Quantifying the link between magma ascent dynamics and tilt

Luke Marsden

Submitted in accordance with the requirements for the degree of
Doctor of Philosophy

The University of Leeds
School of Earth and Environment

May, 2020

The candidate confirms that the work submitted is their own, except where work which has formed part of jointly authored publications has been included. The contribution of the candidate and the other authors to this work has been explicitly indicated below. The candidate confirms that appropriate credit has been given within the thesis where reference has been made to the work of others.

This thesis is submitted as an alternative style of doctoral thesis that includes published material. This is an appropriate format as the work of this thesis can be divided into three distinct strands, each tackling the subject of magma ascent and its link to deformation. These are preceded by an introductory chapter that places the publications within the context of relevant literature. In the final chapter, we discuss these publications together, and the collective broader implications that this work has for the monitoring of silicic volcanoes.

The work in Chapter 2 has been published in the following publication:

Citation: **Marsden, L. H.**, Neuberg, J., Thomas, M., Mothes, P., and Ruiz, M. (2019). *Combining magma flow and deformation modelling to explain observed changes in tilt.* Frontiers in Earth Science 7, 219

I developed the models and wrote the manuscript. JN and MT provided expertise on the governing processes. PM and MR advised on technical aspects of the project. The manuscript also benefitted from constructive reviews from Shigekazu Kusumoto, Oleg Melnik, and Larry Mastin, and the editorial comments of James White and Valerio Acocella. Amy Collinson provided useful contributions to discussions and helped with the modelling software.

The work in Chapter 3 has been published in the following publication:

Citation: **Marsden, L. H.**, Neuberg, J., Thomas, M. (2019). *Topography and tilt at volcanoes.* Frontiers in Earth Science 7, 317

I developed all the models and wrote the manuscript. JN and MT provided technical expertise. The manuscript also benefitted from constructive reviews from Eisuke Fujita and Silvio De Angelis, and the editorial comments of Yosuke Aoki and Valerio Acocella.

Acknowledgements

A huge thank you to my supervisors and friends Jürgen 'Locko' Neuberg and Mark Thomas for always being approachable and interested in my work. We have shared countless long (overrunning) but enjoyable meetings. Also, thanks for all the impromptu meetings where I dropped by your offices when I had hit a wall. I without fail left with a much clearer idea in mind of how to proceed. Thanks for being so supportive when I started a family of my own. The flexibility that I have had in the first few years of Emilia's life has been priceless.

I am especially grateful to Locko, Caro and Chloe for welcoming me and my family into your home on so many occasions, always providing exceptional food, wine and company. I leave a *little* less of an ignoramus when it comes to wine as a result. Your generosity has always gone far above and beyond what is expected of you as a supervisor.

I would like to thank the staff at the IGEPN in Quito, Ecuador, whom I was lucky enough to visit for 2 weeks in March 2018. In particular, thanks to Patricia Mothes, Mario Ruiz, Stephen Hernandez and Santiago Aguaiza, who made me feel welcome in the department, and to Santiago Santamaría and Jorge Yerovi for an unforgettable trip to Tungurahua volcano.

I would also like to thank Dr. David Ferguson and Dr. Jessica Johnson, whose comments throughout the examination process helped me to improve this work.

To my wonderful wife Marte, thanks for encouraging me to be brave enough to follow my dreams. We sacrificed a lot in leaving our old lives behind when I started this project, but have gained much more. Thank you for your endless support and reassurance. Thanks for making life an adventure, where anything is possible. I can't wait to see what the next chapter holds. My little one, Emilia, you are far too young to understand what I've been doing for the first few years of your life, but I hope one day you'll be proud of me. To my Mum, Dad, and sister Hope, you have always believed that I can achieve more than I ever believed myself. There's no doubt that I would never have got to where I am now without you.

Finally, a big thank you to NERC, for providing the funding that made this project possible.

Abstract

Magma viscosity and its ascent rate are key factors in controlling eruption style. Shear stress exerted on the conduit walls as magma ascends pulls up the surrounding edifice, whilst overpressure pushes the edifice outwards. Magma fractures if shear stress exceeds its shear strength, triggering low-frequency seismicity. Shear stress is proportional to both the viscosity of magma and its ascent velocity. Hence, it provides an important link between ascent dynamics and both deformation and seismicity that can be recorded at the surface. Tiltmeters measure changes in inclination, and both shear stress and pressure have been linked conceptually to changes in tilt recorded close to the conduit. However, how much shear stress and pressure are produced as magma ascends, and the relative contribution of each to the tilt, has not previously been quantified.

Firstly, flow and deformation modelling are combined using COMSOL Multiphysics to quantitatively link magma ascent and tilt. Despite shear stress being several orders of magnitude smaller than overpressure at most depths, shear stress generally dominates the tilt signal. Next, I systematically investigate how topography influences tilt, showing how topography controls both the amplitude and polarity of the tilt, and thus the relative contribution of shear stress and pressure. 3D deformation modelling is performed including real volcanic topography to show how a tiltmeter can be strategically deployed at the location most sensitive to changes in source stress. Finally, time-dependent flow modelling is used to show how magma ascent dynamics, and thus shear stress and overpressure, evolve through time due to transient volcanic processes. The growth of a lava dome exerts an increasing loading pressure at the conduit vent that impedes magma ascent, and can cause it to stall even if conditions at depth remain unchanged. By unloading, a full or partial dome collapse can therefore cause an eruption to recommence.

By quantitatively linking magma ascent and deformation, and examining how ascent evolves through time, this work shows the importance of combining flow and deformation modelling in retrospectively investigating what drives temporal variations in seismicity and deformation. This is an important step towards being able to develop a combined forecasting tool using both seismicity and deformation that can be used to detect critical changes in ascent dynamics.

Contents

List of Figures

List of Tables

Nomenclature

List of acronyms

DEM	Digital elevation model
FEM	Finite element model
GPS	Global Positioning System
IGEPN	Instituto Geofísico de la Escuela Politécnica Nacional
InSAR	Interferometric Synthetic Aperture Radar
LP	Long period seismic event
OVT	Observatorio del Volcán Tungurahua
SHV	Soufriére Hills volcano
TBL	Thermal boundary layer
VT	Volcano-tectonic seismic event

List of symbols

α	Radius of spherical pressure source
$\Delta\theta$	Tilt
$\Delta\theta_{\mathrm{AMP}}$	Factor by which tilt is amplified by topography
$\Delta\theta_{\mathrm{DIFF}}$	Difference in tilt due to topography
$\Delta\theta_{\mathrm{raw}}$	Raw tilt angle recorded prior to temperature correction
$\Delta\theta_{\mathrm{r}}$	Reference tilt in the absence of local topography
$\dot{\varepsilon}$	Strain rate
η_0	Melt viscosity
η_{b}	Bulk viscosity

$\eta_{r\infty}$	Infinite shear-rate viscosity bubbly magma
η_{r0}	Zero shear-rate viscosity bubbly magma
η_{rc}	Relative viscosity crystal-bearing magma
η_{rgc}	Relative viscosity three-phase suspension
η_{rg}	Relative viscosity bubbly magma
η_{r}	Relative viscosity
η_{s}	Apparent viscosity
Γ	Bubble surface tension
γ	Parameter that corresponds to crystal growth rate
ν	Poisson's ratio
ϕ_{cpx}	Clinopyroxene crystals volume fraction
ϕ_{c}	Crystal volume fraction
ϕ_{c}^{eq}	Equilibrium crystal content
ϕ_{c}^{max}	Max. packing fraction
ϕ_{c}^{sph}	Max. packing fraction spherical particles
ϕ_{g}	Gas volume fraction
ϕ_{m}	Initial melt fraction
ϕ_{opx}	Orthopyroxene crystals volume fraction
ϕ_{ph}	Content of phenocrysts
ϕ_{plag}	Plagioclase crystals volume fraction
ρ_{b}	Bulk density of magma
ρ_{cpx}	Density of clinopyroxene crystals
ρ_{c}	Average crystal density
ρ_{d}	Dome density
ρ_{e}	Density of edifice
ρ_{opx}	Density of orthopyroxene crystals

ρ_{plag}	Density of plagioclase crystals	
σ_{s}	Shear stress	
τ_{m}	Shear strength of magma	
θ	Slope angle	
θ_{d}	Slope angle of dome	
θ_{maxexp}	Slope angle with maximum exposure to the pressure source	
b	Fitting parameter in equation 2.5	[1.08]
C_{g}	Ideal gas constant	[8.314 $\text{J.K}^{-1}\text{.mol}^{-1}$]
c_{p}	Specific heat capacity	
C_{wi}	Initial H_20 content	
C_{w}	Weight percent of dissolved H_2O	
Ca	Capillary number	
d	Vertical distance from centre of spherical source	
D_{TBL}	Thickness of the thermal boundary layer	
E	Young's modulus	
E_1	Seismic energy in lower frequency window	
E_2	Seismic energy in higher frequency window	
E_{B}	Background seismic energy	
E_{m}	Deformation modulus of a rock mass	
F_{D}	Forces that drive magma ascent	
F_{F}	Frictional force that impedes magma ascent	
F_{L}	Vertical force impeding magma ascent, resulting from dome loading	
G	Shear modulus	
g	Acceleration due to gravity	[9.81 m/s^2]
h_{d}	Dome height	
I	Identity tensor	

K	Constant in equations 2.14 and 4.2	[6/5]
K_s	Temperature coefficient scale factor	
K_z	Temperature coefficient of zero shift	
L	Conduit length	
M	Molar mass of H_2O	[0.018 kg]
m	Constant in equations 2.14 and 4.2	[2]
n	Number of moles of exsolved H_20	
n_b	Bubble number density	
P	Pressure	
P'	Vertical pressure gradient	
P_a	Atmospheric pressure	
P_e	Excess pressure at conduit base	
P_L	Loading pressure at conduit vent	
r	Horizontal distance from centre of source	
R_b	Bubble radius	
R_c	Conduit radius	
r_p	Crystal aspect ratio	
T	Temperature	
t	Time	
T_{DIFF}	Temperature difference within the thermal boundary layer	
T_{cal}	Temperature at which the tiltmeter was calibrated at	
u	Horizontal displacement in x direction	
v	Horizontal displacement in y direction	
V_g	Volume of exsolved H_20	
v_{max}	Ascent velocity at centre of conduit	
v_z	Ascent velocity	

w	Vertical displacement in z direction
z	Depth in conduit
$z_{\max}$	Maximum relief of edifice

Chapter 1

Introduction

Volcanic eruptions are the result of buoyant magma ascending from deep storage reservoirs to the surface, and understanding the processes that govern this ascent is key in forecasting eruption style and scale. In the upper few kilometres, magma is thought to ascend through conduits that link magma reservoirs to the surface (e.g. *Eichelberger et al.*, 1986). Overpressure exerted on the conduit walls pushes the surrounding edifice outwards (*Voight et al.*, 1999), whilst shear stress pulls the edifice upwards (*Beauducel et al.*, 2000). Both shear stress (*Green et al.*, 2006, *Neuberg et al.*, 2018) and pressure (*Voight et al.*, 1999, *Widiwijayanti et al.*, 2005) have been suggested as plausible sources of deformation close to the conduit. Shear stress is proportional to the ascent velocity, and therefore offers an important link between observable deformation and ascent dynamics (*Neuberg et al.*, 2006). However, it remains unclear how much shear stress and pressure are produced as magma ascends, and how they contribute to the deformation recorded. Numerical flow modelling can be used to discern what key factors control magma ascent (*Melnik and Sparks*, 1999, *Collier and Neuberg*, 2006), and quantify how both shear stress and pressure vary both spatially and through time in the conduit. In this thesis, flow and deformation modelling are combined, to quantitatively link magma ascent to observed deformation for the first time, and investigate what influences the amplitude of this deformation. This will contribute to the ultimate aim to invert deformation data for magma ascent rate, one of the most critical parameters in volcanology.

1.1 Magma ascent at silicic volcanoes

Volcanic activity at silicic volcanoes can be subdivided into effusive or explosive behaviour. Explosive eruptions are capable of producing large eruption columns that extend tens of kilometres above the vent, as well as pyroclastic flows and wide-spread ash fall. Effusive eruptions are comparatively slow, producing short lava flows or forming lava domes. A single volcano can exhibit both effusive and explosive behaviour,

and can transition between the two within the same period of activity. The collapse of a lava dome for example brings about an instantaneous reduction in the pressure as the overlying load decreases, which can lead to explosive behaviour. Numerical modelling of magma ascent has played an important role in discerning what key factors control this variability in eruption style (e.g. *Papale*, 1999, *Melnik and Sparks*, 1999, *Thomas and Neuberg*, 2014).

Magma typically comprises melt, crystals, and volatiles, the relative proportions of which significantly influence the rheology (*Truby et al.*, 2015). As magma ascends and pressure decreases, volatiles exsolve from the melt to form bubbles. Volatile exsolution reduces the liquidus temperature of the melt, leading to the solidification of small, elongate crystals called *microlites* (*Couch et al.*, 2003). Therefore, the proportions of both crystals and bubbles (hereon termed the *crystal* and *gas volume fraction*, respectively) increase as magma approaches the surface. Magma with a higher gas volume fraction is more buoyant, and ascends more quickly. Both dehydration of the melt (*Giordano et al.*, 2008) and crystallisation (*Maron and Pierce*, 1956) cause the bulk viscosity of magma to increase, producing steep vertical viscosity gradients in the upper conduit. If the viscosity continues to increase, the magma may solidify in the upper conduit, forming a *plug*, impeding or even stalling ascent (*Hammer et al.*, 1999).

The eruption style depends on the magma viscosity and the gas volume fraction close to the surface (*Gonnermann*, 2015). At low to moderate gas volume fractions, the bubbles are suspended in the melt phase, and magma behaves as a viscous fluid, hence erupts effusively. However, at higher gas volume fractions, bubbles coalesce until the magma is gas dominated, tearing the melt into fragments. The rapid expansion of this gas-fragment mixture culminates in an explosive eruption. This usually occurs in the uppermost section of the conduit, where the bubbles expand most rapidly.

The gas volume fraction depends on the content of volatiles initially dissolved in the melt, and how much gas can escape from the conduit. In low-viscosity, basaltic systems, bubbles can ascend through the melt relatively quickly. However, highly viscous silicic melt takes more time to displace, and restricts bubbles from ascending over eruption time-scales (*Eichelberger et al.*, 1986). Gas instead escapes through fractures (*Gonnermann and Manga*, 2003, *Gaunt et al.*, 2014), or through pathways of interconnected bubbles above a critical gas volume fraction (*Klug and Cashman*, 1996, *Okumura et al.*, 2008).

The relative velocity at which the melt and gas phases of the magma are able to ascend is key in controlling how much gas can escape from the conduit, and therefore controls the eruption style (Figure 1.1). Slower magma ascent allows more time for crystallisation and gas to escape. It reaches the surface with a low to moderate gas volume fraction is therefore more likely to erupt effusively or solidify. Conversely, gas has less time to escape from magma that is ascending relatively quickly, hence magma is more likely to fragment before it reaches the surface, favouring explosive activity.

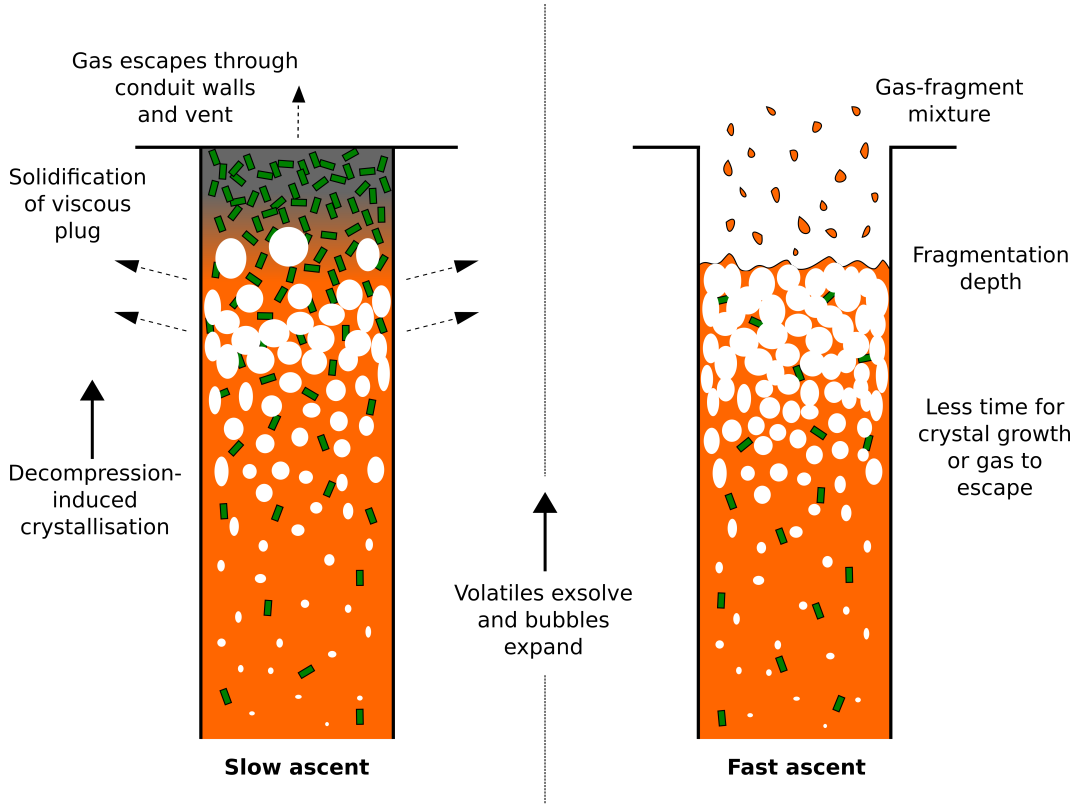

Figure 1.1: Conceptual diagram illustrating how magma ascent rate influences eruption style. Crystallisation and gas escape are more prominent if magma is ascending slowly, favouring effusive eruptions and possibly plug formation. Fragmentation and explosive activity is more likely if magma ascends more rapidly as there is less time for gas to escape.

Ascent rate is primarily governed by the viscosity and buoyancy of the magma, which are in turn controlled by such factors as the composition (*Giordano et al.*, 2008, *Spera*, 2000), volatile content (*Mader et al.*, 2013), driving pressure gradient (*Thomas and Neuberg*, 2014), temperature (*Giordano et al.*, 2008) and crystal content (*Maron and Pierce*, 1956, *Melnik and Sparks*, 1999) of the magma. Shear stress, and the deformation it produces, is proportional to the ascent rate (*Neuberg et al.*, 2006), hence offers an opportunity to monitor changes in ascent velocity. This would allow volcanologists to more reliably forecast eruption style and scale. For this to be possible, a more complete, quantitative understanding is required of how magma ascent induces deformation at the surface.

1.2 Deformation

Deformation at the surface of a volcanic edifice and surrounding region can provide information on stress changes at depth. Deformation can be induced by a range of sources, which display different characteristic spatial and temporal deformation patterns at the surface. Broad metre-scale uplift and subsidence over periods of days to

years can be indicative of inflation and deflation of a magma reservoir at depth (*Mogi*, 1958). More localised deformation from shallower sources may potentially be superimposed upon this broader trend. Being able to quantify the relative contribution of different sources to the deformation at any monitored location is crucial in being able to understand how the volcanic system is evolving through time, and ultimately in forecasting changes in activity.

Since deformation occurs over a range of different scales and time-scales, it is prudent to use a range of monitoring techniques. GPS (Global Positioning System) stations provide a continuous recording of the X,Y and Z coordinates through time. Tiltmeters measure the change in inclination of the ground in X and Y through time. InSAR (Interferometric Synthetic Aperture Radar) can be used to create maps of the spatial deformation field between two points in time, by collecting radar images from orbiting satellites. A good spatial coverage can be gained using InSAR, but the resolution in time is limited by the return period of the orbiting satellite. GPS and tiltmeters provide a continuous recording through time, and of higher precision than InSAR, but are limited spatially to a single location. At a number of silicic volcanoes, deformation that correlates with volcanic activity has been exclusively detected by tiltmeters deployed close to the conduit, due to their particularly high precision relative to other instruments. This includes Soufrière Hills volcano, Montserrat (SHV) (*Voight et al.*, 1998), Tungurahua volcano, Ecuador (*Mothes et al.*, 2015), Mount St. Helens, USA (*Anderson et al.*, 2010), Volcán de Colima, Mexico (*Zobin et al.*, 2007), and Galeras volcano, Colombia (*Medina et al.*, 2017). I use SHV and Tungurahua volcano as case examples throughout this thesis.

1.3 Tilt

A tiltmeter records change in the inclination of the ground through time. A typical instrument can measure changes to a precision of around 1 µrad, equivalent to a differential uplift of 1 mm over a horizontal distance of 1 km. An electronic tiltmeter contains a electrolytic tilt sensor, consisting of a casing partially filled with conductive fluid (electrolyte), and a central pick-up electrode with an excitation electrode to either side (Figure 1.2). The electrical resistance between the electrodes is proportional to the area of each electrode submerged in the conductive fluid. As the instrument is tilted, the electrical resistance between the central pick-up electrode and each excitation electrode to either side of it varies. This resistance is proportional to the tilt angle.

The conductive fluid is subject to thermal expansion and contraction as the temperature varies. As the volume of the fluid changes, the proportion of the electrodes submerged in the conductive fluid also changes. Therefore, the resistance and tilt are sensitive to the temperature. Fortunately, a simple correction can be applied to recover

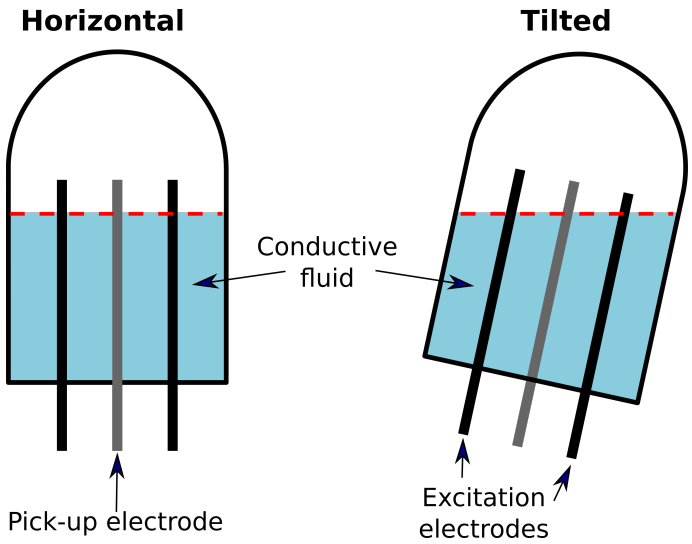

Figure 1.2: Schematic diagram of a electrolytic tilt sensor. As the sensor tilts, the proportion of each electrode submerged in conductive fluid changes. The tilt is proportional to the area of each electrode submerged.

the true tilt angle. The compensated tilt angle, $\Delta\theta$, is a function of the raw tilt angle recorded, $\Delta\theta_{\text{raw}}$, and the difference between the temperature at the time of recording, T, and when the instrument was calibrated, T_{cal}

$$\Delta\theta = \Delta\theta_{\text{raw}} + \Delta\theta_{\text{raw}} K_{\text{s}} \left(T - T_{\text{cal}}\right) - K_{\text{z}} \left(T - T_{\text{cal}}\right). \tag{1.1}$$

K_{s} is the temperature coefficient scale factor and K_{z} is the temperature coefficient of zero shift, each measured in a laboratory and provided on the instrument manual. For the RETU tiltmeter at Tungurahua, $T_{\text{cal}} = 21\,^{\circ}\text{C}$, $K_{\text{s}} = 0.05$ and $K_{\text{z}} = 3$. Upon applying the temperature correction to the tilt data, the amplitude of the tilt variations at RETU between June 2013 and May 2014 reduces from around 500 µrad to around 170 µrad (Figure 1.3). The trend through time is relatively unaltered by this correction, and so the raw data can be interpreted for monitoring purposes. However, for deformation modelling, in order to quantify the amplitude of the pressure or shear stress source, it is imperative that the amplitude of the tilt changes are accurate.

Attempts have been made to link changes in tilt detected close to the conduit to changes in pressure in the upper edifice. The upper conduit is overpressured with respect to the surrounding edifice, due to dehydration of volatiles from the melt, resulting in large vertical viscosity gradients. This produces steep vertical pressure gradients over the same region (*Sparks*, 1997, *Dingwell*, 1996). Additionally, the solidification of small microlite crystals in the upper conduit can cause gas pressure to increase by up to a few tens of MPa (*Sparks*, 1997). The total overpressure in the system depends on the relative rates of this pressure build-up, and the decrease in pressure due to gas escape and fracturing of the host rock. In a number of studies (*Widiwijayanti et al.*, 2005,

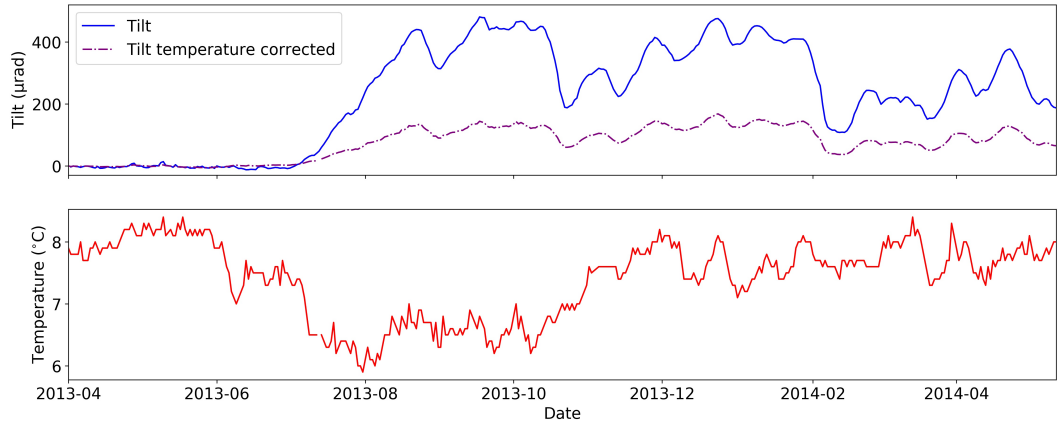

Figure 1.3: Top: Raw and temperature corrected tilt at the RETU tiltmeter, Tungurahua. Bottom: Maximum daily temperature recorded at the tiltmeter through time.

Medina et al., 2017), near-field deformation has been linked analytically to changes in pressure of a point source in an elastic half-space. Here, the radial tilt, $\Delta\theta$, can be given as

$$\Delta\theta = \frac{9\alpha^3 \Delta P}{4G} \frac{rz}{(r^2 + z^2)^{5/2}} \tag{1.2}$$

where ΔP is the change in pressure, α is the source radius, r and z are the horizontal and vertical distance from the centre of the source respectively, and G is the shear modulus (*Mogi*, 1958). The shear modulus is a function of the Poisson's ratio, ν, and the Young's modulus, E, such that $G = E/2(1+\nu)$. A trade-off exists between the change in pressure and the source radius. *Widiwijayanti et al.* (2005) showed that for a decompression of 5 MPa to explain a decrease in tilt of 20-22 µrad at SHV, a source radius of 200-340 m is required. This far exceeds the estimated conduit radius of 15 m (*Voight et al.*, 1999). However, using this radius would likely require the source pressure to far exceed the tensile strength of the host rock at low confining pressures, thought to be around 4 MPa for intact andesite at SHV (*Voight et al.*, 1999). *Widiwijayanti et al.* (2005) suggested that the source radius could exceed that of the conduit if the surrounding region is heavily fractured and fluid-saturated, thus extending the pressurised region. However, increasing the source radius would most likely reduce the pressure of that source (*Collinson and Neuberg*, 2012). It is similarly difficult to link tilt to the pressurisation of a vertical line source, representative of a cylindrical conduit, using realistic values for the overpressure (*Voight et al.*, 1999). It has been suggested that the conduit at SHV is fed by a dyke at a depth of around 1.2 km below the surface (*Costa et al.*, 2007a,b). *Hautmann et al.* (2009) suggested that the pressurisation of the transition zone between this dyke and the conduit can produce the tilt variations observed.

Shear stress has been suggested in several studies as an alternative source of near-

field deformation (*Beauducel et al.*, 2000, *Green et al.*, 2006, *Neuberg et al.*, 2018). As highly viscous magma ascends through the volcanic conduit, shear stress exerted at the conduit walls pulls up the surrounding edifice, causing deformation at the surface. Shear stress, σ_s, is a function of the ascent velocity, v_z, and viscosity, η, of the magma, such that

$$\sigma_s = \frac{d\varepsilon}{dt}\eta = \frac{dv_z}{dr}\eta, \tag{1.3}$$

where $d\varepsilon/dt$ is strain rate, which can be written as dv_z/dr, the lateral gradient of the magma ascent velocity across the conduit (*Neuberg et al.*, 2006). This thereby provides an important link between ascent dynamics and deformation. How close to the conduit a tiltmeter needs to be for one to detect changes ascent dynamics depends on such factors as the amplitude of shear stress and overpressure in the conduit (*Green et al.*, 2006), the mechanical properties of the edifice (*Heap et al.*, 2020), topography (*Johnson et al.*, 2019), and the relative contribution of other deformation sources (e.g. pressurisation of a shallow reservoir (*McTigue and Segall*, 1988).

1.3.1 Tilt and low-frequency seismicity

If shear stress exceeds the shear strength of the magma, magma fractures (*Goto*, 1999, *Tuffen et al.*, 2003), triggering low-frequency seismicity (*Neuberg et al.*, 2006). The total shear stress is therefore partitioned between inducing deformation and generating low-frequency seismicity (*Neuberg et al.*, 2018).

Neuberg et al. (2006) observed a negative correlation between tilt cycles observed at SHV and the occurrence of low-frequency earthquake swarms (Figure 1.4). Seismicity commences at an inflection point in the tilt cycle, when the maximum increase in tilt over time is observed. This point marks a crucial change in trend where the rate of increase in tilt begins to decrease. Seismicity then ceases when the tilt cycle goes through a second inflection point, where the maximum decrease in tilt over time is observed. This correlation between the two implies a common driving mechanism, which suggests to incorporate both measurements into a combined monitoring tool.

It is possible to quantify changes in the total seismic energy through time by integrating the modulus of the seismogram (i.e. the power of the signal) through time. If seismicity and tilt and driven by both changes in shear stress, one may expect more easily detectable changes in tilt to correlate with larger increases in the seismic energy, from either a single large earthquake or a swarm of smaller events. Here, I use data from the RETU station at Tungurahua volcano, where a correlation has previously been observed between tilt and the number of low-frequency earthquakes (*Neuberg et al.*, 2018). The total seismic energy consists of the signal of interest and noise from numerous sources. Computing energy in the frequency domain has the distinct advantage that energy over a discreet frequency range can be isolated and measured. Low-frequency energy can

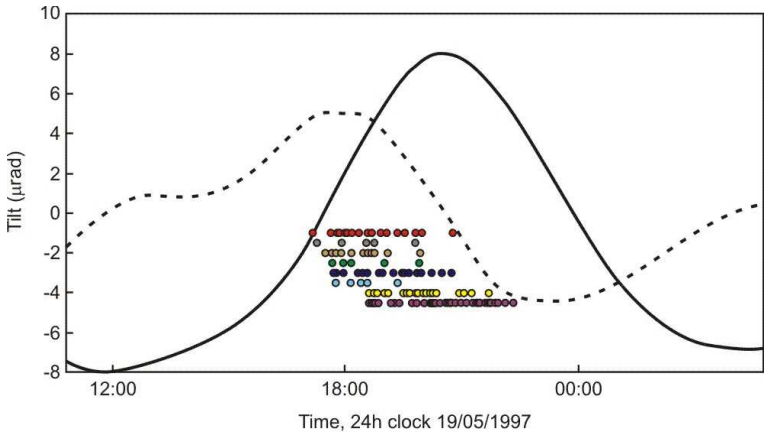

Figure 1.4: Low-frequency earthquakes at SHV on May 19th 1997. Individual earthquakes are represented by dots, each colour represents a different family of similar waveforms. Lines are plotted for tilt (solid) and its time derivative (dashed). From *Neuberg et al.* (2006).

be discriminated from higher frequency noise. I have first divided the seismogram into 10 s windows. The energy within a each window, E_1, is calculated by computing the frequency spectrum of the data and then integrating between two desired frequencies - in this case 1-4 Hz. The change in energy through time can be assessed by comparing successive time windows.

In order to quantify only energy from low-frequency earthquakes, energy from other sources must be subtracted from the total energy computed. The *background* energy level is the energy measured in the absence of activity. In reality, the background level fluctuates through time, however this is difficult to account for. Therefore, the background energy level has been assumed constant throughout the period of interest, and subtracted from the total energy for each time window. The energy in a window has been muted where the energy is lower than computed background level. Low-frequency earthquakes can be discriminated from volcano-tectonic (VT) events in the frequency domain by computing the energy in a second higher frequency window, E_2, (6-9 Hz) and computing the ratio of the energy in the two windows. Low-frequency earthquakes have a predominantly low-frequency content, and therefore the ratio E_1/E_2 is high. VT earthquakes have a greater proportion of higher frequency energy, and therefore the ratio of low/high frequency energy is smaller.

Testing was performed on a suite of hand-picked events to determine the optimal ratio and background energy threshold to be used, to ensure that low-frequency earthquakes are discriminated from VTs and background energy. A subset of these events is shown in Figure 1.5. One challenge of this is that the dominant frequency of a VT reduces through time as amplitude decreases, because higher frequency energy is preferentially attenuated (*Toksöz et al.*, 1979). Therefore, the tails of VT events have a higher ratio of low/high frequency energy. To tackle this, the background energy threshold must be increased to ensure that the tails of VT events are discarded, at

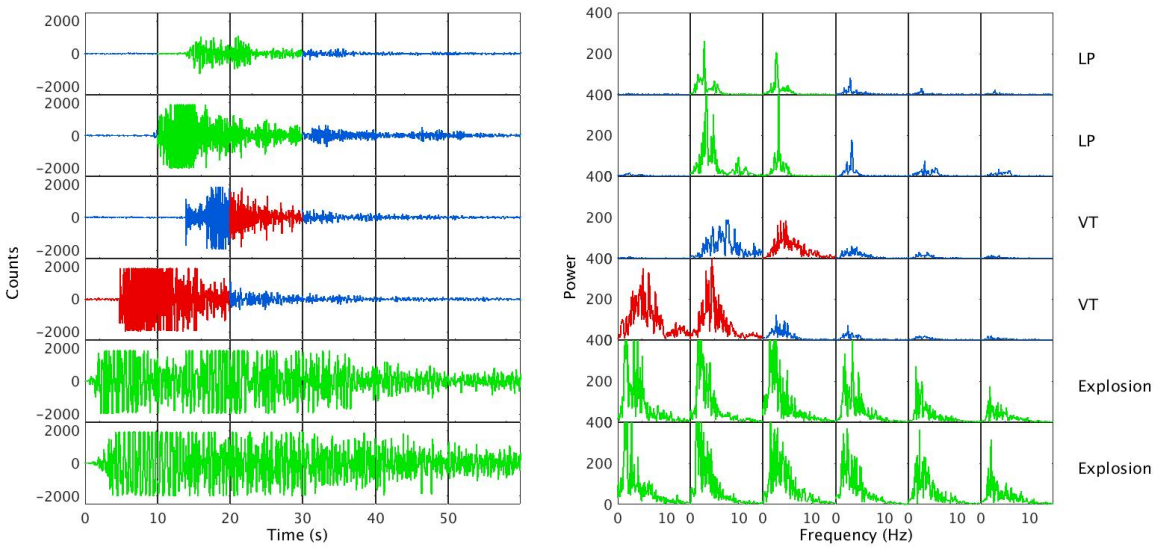

Figure 1.5: Example of how low-frequency seismic energy has been isolated and quantified on a subset of events from Tungurahua volcano. Each event is 60 seconds long, and has been divided into 10 s windows. Each window has been colour coded. Blue: $E_1 < 13$. Red: $E_1 > 13$, $E_1/E_2 < 2.5$. Green: $E_1 > 13$, $E_1/E_2 > 2.5$. Energy in blue and red windows has been muted. For green windows, the background energy level, $E_B = 13$, has been subtracted from the value of E_1. Left: Event in time domain. Right: The frequency spectrum computed for each corresponding 10 s time window.

the compromise of excluding some low magnitude low-frequency earthquakes. Here, we set the background energy threshold, E_B, at 13, and the low/high frequency ratio threshold, E_1/E_2, at 2.5. As calculations were performed on the raw data as counts, these values are unitless.

Following the aforementioned processing steps, the isolated low-frequency seismic energy is still dominated by volcanic explosions (Figure 1.6), that have a similar spectral content to low-frequency earthquakes but are more energetic (Figure 1.5). Here, I remove the energy from volcanic explosions by manually muting the seismogram for the duration of each explosion. Unfortunately, it is not possible to identify low-frequency earthquakes that coincide with the timing of explosions using this method. Also, unwanted energy may be included, where for example a VT has an anomalously low-frequency content. However, since the majority of the isolated energy is generated by low-frequency earthquakes, it is possible to identify the timing of low-frequency earthquake swarms using this method and examine how they correlate with the tilt. Contrary to at SHV, at Tungurahua, in the lead up to the Vulcanian explosion on February 1st 2014, tilt began to decrease *before* the onset of seismicity (Figure 1.6). This is not obviously consistent with the shear stress partitioning model of (*Neuberg et al.*, 2018), where one would expect seismicity to initiate before or coincident with a decrease in tilt. Therefore, further work is required to investigate what controls the

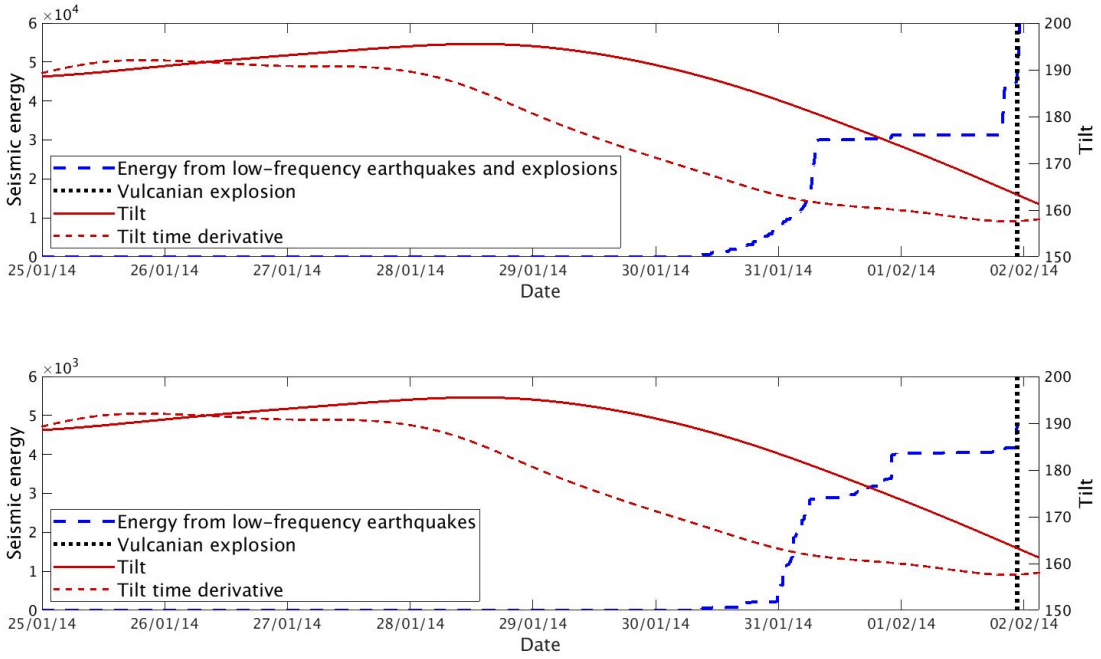

Figure 1.6: Isolated cumulative seismic energy, tilt, and its time derivative recorded at RETU, Tungurahua, leading up to a Vulcanian explosion on 1st February 2014. Top: Seismic energy from explosions and low-frequency earthquakes. Bottom: Seismic energy from low-frequency earthquakes only.

correlation between seismicity in tilt in this case.

1.4 Deformation modelling and shear stress

Previous deformation modelling linking shear stress to tilt has successfully established shear stress as a feasible source of near-deformation at silicic volcanoes, which must be considered alongside pressure. However, in most studies, deformation is linked to a single value for the shear stress, over a certain depth range (*Green et al.*, 2006, *Nishimura*, 2009, *Neuberg et al.*, 2018). The amount of stress produced as magma ascends has often been estimated assuming Poiseuille flow, where the ascent velocity, v_z, can be given as

$$v_z(r) = \frac{1}{4\eta}\frac{dP}{dz}(R^2 - r^2), \tag{1.4}$$

where η is magma viscosity, dP/dz is the vertical pressure gradient, R is the conduit radius, and r is the horizontal distance from the centre of the conduit. The strain rate,

dv_z/dr, is the spatial derivative of the velocity.

$$\frac{dv_z}{dr} = \frac{-r}{2\eta}\frac{dP}{dz} \tag{1.5}$$

The strain rate is greatest at the conduit wall, where r = R.

$$\frac{dv_z}{dr} = \frac{-R}{2\eta}\frac{dP}{dz} \tag{1.6}$$

By combining Eqs. 1.3 and 1.6, one can calculate the shear stress exerted on the conduit wall, as

$$\sigma_s = \frac{-R}{2}\frac{dP}{dz}. \tag{1.7}$$

The maximum velocity, v_{max}, is reached at the centre of the conduit, where $r = 0$, such that

$$v_{max} = \frac{1}{4\eta}\frac{dP}{dz}R^2 \tag{1.8}$$

Equation 1.8 can be rearranged to solve for the pressure gradient, which can then be substituted into Eq. 1.7.

$$\frac{dP}{dz} = \frac{4v_{max}\eta}{R^2} \tag{1.9}$$

$$\sigma_s = 2\eta\frac{v_{max}}{R} \tag{1.10}$$

In an attempt to assign a suitable value for the shear stress to be applied in their deformation modelling, *Neuberg et al.* (2018) used Eq. 1.10 and reasonable values of $\eta = 1 \times 10^{11}$ Pas (for highly crystalline degassed magma), $v_{max} = 0.0015$ m/s, and $R = 15$ m, to obtain $\sigma_s = 20$ MPa. Such values are of the same order of magnitude as estimates of the shear strength of silicate melt (10 MPa, *Tuffen and Dingwell*, 2005). By applying a shear stress of 20 MPa along a conduit with a length of 4.5 km, *Neuberg et al.* (2018) were able to explain 480 µrad of tilt at the RETU tiltmeter at Tungurahua using a Young's modulus of $E = 1$ GPa. However, it is unclear whether a shear stress of 20 MPa can be produced and sustained over a large depth range as magma ascends.

Eqs. 1.4-1.10 are only applicable where the viscosity in the conduit is constant. The shear stress exerted on the conduit wall as magma ascends is a function of both the ascent velocity and the viscosity of the magma (Eq. 1.3). Magma viscosity increases by several orders of magnitude as magma ascends, due to the exsolution of volatiles and crystallisation (*Dingwell*, 1996, *Melnik and Sparks*, 1999). Using a shear stress of 20 MPa in Eq. 1.7 yields a vertical pressure gradient of 2.67 MPa/m or a pressurisation of 26 MPa over a short distance of only 10 m. This is almost 2 orders of magnitude greater than the value of 3.5×10^4 Pa/m that the flow models of *Sparks* (1997) deem

achievable in the upper 1000 m of andesitic conduits. Therefore, a shear stress of $\sigma_s = 20$ MPa does not appear to be realistic, particularly over a relatively large depth range of 4.5 km.

1.5 Flow modelling

Numerical modelling can be used to simulate the ascent of magma through a conduit, and quantify how both shear stress and pressure vary spatially and through time. They are able to incorporate parameters and equations from a wide range of disciplines within volcanology. *Wilson et al.* (1980) published the first 1D volcanic conduit flow model, making several simplifying assumptions, for example neglecting variations in viscosity with depth. Over the following decades, significant advances have been made in flow modelling, including consideration of decompression-induced crystallisation (*Melnik and Sparks*, 1999, 2005), gas loss (*Jaupart and Allègre*, 1991, *Diller et al.*, 2006), the exsolution of volatiles (*Burgisser and Gardner*, 2004), changes in conduit geometry (*Aravena et al.*, 2017), fragmentation (*Papale*, 1999), non-Newtonian rheology (*Caricchi et al.*, 2007) and the transition from viscous flow to friction-controlled flow (*Okumura and Kozono*, 2017).

All of the models referenced above are 1D and therefore assume that flow properties can be averaged at each depth. However, a number of studies have highlighted the importance of lateral variations in governing ascent (*Llewellin and Manga*, 2005, *Collier and Neuberg*, 2006, *Tsvetkova and Melnik*, 2018). Three-phase magma, comprising melt, bubbles and crystals, has a shear-thinning rheology (*Llewellin et al.*, 2002, *Costa et al.*, 2009), meaning that the viscosity decreases as the strain rate increases. Therefore, the viscosity is reduced towards the conduit walls. Consequently, the ascent velocity is higher towards the conduit walls, and the velocity profile deviates from the parabolic one assumed in 1D models (*Llewellin and Manga*, 2005, *Collier and Neuberg*, 2006). 2D modelling of magma ascent has allowed further investigation into how ascent dynamics are influenced by shear thinning (*Llewellin and Manga*, 2005), thermal boundary layers (*Collier and Neuberg*, 2006), changes in conduit geometry with depth (*Thomas and Neuberg*, 2012), gas loss (*Chevalier et al.*, 2017, *Collombet*, 2009) and crystallisation (*Tsvetkova and Melnik*, 2018).

Despite these advances, volcanologists are still unable to realistically model ascent, due to our incomplete knowledge of conduit geometry, crystallisation, the rheology of three-phase magmas, outgassing from a conduit, the transition from liquid magma to solidified rock, and other factors. Considering these limitations, one should not expect conduit flow models to perfectly reproduce the conditions observed in a given eruption. Instead, the strength of these models is in deciphering what key parameters control ascent dynamics, and quantifying how sensitive magma ascent is to changes in these parameters.

Throughout this thesis, I build upon the 2D axisymmetric flow models of *Collier and Neuberg* (2006) and *Thomas and Neuberg* (2014) in the finite element modelling (FEM) software, COMSOL Multiphysics. I obtain depth-dependent profiles of shear stress and pressure at the conduit walls, and use them to drive my deformation models, thereby linking magma ascent to deformation.

1.6 Finite element modelling in COMSOL Multiphysics

Finite element analysis is widely used in mathematics and engineering to model processes described by partial differential equations (PDEs). Analytical solutions to PDEs cannot be directly obtained where geometries, material properties or loads are complex. The finite element method approximates the PDEs in a system of algebraic equations over the domain. The domain is subdivided into a network of *elements* that connect *nodes*, the pattern of which is referred to as the *mesh*. Higher order elements can also have nodes that are not at the corner of the element (Figure 1.7). The PDEs are approximately solved at the coordinate of each node. The accuracy of the solution increases as the number of nodes across the domain is increased, however, so does the computation time. Therefore, a mesh refinement study must be performed to determine the number of nodes required to find a solution that is sufficiently accurate. A spatially variant mesh is often employed to increase the resolution of the mesh over regions of interest, or where there are highly non-linear changes in modelled variables, for example temperature, velocity or displacement. Boundary conditions must be applied at the edges of the model, to provide a full description of the physics and constrain the problem.

COMSOL Multiphysics is a commercial FEM software, that can be used to simulate of a wide range of physical phenomena. COMSOL has been used in a number of sophisticated, diverse studies within volcanology, for example modelling ground deformation (*Bagnardi et al.*, 2013, *Hickey and Gottsmann*, 2014, *Johnson et al.*, 2019), magma ascent (*Massol and Jaupart*, 2009, *Albino et al.*, 2011, *Chevalier et al.*, 2017), outgassing from the conduit (*Collinson and Neuberg*, 2012), stress transfer between multiple magma bodies (*Albino and Sigmundsson*, 2014), the adhesion of ash particles (*Taltavull et al.*, 2016), and permafrost thickness on active volcanoes (*Abramov et al.*, 2008). A key strength of COMSOL is its ability to easily account for multiple physical phenomena simultaneously. This has not been exploited in this project, as the flow and deformation modelling are decoupled to avoid convergence issues. However, previous studies have used the multiphysics option to investigate the effects of heat transfer (*Costa et al.*, 2007c) or gas escape (*Chevalier et al.*, 2017) on magma ascent.

Magma ascent is simulated using the laminar flow interface in COMSOL, in the Computational Fluid Dynamics (CFD) module, building on the 2D axisymmetric flow models of *Collier and Neuberg* (2006) and *Thomas and Neuberg* (2014). A simplified

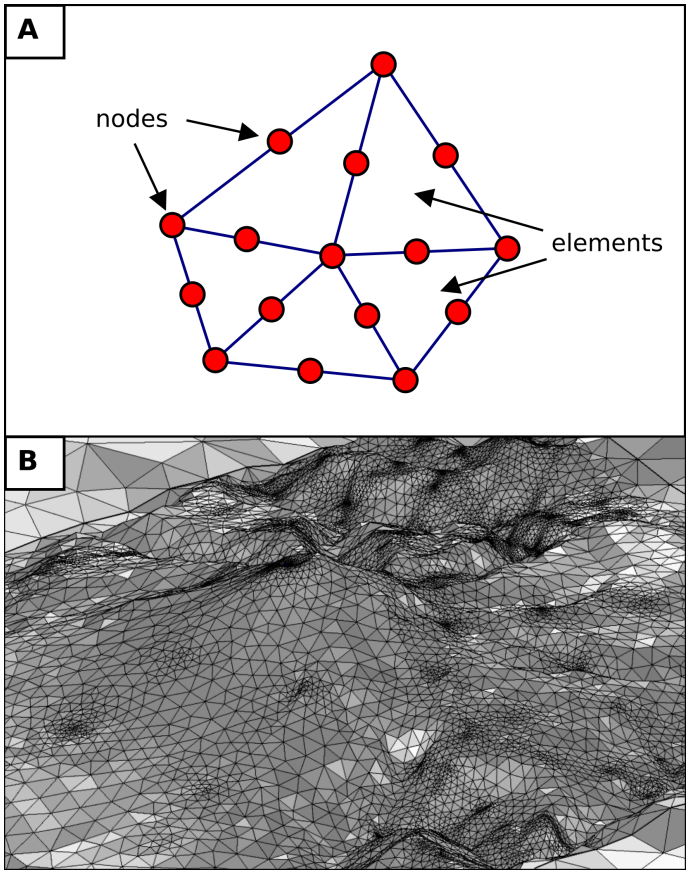

Figure 1.7: Top: Illustration of a mesh in a finite element model. A solution is computed at each node point. Bottom: Example of a spatially variant mesh used to represent the topography at Tungurahua volcano.

cylindrical geometry is used to represent the conduit. I obtain depth-dependent profiles of shear stress and overpressure at the conduit walls, and use them to drive my deformation models, thereby linking magma ascent to deformation. Deformation is simulated using the solid mechanics interface, in the Structural Mechanics module, and builds on the work of *Neuberg et al.* (2018).

1.7 Project aims

The primary focus of this research is to quantitatively link magma ascent to near-field deformation at silicic volcanoes, and understand what controls observed patterns in tilt and low-frequency seismicity that coincide with eruptive activity. More specifically:

1. To quantify the relative contribution of shear stress and pressure to observed changes in tilt, recorded in close proximity to the conduit.
2. To understand what key factors can drive changes in ascent dynamics, as well as tilt through time.
3. To investigate how topography influences tilt.

1.8 Thesis outline

In Chapter 2, magma ascent and deformation modelling are combined to investigate the relative contribution of shear stress and overpressure to observed changes in tilt. I investigate as a case study Tungurahua volcano, Ecuador, where between 2013 and 2014 Vulcanian explosions coincided with cycles of tilt and low-frequency seismicity. I discern what key factors can drive changes in shear stress, pressure, and therefore tilt and seismicity through time.

In Chapter 3, I show how topography can amplify or reduce tilt induced by either the pressurisation of a conduit, dyke or spherical reservoir, or shear stress exerted on the walls of a conduit. Simple 2D axisymmetric models are first used to show how tilt is influenced by changes in slope, before 3D digital elevation models of SHV and Tungurahua are incorporated, to demonstrate how real topography can affect the tilt. I quantify the error that arises if topography is neglected when inverting for changes in source stress. I also discuss how topography can be exploited when deploying a tiltmeter, to maximise it's sensitivity to changes in source stress.

Advancing on the equilibrium models of Chapter 2, in Chapter 4 fully time-dependent magma ascent models are developed. I show how the growth of a lava dome can exert a top-down control on ascent dynamics, due to an increase in pressure at the conduit vent. I explore what factors control the height a lava dome can grow to, and investigate under what conditions dome growth can cause an eruption to cease, at least temporarily.

Finally, in Chapter 5, the main conclusions of the research are summarised. I discuss the broader implications of this work for monitoring of volcanoes. I summarise the limitations of the presented methods, and discuss what further work could be done to build upon the findings of this study.

References

Abramov, A., S. Gruber, and D. Gilichinsky (2008), Mountain permafrost on active volcanoes: field data and statistical mapping, Klyuchevskaya volcano group, Kamchatka, Russia, *Permafrost and Periglacial Processes*, *19*(3), 261–277. 1.6

Albino, F., and F. Sigmundsson (2014), Stress transfer between magma bodies: influence of intrusions prior to 2010 eruptions at Eyjafjallajökull volcano, Iceland, *Journal of Geophysical Research: Solid Earth*, *119*(4), 2964–2975. 1.6

Albino, F., V. Pinel, H. Massol, and M. Collombet (2011), Conditions for detection of ground deformation induced by conduit flow and evolution, *Journal of Geophysical Research: Solid Earth*, *116*(B6). 1.6

Anderson, K., M. Lisowski, and P. Segall (2010), Cyclic ground tilt associated with the 2004–2008 eruption of Mount St. Helens, *Journal of Geophysical Research: Solid Earth*, *115*(B11). 1.2

Aravena, Á., M. d. Vitturi, R. Cioni, and A. Neri (2017), Stability of volcanic conduits during explosive eruptions, *Journal of Volcanology and Geothermal Research*, *339*, 52–62. 1.5

Bagnardi, M., F. Amelung, and M. P. Poland (2013), A new model for the growth of basaltic shields based on deformation of Fernandina volcano, Galápagos Islands, *Earth and Planetary Science Letters*, *377*, 358–366. 1.6

Beauducel, F., F.-H. Cornet, E. Suhanto, T. Duquesnoy, and M. Kasser (2000), Constraints on magma flux from displacements data at Merapi volcano, Java, Indonesia, *Journal of Geophysical Research: Solid Earth*, *105*(B4), 8193–8203. 1, 1.3

Burgisser, A., and J. E. Gardner (2004), Experimental constraints on degassing and permeability in volcanic conduit flow, *Bulletin of volcanology*, *67*(1), 42–56. 1.5

Caricchi, L., L. Burlini, P. Ulmer, T. Gerya, M. Vassalli, and P. Papale (2007), Non-Newtonian rheology of crystal-bearing magmas and implications for magma ascent dynamics, *Earth and Planetary Science Letters*, *264*(3), 402–419. 1.5

Chevalier, L., M. Collombet, and V. Pinel (2017), Temporal evolution of magma flow and degassing conditions during dome growth, insights from 2D numerical modeling, *Journal of Volcanology and Geothermal Research*, *333*, 116–133. 1.5, 1.6

Collier, L., and J. Neuberg (2006), Incorporating seismic observations into 2D conduit flow modeling, *Journal of Volcanology and Geothermal Research*, *152*(3), 331–346. 1, 1.5, 1.6

Collinson, A., and J. Neuberg (2012), Gas storage, transport and pressure changes in an evolving permeable volcanic edifice, *Journal of Volcanology and Geothermal Research*, *243*, 1–13. 1.3, 1.6

Collombet, M. (2009), Two-dimensional gas loss for silicic magma flows: toward more realistic numerical models, *Geophysical Journal International*, *177*(1), 309–318. 1.5

Costa, A., O. Melnik, and R. Sparks (2007a), Controls of conduit geometry and wall-rock elasticity on lava dome eruptions, *Earth and Planetary Science Letters*, *260*(1), 137–151. 1.3

Costa, A., O. Melnik, R. Sparks, and B. Voight (2007b), Control of magma flow in dykes on cyclic lava dome extrusion, *Geophysical Research Letters*, *34*(2). 1.3

Costa, A., O. Melnik, and E. Vedeneeva (2007c), Thermal effects during magma ascent in conduits, *Journal of Geophysical Research: Solid Earth*, *112*(B12). 1.6

Costa, A., L. Caricchi, and N. Bagdassarov (2009), A model for the rheology of particle-bearing suspensions and partially molten rocks, *Geochemistry, Geophysics, Geosystems*, *10*(3). 1.5

Couch, S., R. Sparks, and M. Carroll (2003), The kinetics of degassing-induced crystallization at soufriere hills volcano, montserrat, *Journal of Petrology*, *44*(8), 1477–1502. 1.1

Diller, K., A. Clarke, B. Voight, and A. Neri (2006), Mechanisms of conduit plug formation: Implications for vulcanian explosions, *Geophysical Research Letters*, *33*(20). 1.5

Dingwell, D. B. (1996), Volcanic dilemma: flow or blow?, *Science*, *273*(5278), 1054. 1.3, 1.4

Eichelberger, J., C. Carrigan, H. Westrich, and R. Price (1986), Non-explosive silicic volcanism, *Nature*, *323*(6089), 598–602. 1, 1.1

Gaunt, H. E., P. R. Sammonds, P. G. Meredith, R. Smith, and J. S. Pallister (2014), Pathways for degassing during the lava dome eruption of Mount St. Helens 2004–2008, *Geology*, *42*(11), 947–950. 1.1

Giordano, D., J. K. Russell, and D. B. Dingwell (2008), Viscosity of magmatic liquids: a model, *Earth and Planetary Science Letters*, *271*(1), 123–134. 1.1

Gonnermann, H. M. (2015), Magma fragmentation, *Annual Review of Earth and Planetary Sciences*, *43*, 431–458. 1.1

Gonnermann, H. M., and M. Manga (2003), Explosive volcanism may not be an inevitable consequence of magma fragmentation, *Nature*, *426*(6965), 432–435. 1.1

Goto, A. (1999), A new model for volcanic earthquake at Unzen Volcano: Melt rupture model, *Geophysical Research Letters*, *26*(16), 2541–2544. 1.3.1

Green, D., J. Neuberg, and V. Cayol (2006), Shear stress along the conduit wall as a plausible source of tilt at Soufrière Hills volcano, Montserrat, *Geophysical Research Letters*, *33*(10). 1, 1.3, 1.3, 1.4

Hammer, J., K. Cashman, R. Hoblitt, and S. Newman (1999), Degassing and microlite crystallization during pre-climactic events of the 1991 eruption of Mt. Pinatubo, Philippines, *Bulletin of Volcanology*, *60*(5), 355–380. 1.1

Hautmann, S., J. Gottsmann, R. S. J. Sparks, A. Costa, O. Melnik, and B. Voight (2009), Modelling ground deformation caused by oscillating overpressure in a dyke conduit at Soufrière Hills Volcano, Montserrat, *Tectonophysics*, *471*(1), 87–95. 1.3

Heap, M. J., M. Villeneuve, F. Albino, J. I. Farquharson, E. Brothelande, F. Amelung, J.-L. Got, and P. Baud (2020), Towards more realistic values of elastic moduli for volcano modelling, *Journal of Volcanology and Geothermal Research*, *390*, 106,684. 1.3

Hickey, J., and J. Gottsmann (2014), Benchmarking and developing numerical finite element models of volcanic deformation, *Journal of Volcanology and Geothermal Research*, *280*, 126–130. 1.6

Jaupart, C., and C. J. Allègre (1991), Gas content, eruption rate and instabilities of eruption regime in silicic volcanoes, *Earth and Planetary Science Letters*, *102*(3-4), 413–429. 1.5

Johnson, J. H., M. P. Poland, K. R. Anderson, and J. Biggs (2019), A cautionary tale of topography and tilt from kīlauea caldera, *Geophysical Research Letters*, *46*(8), 4221–4229. 1.3, 1.6

Klug, C., and K. V. Cashman (1996), Permeability development in vesiculating magmas: implications for fragmentation, *Bulletin of Volcanology*, *58*(2-3), 87–100. 1.1

Llewellin, E., and M. Manga (2005), Bubble suspension rheology and implications for conduit flow, *Journal of Volcanology and Geothermal Research*, *143*(1), 205–217. 1.5

Llewellin, E., H. Mader, and S. Wilson (2002), The constitutive equation and flow dynamics of bubbly magmas, *Geophysical research letters*, *29*(24). 1.5

Mader, H., E. Llewellin, and S. Mueller (2013), The rheology of two-phase magmas: A review and analysis, *Journal of Volcanology and Geothermal Research*, *257*, 135–158. 1.1

Maron, S. H., and P. E. Pierce (1956), Application of Ree-Eyring generalized flow theory to suspensions of spherical particles, *Journal of colloid science*, *11*(1), 80–95. 1.1

Massol, H., and C. Jaupart (2009), Dynamics of magma flow near the vent: Implications for dome eruptions, *Earth and Planetary Science Letters*, *279*(3-4), 185–196. 1.6

McTigue, D., and P. Segall (1988), Displacements and tilts from dip-slip faults and magma chambers beneath irregular surface topography, *Geophysical Research Letters*, *15*(6), 601–604. 1.3

Medina, L. N., D. F. Arcos, and M. Battaglia (2017), Twenty years (1990–2010) of geodetic monitoring of Galeras volcano (Colombia) from continuous tilt measurements, *Journal of Volcanology and Geothermal Research*. 1.2, 1.3

Melnik, O., and R. Sparks (1999), Nonlinear dynamics of lava dome extrusion, *Nature*, *402*(6757), 37. 1, 1.1, 1.4, 1.5

Melnik, O., and R. Sparks (2005), Controls on conduit magma flow dynamics during lava dome building eruptions, *Journal of Geophysical Research: Solid Earth*, *110*(B2). 1.5

Mogi, K. (1958), Relations between the eruptions of various volcanoes and the deformations of the ground surfaces around them, *Bulletin of the Earthquake Research Institute, University of Tokyo*, *36*, 99–134. 1.2, 1.3

Mothes, P. A., H. A. Yepes, M. L. Hall, P. A. Ramón, A. L. Steele, and M. C. Ruiz (2015), The scientific–community interface over the fifteen-year eruptive episode of Tungurahua Volcano, Ecuador, *Journal of Applied Volcanology*, *4*(1), 9. 1.2

Neuberg, J., H. Tuffen, L. Collier, D. Green, T. Powell, and D. Dingwell (2006), The trigger mechanism of low-frequency earthquakes on Montserrat, *Journal of Volcanology and Geothermal Research*, *153*(1), 37–50. (document), 1, 1.1, 1.3, 1.3.1, 1.4

Neuberg, J. W., A. S. Collinson, P. A. Mothes, M. C. Ruiz, and S. Aguaiza (2018), Understanding cyclic seismicity and ground deformation patterns at volcanoes: Intriguing lessons from Tungurahua volcano, Ecuador, *Earth and Planetary Science Letters*, *482*, 193–200. 1, 1.3, 1.3.1, 1.3.1, 1.3.1, 1.4, 1.4, 1.6

Nishimura, T. (2009), Ground deformation caused by magma ascent in an open conduit, *Journal of Volcanology and Geothermal Research*, *187*(3), 178–192. 1.4

Okumura, S., and T. Kozono (2017), Silicic lava effusion controlled by the transition from viscous magma flow to friction controlled flow, *Geophysical Research Letters*, *44*(8), 3608–3614. 1.5

Okumura, S., M. Nakamura, A. Tsuchiyama, T. Nakano, and K. Uesugi (2008), Evolution of bubble microstructure in sheared rhyolite: Formation of a channel-like bubble network, *Journal of Geophysical Research: Solid Earth*, *113*(B7). 1.1

Papale, P. (1999), Strain-induced magma fragmentation in explosive eruptions, *Nature*, *397*(6718), 425. 1.1, 1.5

Sparks, R. S. J. (1997), Causes and consequences of pressurisation in lava dome eruptions, *Earth and Planetary Science Letters*, *150*(3-4), 177–189. 1.3, 1.4

Spera, F. J. (2000), Physical properties of magma, *Encyclopedia of volcanoes*, *176*. 1.1

Taltavull, C., J. Dean, and T. W. Clyne (2016), Adhesion of volcanic ash particles under controlled conditions and implications for their deposition in gas turbines, *Advanced Engineering Materials*, *18*(5), 803–813. 1.6

Thomas, M. E., and J. Neuberg (2012), What makes a volcano tick-A first explanation of deep multiple seismic sources in ascending magma, *Geology*, *40*(4), 351–354. 1.5

Thomas, M. E., and J. W. Neuberg (2014), Understanding which parameters control shallow ascent of silicic effusive magma, *Geochemistry, Geophysics, Geosystems*, *15*(11), 4481–4506. 1.1, 1.5, 1.6

Toksöz, M., D. H. Johnston, and A. Timur (1979), Attenuation of seismic waves in dry and saturated rocks: I. laboratory measurements, *Geophysics*, *44*(4), 681–690. 1.3.1

Truby, J., S. Mueller, E. Llewellin, and H. Mader (2015), The rheology of three-phase suspensions at low bubble capillary number, in *Proc. R. Soc. A*, vol. 471, p. 20140557, The Royal Society. 1.1

Tsvetkova, Y. D., and O. Melnik (2018), The influence of non-newtonian properties of magma on flow in a volcanic conduit, in *Doklady Physics*, vol. 63, pp. 485–488, Springer. 1.5

Tuffen, H., and D. Dingwell (2005), Fault textures in volcanic conduits: evidence for seismic trigger mechanisms during silicic eruptions, *Bulletin of Volcanology*, *67*(4), 370–387. 1.4

Tuffen, H., D. B. Dingwell, and H. Pinkerton (2003), Repeated fracture and healing of silicic magma generate flow banding and earthquakes?, *Geology*, *31*(12), 1089–1092. 1.3.1

Voight, B., R. Hoblitt, A. Clarke, A. Lockhart, A. Miller, L. Lynch, and J. McMahon (1998), Remarkable cyclic ground deformation monitored in real-time on Montserrat, and its use in eruption forecasting, *Geophysical Research Letters*, *25*(18), 3405–3408. 1.2

Voight, B., R. Sparks, A. Miller, R. Stewart, R. Hoblitt, A. Clarke, J. Ewart, W. Aspinall, B. Baptie, E. Calder, et al. (1999), Magma flow instability and cyclic activity at Soufrière Hills Volcano, Montserrat, British West Indies, *Science*, *283*(5405), 1138–1142. 1, 1.3

Widiwijayanti, C., A. Clarke, D. Elsworth, and B. Voight (2005), Geodetic constraints on the shallow magma system at Soufrière Hills Volcano, Montserrat, *Geophysical Research Letters*, *32*(11). 1, 1.3, 1.3

Wilson, L., R. S. J. Sparks, and G. P. Walker (1980), Explosive volcanic eruptionsiv. the control of magma properties and conduit geometry on eruption column behaviour, *Geophysical Journal International*, *63*(1), 117–148. 1.5

Zobin, V. M., H. Santiago-Jiménez, J. J. Ramírez-Ruiz, G. A. Reyes-Dávila, M. Bretón-González, and C. Navarro-Ochoa (2007), Quantification of volcanic explosions from tilt records: Volcán de Colima, México, *Journal of Volcanology and Geothermal Research*, *166*(2), 117–124. 1.2

Chapter 2

Combining magma flow and deformation modelling to explain observed changes in tilt

L. Marsden[1], J. Neuberg[1], M. Thomas[1], P. Mothes[2] and M. Ruiz [2]

[1] *School of Earth and Environment, University of Leeds, Leeds, United Kingdom*
[2] *Instituto Geofisico, Escuela Politécnica Nacional, Quito, Ecuador*

Citation: **Marsden, L. H.**, Neuberg, J., Thomas, M., Mothes, P., and Ruiz, M. (2019). *Combining magma flow and deformation modelling to explain observed changes in tilt.* Frontiers in Earth Science 7, 219

Abstract

The understanding of magma ascent dynamics is essential in forecasting the scale, style and timing of volcanic eruptions. The monitoring of near-field deformation is widely used to gain insight into these dynamics, and has been linked to stress changes in the upper conduit. The ascent of magma through the conduit exerts shear stress on the conduit wall, pulling up the surrounding edifice, whilst overpressure in the upper conduit pushes the surrounding edifice outwards. How much shear stress and pressure is produced during magma ascent, and the relative contribution of each to the deformation, has until now only been explored conceptually. By combining flow and deformation modelling using COMSOL Multiphysics, we for the first time present a quantitative model that links magma ascent to deformation. We quantify how both shear stress and pressure vary spatially within a cylindrical conduit, and show that shear stress generally dominates observed changes in tilt close to the conduit. However, the relative contribution of pressure is not insignificant, and both pressure and shear stress must be considered when interpreting deformation data. We demonstrate that significant changes in tilt can be driven by changes in the driving pressure gradient or volatile content of the magma. The relative contribution of shear stress and pressure to the tilt varies considerably depending on these parameters. Our work provides insight into the range of elastic moduli that should be considered when modelling edifice-scale rock masses, and we show that even where the edifice is modelled as weak, shear stress generally dominates the near field deformation over pressurisation of the conduit. While our model addresses cyclic tilt changes observed during activity at Tungurahua volcano, Ecuador, between 2013 and 2014, it is also applicable to silicic volcanoes in general.

2.1 Introduction

Being able to understand what drives temporal variations in seismicity and deformation at volcanoes is essential in interpreting how volcanic systems evolve through time. Tiltmeters are sensitive to deformation, and at basaltic volcanoes they have long since been used to infer pressure changes in a shallow magma reservoir (e.g. *Hreinsdóttir et al.*, 2014). More recently at silicic volcanoes, tiltmeters deployed close to the summit of the volcano have been used to infer pressure variations in or surrounding a volcanic conduit. However, modelling of such deformation by realistic pressure variations often requires the source radius to far exceed that of the assumed conduit (e.g. *Voight et al.*, 1999). Therefore, shear stress has been suggested in several studies as an alternative source of deformation (*Neuberg et al.*, 2018, *Beauducel et al.*, 2000, *Green et al.*, 2006).

The ascent of highly viscous magma generates sustained shear traction at the conduit walls, which pulls up the surrounding edifice and causes deformation at the surface. It thereby provides an important link between ascent dynamics and deformation (Fig-

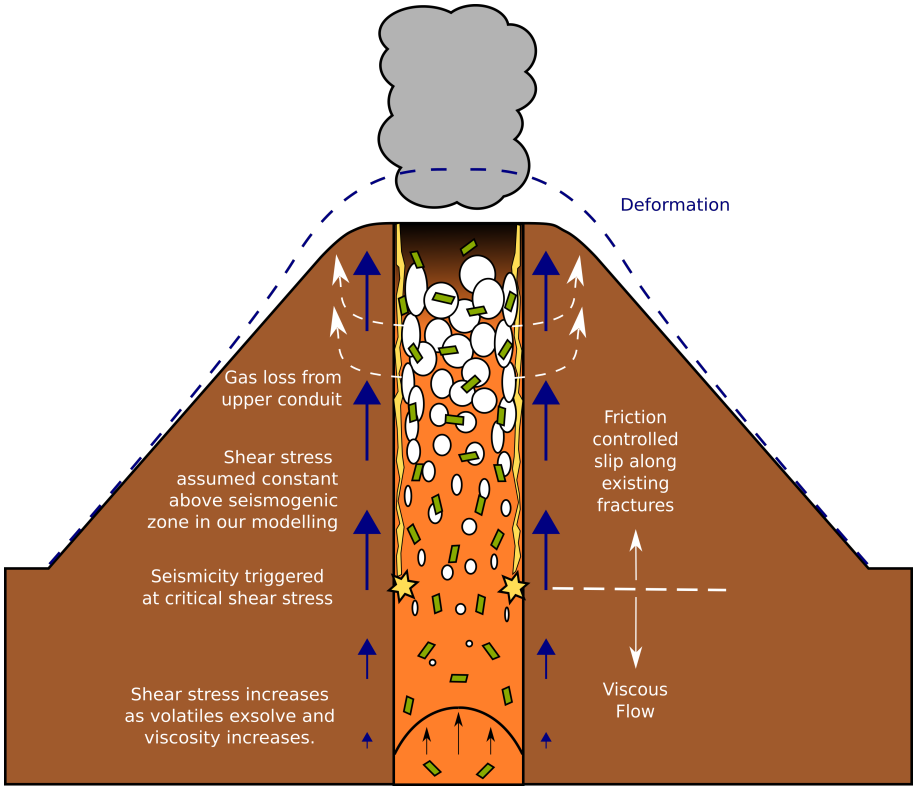

Figure 2.1: Schematic diagram illustrating how as magma ascends, shear stress is exerted on the conduit walls, inducing deformation. Shear fractures form where the shear stress reaches a critical threshold, triggering low frequency seismicity. Once formed, these fractures move up with the ascending magma, allowing friction controlled slip along them. The shear stress cannot exceed this critical threshold at which brittle failure is induced. The total shear stress is partitioned between low frequency seismicity and the deformation.

ure 2.1). Shear stress σ_s is a function of the ascent velocity v_z and viscosity η of the magma, such that

$$\sigma_s = \dot{\varepsilon}\eta = \frac{dv_z}{dr}\eta \tag{2.1}$$

where $\dot{\varepsilon}$ is strain rate, which can be written as dv_z/dr, the lateral gradient of the magma ascent velocity across the conduit (*Neuberg et al.*, 2006). r is the horizontal distance from the centre of the conduit. Therefore, if deformation is driven predominantly by a shear stress source, and the viscosity of the magma and the mechanical properties of the edifice are known, the amount of deformation can be used to estimate the ascent velocity of the magma, a vital parameter in forecasting eruption style.

Where shear stress reaches a critical value, brittle failure of the melt occurs, triggering low frequency seismicity (*Neuberg et al.*, 2006). Brittle failure occurs where the shear stress σ_s is greater than the shear strength of the magma, τ_m. Shear stress in the conduit cannot exceed the value at which magma fractures, hence the shear stress is limited by the shear strength at the depth that low frequency seismicity is observed.

There have been several attempts to conceptually link the shear stress or pressure necessary to achieve observed deformation as magma ascends. *Green et al.* (2006) showed that shear stress of 0.5 MPa in the upper 1 km of the conduit can explain tilt of 20 μrad at the tiltmeter at Chances Peak, Soufriére Hills volcano, Montserrat, whereas a pressure in excess of 40 MPa is required to model the same tilt using a realistic conduit radius. More recently, *Neuberg et al.* (2018) showed that shear stress of 20 MPa along a 4.5 km conduit can explain 480 μrad of tilt at the RETU tiltmeter at Tungurahua, Ecuador, whereas an overpressure of several hundreds of MPa would be required. However, the key question remains whether such stress levels are achieved and sustained in a volcanic conduit during ascent of magma, or how shear stress and pressure vary both spatially and temporally within a conduit as a result of various volcanic phenomena.

Through flow modelling, it is possible to simulate realistic magma ascent, where the governing parameters are based on results of several disciplines within volcanology. This allows us to quantify how both pressure and shear stress vary within a volcanic conduit. *Thomas and Neuberg* (2012) showed that variations in conduit geometry can significantly increase the shear stress locally to potentially induce seismicity through brittle failure of magma, and in further work (*Thomas and Neuberg*, 2014) identified volatile content and the driving pressure gradient as key parameters in modulating the ascent dynamics and therefore shear stress and pressure. *Okumura and Kozono* (2017) demonstrated that the transition from viscous flow to friction-controlled slip occurs at a greater depth if the crystal content is higher, as strain localises in the melt phase where crystals are assumed rigid. However, there is a significant mismatch between the shear stress and pressure values obtained in these studies and the values required in modelling to explain the observed deformation. Shear stress on the order of MPa is only modelled in the uppermost section of the conduit if at all. This poses the question; can shear stress sufficient to explain observed deformation realistically be achieved during magma ascent?

Despite advances in both flow and deformation modelling, few studies have attempted to couple the two. One exception by *Albino et al.* (2011) demonstrated that the formation of a viscous plug can lead to a localised increase in shear stress in the upper part of the conduit, and induce near-field deformation. By using a simple step function to define the viscosity as a function of depth, due to the plug and underlying magma, they also obtained a step function for shear stress as a function of depth. In reality, the melt viscosity increases gradually as magma ascends and volatiles exsolve.

Moving on from these studies, we investigate whether observed deformation can be explained using realistic depth-dependent pressure and shear stress profiles, obtained through flow modelling. Here, we build upon the 3 phase, 2D axisymmetric flow models of *Collier and Neuberg* (2006) and *Thomas and Neuberg* (2014) to simulate more realistic conditions during ascent of magma through a cylindrical conduit. From this, we

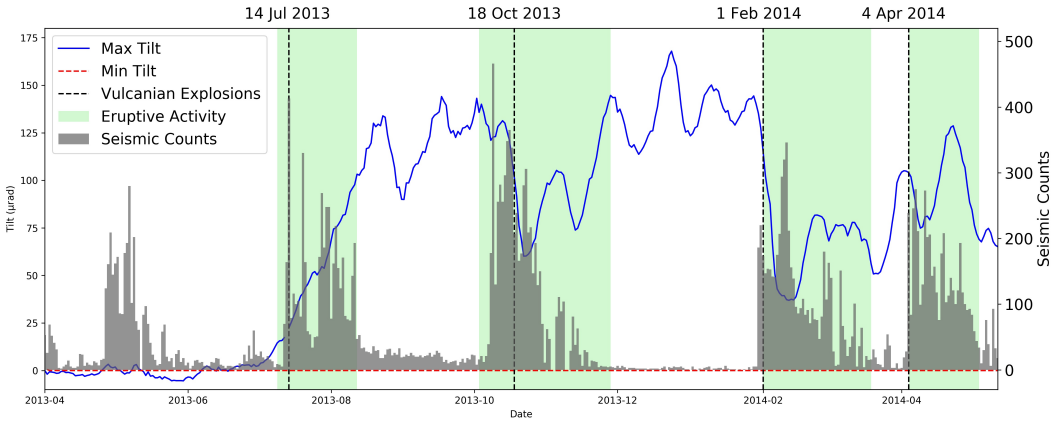

Figure 2.2: Daily averaged tilt (μrad) and long-period seismic event count recorded at RETU. Each marked period of eruptive activity includes a single Vulcanian explosion.

obtain depth-dependent pressure and shear stress profiles at the conduit-edifice boundary, which we use to drive our deformation modelling. In doing so, we for the first time provide a quantitative model that links magma ascent to observed deformation.

A reference conduit flow model is developed in Section 2.2, with parameters based on Tungurahua volcano, Ecuador, where between July 2013 and June 2014, 4 Vulcanian explosions coincided with cyclic tilt variations of around 170 μrad, recorded at RETU (Figure 2.2), located 1 km vertically and 2 km laterally from the summit (Figure 2.3). In Figure 2.2, we present the maximum tilt, defined as the modulus of the X and Y components of the tilt. The directions of maximum and minimum tilt are perpendicular to each other. Due to factors such as topography, the maximum tilt is not necessarily radial from the source (*Johnson et al.*, 2019). Other tiltmeters deployed further down the flanks at Tungurahua are not sensitive to stress changes in or around the conduit (*Neuberg et al.*, 2018). This striking correlation between the tilt and activity is seldom seen at volcanoes, as for logistical reasons tiltmeters are rarely deployed at such close proximity to the conduit at silicic volcanoes with considerable relief. However, even a single strategically deployed tiltmeter can be an invaluable addition to a monitoring network. A considerable decrease in tilt at RETU, alongside an increase in low frequency seismicity, was used to forecast that an eruption was imminent at Tungurahua 3 days prior to the Vulcanian explosion on February 1st, 2014 (*Mothes et al.*, 2015). Supplementary information regarding the flow model is included in the sections A.1, A.3, A.4. In Section 2.2.4, we present depth-dependent pressure and shear stress profiles extracted from our reference flow model, and use these to drive our deformation models in Section 2.3. Finally, in Section 2.4 we quantify how realistic changes in key parameters, such as the volatile content or driving pressure gradient, can influence pressure, shear stress and therefore tilt through time. We demonstrate how independently inferred processes, such as the gradual solidification of a viscous plug (*Hall et al.*, 2015) or the injection of a volatile rich batch of magma at depth (*Samaniego et al.*, 2011,

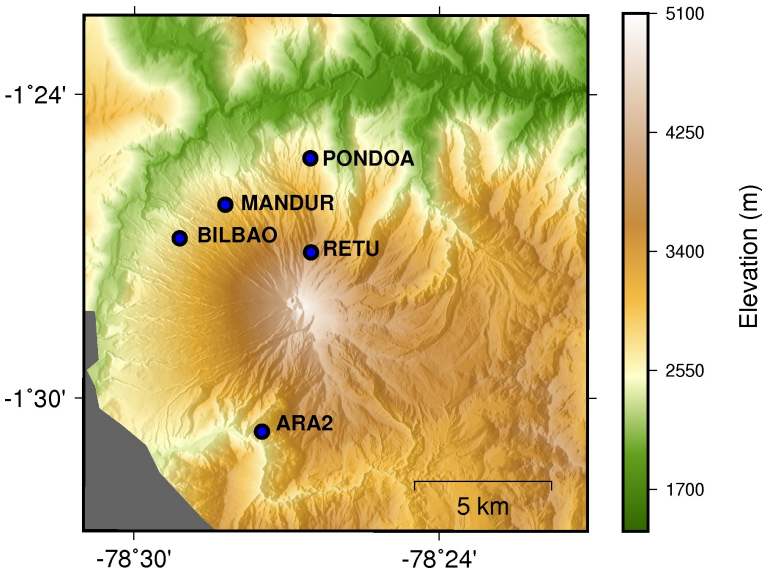

Figure 2.3: Elevation map showing the location of tiltmeters deployed at Tungurahua volcano (blue dots). Note that due to its proximity to the conduit, only RETU is sensitive to changes in stress in the conduit (*Neuberg et al.*, 2018).

Andújar et al., 2017), can explain both the amplitude and variations in tilt during the 2013-4 activity at Tungurahua. However, whilst we use observed data at Tungurahua to constrain the model, our findings provide important insight into the source of near-field deformation at silicic volcanoes in general.

2.2 Flow model set-up

The 2D axisymmetric flow modelling in this project builds upon the work of *Collier and Neuberg* (2006) and *Thomas and Neuberg* (2014), and is performed using the Laminar Flow Module in the finite element software COMSOL Multiphysics 5.3. 1D models have been used successfully to discern volcanic phenomena such as lava dome extrusion (*Melnik and Sparks*, 1999) and plug formation (*Diller et al.*, 2006). However, other authors have highlighted the importance of radial changes within conduit flow models (*Llewellin and Manga*, 2005, *Collier and Neuberg*, 2006), and quasi 2D models of *Tsvetkova and Melnik* (2018) have recently showed that the dependence of shear rate on viscosity and therefore ascent dynamics can be significant. The magma is considered a three-phase fluid comprising gas, crystals and melt. While the melt is treated as a Newtonian fluid, the magma viscosity is modulated by the gas and crystal content and strain rate. A cylindrical conduit is represented in 2D axial symmetric domain space as a rectangle, through which isothermal magma ascent is governed by the compressible form of the Navier-Stokes equation

$$\rho\frac{d\mathbf{v}}{dt} + \rho\mathbf{v}\cdot\nabla\mathbf{v} = -\nabla P + \nabla\cdot\left(\eta\left[\nabla\mathbf{v} + (\nabla\mathbf{v})^T\right] - \frac{2}{3}\eta\left[\nabla\cdot\mathbf{v}\right]I\right) + \mathbf{F} \qquad (2.2)$$

and the continuity equation

$$\frac{d\rho}{dt} + \nabla \cdot (\rho \mathbf{v}) = 0 \tag{2.3}$$

where ρ is density, $\mathbf{v}$ is the velocity vector, P is pressure, η is the viscosity, $\mathbf{F}$ is a volume force vector, in this case gravity, and I is the identity tensor (*Faber*, 1995). We solve for an equilibrium solution, and time dependent terms $\rho\frac{d\mathbf{v}}{dt}$ and $\frac{d\rho}{dt}$ are discarded.

Typically, finite element models use an unstructured mesh (for example a triangular mesh). However, as a simple cylindrical geometry is used for the conduit, a rectangular 'mapped' mesh is employed in this case, providing improved stability to the model solver. This allows larger spatial variations in parameters to be modelled, which would face convergence issues when using a unstructured mesh. A mesh refinement study was performed to determine the mesh resolution close to the conduit wall required to model a solution for the shear stress at the conduit wall that is independent of the mesh size. An minimum element size as small as 2 cm at the conduit wall was applied in some tests, increasing towards the conduit centre.

A summary of the parameters used in the flow model is presented in Table 2.1. A no-slip boundary condition is applied at the conduit wall. Pressure boundary conditions are set at the top and base of the conduit as atmospheric and magmastatic plus overpressure, respectively. ρ_e is the density of the edifice surrounding the conduit, g is acceleration due to gravity, z_c is the depth in the conduit, P_a is atmospheric pressure, and P_e is excess pressure at the base of the conduit, which is varied between tests (section 2.4) to account for overpressure in the system.

$$P = P_a + \rho_e g z_c + P_e \tag{2.4}$$

2.2.1 Magma rheology

Magma is typically a multiphase suspension consisting of silicate melt, crystals and bubbles. The relative proportion of these three phases significantly influences the magma rheology, and therefore the eruption dynamics (*Dingwell*, 1996). Silicic melt is often assumed to behave as a Newtonian fluid, where the viscosity η_0 is constant (e.g. *Truby et al.*, 2015). However, at moderate crystal and gas fractions, the apparent viscosity of the suspension η_s is a function of the shear stress σ_s and strain rate $\dot{\varepsilon}$, such that $\eta_s = \sigma_s/\dot{\varepsilon}$ (*Mueller et al.*, 2011). This is often normalised by the viscosity of the suspending melt η_0, to give the relative viscosity as $\eta_r = \eta_s/\eta_0$.

The viscosity of the melt phase has been determined as a function of melt composition and temperature, using the model by *Giordano et al.* (2008). The melt composition we use has been obtained by *Myers et al.* (2014) from averaging the composition of matrix glass from scoria bombs of the 2010 eruption of Tungurahua (Table 2.2).

Symbol	Variable	Values in reference model [range considered]	Reference
τ_m	Shear strength of magma	1 MPa	*Okumura et al.* (2010)
T	Magma temperature	950 °C [850,1000 °C]	*Samaniego et al.* (2011)
r_p	Crystal aspect ratio	3 [1,20]	
Γ	Bubble surface tension	0.073 N/m	*Gardner et al.* (2013)
R_c	Conduit radius	10 m	*Ruiz et al.* (2006)
L	Conduit length	5 km	*Molina et al.* (2005)
C_g	Ideal gas constant	8.314 J K^{-1} mol^{-1}	
n_b	Bubble number density	1×10^{10} m^{-3}	*Cluzel et al.* (2008)
P	Pressure		
P_a	Atmospheric pressure	0.1 MPa	
P_e	Excess pressure at conduit base	20 MPa **[0,20 MPa]**	*Sparks* (1997)
ρ_e	Density of edifice	2650 kg/m^3	*Hall et al.* (1999)
ρ_{plag}	Density of plagioclase crystals	2570 kg/m^3	*Burgisser et al.* (2010)
ρ_{opx}	Density of orthopyroxene crystals	3300 kg/m^3	*Burgisser et al.* (2010)
ρ_{cpx}	Density of clinopyroxene crystals	3300 kg/m^3	*Burgisser et al.* (2010)
ρ_c	Average crystal density	Eq. 2.18	
ρ_b	Bulk density of magma	Eq. 2.17	*Spera* (2000)
ϕ_{plag}	Plagioclase crystals volume fraction	17 vol.%	*Romero et al.* (2017)
ϕ_{opx}	Orthopyroxene crystals volume fraction	2 vol.%	*Romero et al.* (2017)
ϕ_{cpx}	Clinopyroxene crystals volume fraction	10 vol.%	*Romero et al.* (2017)
ϕ_c	Crystal volume fraction	29 vol.% [10,50 vol.%]	$\phi_{plag} + \phi_{opx} + \phi_{cpx}$
ϕ_c^{sph}	Max. packing fraction spherical particles	0.656	*Mueller et al.* (2011)
ϕ_c^{max}	Max. packing fraction	0.595 [Eq. 2.5]	*Mueller et al.* (2011)
b	Fitting parameter in Eq. 2.5	1.08	*Mueller et al.* (2011)
C_{wi}	Initial H_20 content	5 wt.% **[0,10** wt.%]	*Andújar et al.* (2017), *Samaniego et al.* (2011), *Myers et al.* (2014)
g	Acceleration due to gravity	9.81 m/s^2	
K	Constant in Eq. 2.14	6/5	*Mader et al.* (2013)
σ_s	Shear stress	Eq. 2.1	*Neuberg et al.* (2006)
v_z	Ascent velocity		
r	Horizontal distance from centre of source		
z	Vertical distance from conduit centre		
z_c	Depth in conduit		
$\dot{\varepsilon}$	Strain rate	dv_z/dr	
η_0	Melt viscosity	Spatially variant	*Giordano et al.* (2008), *Myers et al.* (2014)
η_s	Apparent viscosity	$\sigma_s/\dot{\varepsilon}$	*Mueller et al.* (2011)
η_r	Relative viscosity	η_s/η_0	*Mueller et al.* (2011)
η_{rc}	Relative viscosity crystal-bearing magma	Eq. 2.6	*Maron and Pierce* (1956)
C_w	Weight percent of dissolved H_2O	Eq. 2.7	*Zhang et al.* (2007)
n	Number of moles of exsolved H_20	Eq. 2.8	
M	Molar mass of H_20	0.018 kg	
V_g	Volume of exsolved H_20	Eq. 2.9	
ϕ_g	Gas volume fraction	Eq. 2.10	
ϕ_m	Initial melt fraction	$1 - \phi_c$	
η_{r0}	Zero shear-rate viscosity bubbly magma	Eq. 2.12	*Llewellin and Manga* (2005)
η_{rg}	Infinite shear-rate viscosity bubbly magma	Eq. 2.13	*Llewellin and Manga* (2005)
$\eta_{r\infty}$	Relative viscosity bubbly magma	Eq. 2.14	*Mader et al.* (2013)
m	Constant in Eq. 2.14	2	*Mader et al.* (2013)
η_{rgc}	Relative viscosity three-phase suspension	Eq. 2.16	
Ca	Capillary number	Eq. 2.11	*Rust and Manga* (2002)
R_b	Bubble radius	Eq. A.3	*Lensky et al.* (2002)

Table 2.1: Parameters and variables used in the flow model, based on Tungurahua volcano, Ecuador. Range of values tested in Section 2.4 in bold.

	Sample 1	Sample 2	Sample 3	Average
SiO_2	62.01	61.71	60.58	61.43
TiO_2	1.28	1.26	1.28	1.27
Al_2O_3	15.77	15.70	15.81	15.76
FeO^T	6.40	6.47	6.78	6.55
MnO	0.10	0.07	0.09	0.09
MgO	2.17	2.25	2.48	2.30
CaO	4.70	4.89	5.14	4.91
Na_2O	4.01	4.12	4.48	4.20
K_2O	3.26	3.13	2.97	3.12
P_2O_5	0.30	0.39	0.40	0.36

Table 2.2: Composition of melt phase, from matrix glass of scoria clasts from the 2010 eruption at Tungurahua volcano (*Myers et al.*, 2014)

Crystal bearing magma

Crystals increase the viscosity of magma due to energy being dissipated through fluid-particle and particle-particle interactions. The relative viscosity increases exponentially as the crystal content increases, approaching the maximum packing fraction, at which point the suspension becomes jammed (*Mueller et al.*, 2011). More elongate crystals with a higher aspect ratio encompass a larger area during rotation, hence, enhance the particle-particle interactions. From experiments on suspensions of particles over a range of aspect ratios, *Mueller et al.* (2011) derived the following empirical relationship between the maximum packing fraction ϕ_c^{max} and the particle aspect ratio r_p.

$$\phi_c^{max} = \phi_c^{sph} \exp\left[-\frac{(\log_{10} r_p)^2}{2b^2}\right] \tag{2.5}$$

where the maximum packing fraction for spherical particles $\phi_c^{sph} = 0.656$, and a fitting parameter $b = 1.08$, have each been experimentally derived by *Mueller et al.* (2011). Here, where we assume an aspect ratio of 3 for a predominantly plagioclase and pyroxene crystal phase, $\phi_c^{max} = 0.595$. *Mueller et al.* (2011) found empirically that for diverse crystal suspensions over a range of values for r_p, η_r and the crystal volume fraction of the suspension ϕ_c, that the theoretical model of *Maron and Pierce* (1956) is able to accurately describe the relative viscosity, hence the rheology.

$$\eta_{rc} = \eta_r \left(1 - \frac{\phi_c}{\phi_c^{max}}\right)^{-2} \tag{2.6}$$

Romero et al. (2017) assessed thin sections of pyroclastic density current blocks from the February 2014 eruption on Tungurahua, and estimated the crystal volume fraction as $\phi_c = 0.29$. For simplicity, we proceed with the constant value of $\phi_c = 0.29$ in all our models, making the assumption that the ascent time is short relative to the time period of crystallisation. Using this value, the relative viscosity of the crystal-bearing suspension η_{rc} is a factor of 4 greater than the relative viscosity of the melt phase η_r.

Bubbly magma

The gas volume fraction at any point in the conduit is a function of the solubility of volatiles in the melt, the initial content dissolved in the melt at depth, and the amount of gas that has been able to escape from the system. In our models, we consider only H_2O as the most volumetrically significant volatile phase that exsolves from the melt, and use the law from *Zhang et al.* (2007) to determine the weight percent of H_2O, C_w, dissolved in the melt phase:

$$C_w = \left(-0.231 + \frac{651.1}{T}\right)\sqrt{P} + \left(0.03424 - \frac{32.57}{T} + 0.02447AI\right)P \tag{2.7}$$

where T is temperature in degrees Kelvin, P is pressure in MPa, and AI is the sum of the mole fractions of Na, K and Al.

An upper limit is placed upon C_w from estimates of the initial concentration of water dissolved in the melt. *Myers et al.* (2014) found that melt inclusions from eruptions in 2006 and 2010 contained as much as 4 wt.% H_2O. *Samaniego et al.* (2011) performed a petrological analysis of juvenile blocks and bombs from pyroclastic flow deposits of the 2006 paroxysmal eruptions at Tungurahua. They stated that the observed absence of amphibole suggests that the magmas evolved at a H_2O content less than 4 wt.%, and temperatures higher than 950-1000 °C. *Andújar et al.* (2017) propose that prior to the July 2006 eruption magma was stored at 400 MPa, at 1000 °C, with an H_2O content of 6 wt.%, before ascending to a second storage reservoir at 200 MPa. For our reference model, we use an initial H_2O content of 5 wt.%, and assess how varying this value by ±5 wt.% influences the ascent dynamics and associated deformation in Section 2.4.

Eq. 2.7 is valid where the water content dissolved in the melt is in equilibrium with the exsolved water, and assumes instantaneous and homogeneous nucleation and exsolution. This yields a sharp variation in C_w at the nucleation depth. A more gradual onset of exsolution is probably more realistic, and has been implemented by applying a taper function as shown in the supplementary section A.3 (Eq. A.6).

Eq. 2.7 provides the mass fraction of H_2O that has been exsolved. However, the gas volume fraction ϕ_g depends on the gas density, which is also pressure and therefore depth dependent. To quantify how ϕ_g varies with depth, first the number of moles of exsolved H_2O per cubic metre, n, must be calculated using the melt density ρ_m and the molar mass of H_2O, $M = 0.018$ kg

$$n = \frac{C_w \rho_m}{M} \tag{2.8}$$

The volume of exsolved H_2O, V_g, can then be calculated using the ideal gas equation:

$$V_g = \frac{nC_gT}{P} \tag{2.9}$$

where T is temperature in degrees Kelvin, P is pressure in MPa and C_g is the ideal

gas constant. The volume of melt from which gas exsolves is reduced by the fraction of crystals within the magma, therefore, V_g is weighted by the initial melt fraction, $\phi_m = 1 - \phi_c$. The gas volume fraction, ϕ_g, is calculated by

$$\phi_g = \frac{V_g \phi_m}{V_g \phi_m + \phi_m + \phi_c}. \tag{2.10}$$

The efficiency by which exsolved volatiles can be released from a volcanic system plays a fundamental role on controlling the eruption style. The gas volume fraction remaining in the magma is a key factor in determining whether magma fragmentation occurs, and therefore whether a subsequent eruption is effusive or explosive (*Dingwell*, 1996). Additionally, the remaining gas content influences both the viscosity (*Llewellin and Manga*, 2005) and density (*Spera*, 2000) of the bulk magma, and therefore provides a top-down control on the magma ascent rate (*Thomas and Neuberg*, 2014). Therefore, it is important to be able to quantify how much gas is lost from the system.

Independent ascent of bubbles through magma is not considered in this highly viscous system, and therefore gas is assumed to be lost only through permeable flow. Permeable gas flow occurs where the porosity is sufficient for bubbles to be interconnected (*Klug and Cashman*, 1996). Additionally, gas loss may be facilitated by fractures in the magma (*Gaunt et al.*, 2014). The minimum porosity required for degassing is unclear and varies with crystal volume fraction and strain rate (*Laumonier et al.*, 2011). Also, it is unclear how magma permeability and degassing vary with depth. Therefore, in this study, a simplified forced degassing approach is adopted, where an empirical permeability depth profile is provided. We assume that no permeable degassing pathways exist where $\phi_g < 0.2$, a reasonable compromise based on results of several studies (see the supplementary section A.4). This corresponds to a depth of 1600 m in the reference model. This depth is then set as the maximum depth of degassing in all future models. This was derived by iteratively adjusting the maximum gas loss depth and assessing the ϕ_g depth profile. We assume that all the gas is lost at the surface, to simulate in our flow model the presence of an impermeable plug in the upper conduit (*Hall et al.*, 2015). This is supported by observations of negligible outgassing during periods of quiescence at the Tungurahua (*Hidalgo et al.*, 2015). A cosine taper is used for the gas loss profile to achieve a smooth variation with depth. Our resultant profile for the gas volume fraction is in line with the numerical modelling of (*Diller et al.*, 2006), who showed that if the magma and surrounding edifice are permeable, a low vesicularity, dense region forms in the upper conduit.

Bubbles can either increase or decrease the relative viscosity of the bubble suspension η_{rg} depending on the capillary number Ca, a ratio of the viscous stresses deforming the bubble to the interfacial stresses restoring it (*Rust and Manga*, 2002)

$$Ca = \frac{\eta_0 R_b \dot{\varepsilon}}{\Gamma} \tag{2.11}$$

where Γ is the bubble surface tension and R_b is the bubble radius, where the computation of R_b is documented in the supplementary section A.1. Bubbles increase the relative viscosity η_rg by distorting the flow paths of the melt, and decrease η_rg by providing free-slip surfaces for flow. The zero shear-rate viscosity η_r0 and infinite shear rate viscosity $\eta_\mathrm{r\infty}$ describe the limits of the influence of bubbles on the viscosity, where the bubbles are considered spherical or at the limit of elongation respectively, and are functions of the gas volume fraction ϕ_g, as determined by *Llewellin and Manga* (2005) where ϕ_g is less than 0.5.

$$\eta_\mathrm{r0} = (1 - \phi_\mathrm{g})^{-1} \tag{2.12}$$

$$\eta_\mathrm{r\infty} = (1 - \phi_\mathrm{g})^{5/3} \tag{2.13}$$

The relative viscosity between η_r0 and $\eta_\mathrm{r\infty}$ can be defined using

$$\eta_\mathrm{rg} = \eta_\mathrm{r\infty} + \frac{\eta_\mathrm{r0} - \eta_\mathrm{r\infty}}{1 + KCa^m}, \tag{2.14}$$

where $K = 6/5$ and $m = 2$ (*Mader et al.*, 2013). η_rg tends asymptotically towards η_r0 at low strain rate, where the bubbles are spherical, and towards $\eta_\mathrm{r\infty}$ at high strain rate, where the bubbles approach the limit of elongation. Hence, spherical bubbles impede flow while elongate bubbles facilitate flow.

Three-phase magma

Three-phase suspension experiments from *Truby et al.* (2015) presented a model for the relative viscosity of three-phase magma. In this model, the bubble-bearing suspension is treated as the 'effective medium' in which crystals are suspended, and hence Eqs. 2.12 and 2.6 have been combined to provide the bulk viscosity.

$$\eta_\mathrm{rgc} = (1 - \phi_\mathrm{g})^{-1} \left(1 - \frac{\phi_\mathrm{c}}{\phi_\mathrm{c}^\mathrm{max}}\right)^{-2} \tag{2.15}$$

This equation has been tested only for steady flow in the low capillarity regime (spherical bubbles), for $0 \leq \phi_\mathrm{g} \leq 0.3$ and $0 \leq \phi_\mathrm{c} \leq 0.85$, however *Truby et al.* (2015) state that the model's applicability is potentially much broader, although subject to experimental validation. To our knowledge, this has not yet been done, nor has an alternative model been suggested for higher capillary numbers. By combining Eqs. 2.14 and 2.6, we extrapolate the trend so it is usable for higher capillary numbers.

$$\eta_\mathrm{rgc} = \left(\eta_\mathrm{r\infty} + \frac{\eta_\mathrm{r0} - \eta_\mathrm{r\infty}}{1 + KCa^m}\right) \left(1 - \frac{\phi_\mathrm{c}}{\phi_\mathrm{c}^\mathrm{max}}\right)^{-2} \tag{2.16}$$

Eq. 2.16 is used within our flow models to provide a spatially variant viscosity that

accounts for melt, crystals and bubbles.

Why the bulk viscosity needs to be scaled up

Eq. 2.16 provides us with a good representation of how the bulk magma viscosity varies spatially within the conduit. However, this describes the classical flow dynamics within a clean pipe. In reality, a volcanic conduit is filled with rubble from previous eruptions that ascending magma must percolate through and incorporate. For this reason, a Bingham rheology is often used (e.g. *Blake*, 1990), where a yield strength must be overcome for magma to ascend. Furthermore, based on the available data for Tungurahua, we must consider in our models a range of values for magma temperature, composition, crystal content and aspect ratio, resulting in significant uncertainties in the bulk viscosity. We adopt the concept of a Bingham rheology by scaling up the bulk viscosity derived in eq. 2.16 by a factor of 10 000, in order to yield suitable values for the ascent velocity (millimetres per second) that are low enough for magma to ascend from chamber depth (7.5-9.5 km, (*Samaniego et al.*, 2011)) to the surface without fragmentation over the three months between each Vulcanian explosion. Due to the large uncertainties in the bulk viscosity, we neglect a further fine-tuning that takes crystallisation during magma ascent into account (*Melnik and Sparks*, 2005).

2.2.2 Magma density

The density of the melt phase ρ_m has been calculated as a function of the composition (Table 2.2), pressure and temperature, as in *Spera* (2000), such that the melt density varies spatially within the conduit. The bulk density ρ_b is a function of the gas volume fraction ϕ_g and density ρ_g, and crystal volume fraction ϕ_c and density ρ_c.

$$\rho_b = \rho_m \phi_m (1 - \phi_g) + \rho_g \phi_g + \phi_c \rho_c (1 - \phi_g) \tag{2.17}$$

As H_2O is exsolved from the melt as it ascends, the melt density ρ_m increases, whilst the bulk magma density ρ_b decreases due to the increased gas volume fraction ϕ_g. The crystal volume fraction ϕ_c has been taken from estimates of *Romero et al.* (2017), who assessed thin sections from pyroclastic density current blocks from the February 2014 eruption on Tungurahua. The crystal assemblage was estimated to consist mainly of 17 % plagioclase (ϕ_{plag}), 10 % clinopyroxene (ϕ_{cpx}) and 2 % orthopyroxene (ϕ_{opx}). Approximations of the density of each crystal phase (ρ_{plag}, ρ_{cpx} and ρ_{opx}) have been taken from *Engineering Toolbox* (2018). Given that the density varies quite considerably within the pyroxene group, an average density of 3334 kg/m^3 is used for both ρ_{cpx} and ρ_{opx}. Using this information, we calculate the average crystal density ρ_c using

$$\rho_c = \rho_{plag} \frac{\phi_{plag}}{\phi_c} + \rho_{cpx} \frac{\phi_{cpx}}{\phi_c} + \rho_{opx} \frac{\phi_{opx}}{\phi_c}. \tag{2.18}$$

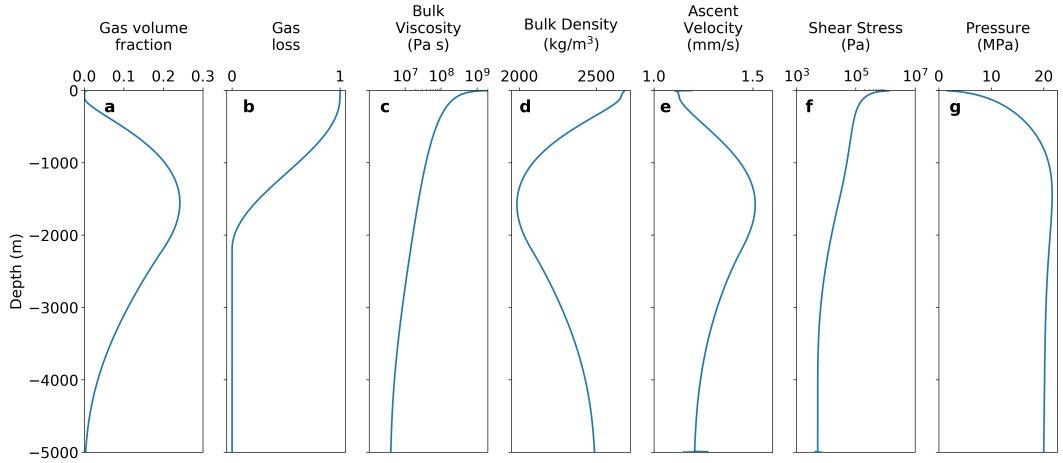

Figure 2.4: Depth profiles of key variables obtained from the reference flow model. **a** to **e** have been extracted from the centre of the conduit, **f** and **g** have been extracted from the conduit wall. Note that the shear stress profile has been clipped at 1 MPa to accommodate low frequency seismicity.

2.2.3 Accounting for seismicity

Brittle failure of the magma occurs where the shear stress exceeds the shear strength of the magma, triggering low frequency seismicity (*Neuberg et al.*, 2006). The occurrence of this seismicity marks the critical depth where a crucial change in the flow regime exists, from viscous flow below this level to friction controlled slip above it along existing fractures. The shear stress in the conduit cannot exceed the shear strength of the magma, here assumed to be constant at 1 MPa for simplicity, based on experiments on vesicular magma at low confining pressures (*Okumura et al.*, 2010). To accommodate this, the shear stress profile obtained from our flow model is clipped at 1 MPa, which is reached only in the uppermost section of the conduit in all of our models. As low frequency seismicity is only observed at RETU, located at high elevation, this critical source depth is poorly constrained, but probably in the upper section of the conduit (*Bell et al.*, 2018). A full investigation would also take the depth-dependence of the shear strength of the magma into account.

2.2.4 Resulting reference flow model

Figure 2.4 shows how various parameters taken at the conduit centre (a to e) and wall (f and g) vary with depth in the solution of the resulting reference flow model, parameterised as in Table 2.1. The gas volume fraction increases as magma ascends, as volatiles exsolve from the melt. Closer to the surface where gas loss is significant, the gas volume fraction decreases toward zero. The melt and therefore bulk viscosity increase by several orders of magnitude as magma ascends and volatiles exsolve. The bulk density is inversely proportional to the gas volume fraction.

2.2.5 Thermal boundary layer

Temperature gradients can develop in the conduit due to the difference in temperature between the ascending magma and the surrounding edifice. *Collier and Neuberg* (2006) estimated the temperature difference across a 0.3 m thick thermal boundary layer (TBL) at the conduit wall to be 50-200 K (depending on the thermal conductivity of the magma, see Table 2.1) calculated by running a time-dependent model of constant fluid flow including heat loss. Where a TBL with a temperature difference of 200 K is included in our model, we observe that the velocity and therefore strain rate decreases within the TBL. However, this is counteracted by an increase in viscosity to yield a similar shear stress with or without the TBL (Figure 2.5). Therefore, a TBL has been excluded from future model runs. We also discard a vertical temperature gradient in the upper conduit in our model, assuming this, similarly, does not extend far into the conduit and, therefore, does not affect the ascent dynamics.

2.3 Deformation model

To investigate the deformation field at Tungurahua, we build upon the 2D axisymmetric modelling of *Neuberg et al.* (2018) using the Solid Mechanics Module in COMSOL Multiphysics 5.4. The edifice is represented by a homogeneous cone, with the slope angle set to a constant of 26.6° to fix the location of RETU to 1 km vertically and 2 km laterally away from the summit. The base of the slope is 3 km below the summit. Beyond this, the model is extended with a flat surface to a horizontal distance of 100 km from the conduit, and a depth of 100 km from the summit, to avoid numerical boundary effects. A six node triangular mesh is used with an element size of around 50 m across the edifice, extending with distance from the conduit beyond the base of the slope. Roller boundary conditions are applied to exterior lateral model boundaries, such that horizontal displacement is constrained, allowing vertical displacement only. The base of the model is fully constrained in all directions. No constraints are applied to on the upper surface of the model. The depth-dependent shear stress and pressure profiles at the conduit wall, obtained from the flow modelling, are employed along the conduit-edifice boundary to drive the deformation model.

To accurately model the amplitude of the deformation it is imperative to assign realistic values for the mechanical properties (most importantly the Young's modulus) of the volcanic edifice. Volcanic edifices are formed from the deposits of numerous eruptions, effusive and explosive, including lava flows, ignimbrites and ash fall deposits. They are therefore heterogeneous structures, assembled over geologically short time scales of several thousands of years, which makes them inherently unstable (*McGuire*, 1996). It is therefore very difficult to assign a single overall value for the Young's modulus) modulus of a volcanic edifice.

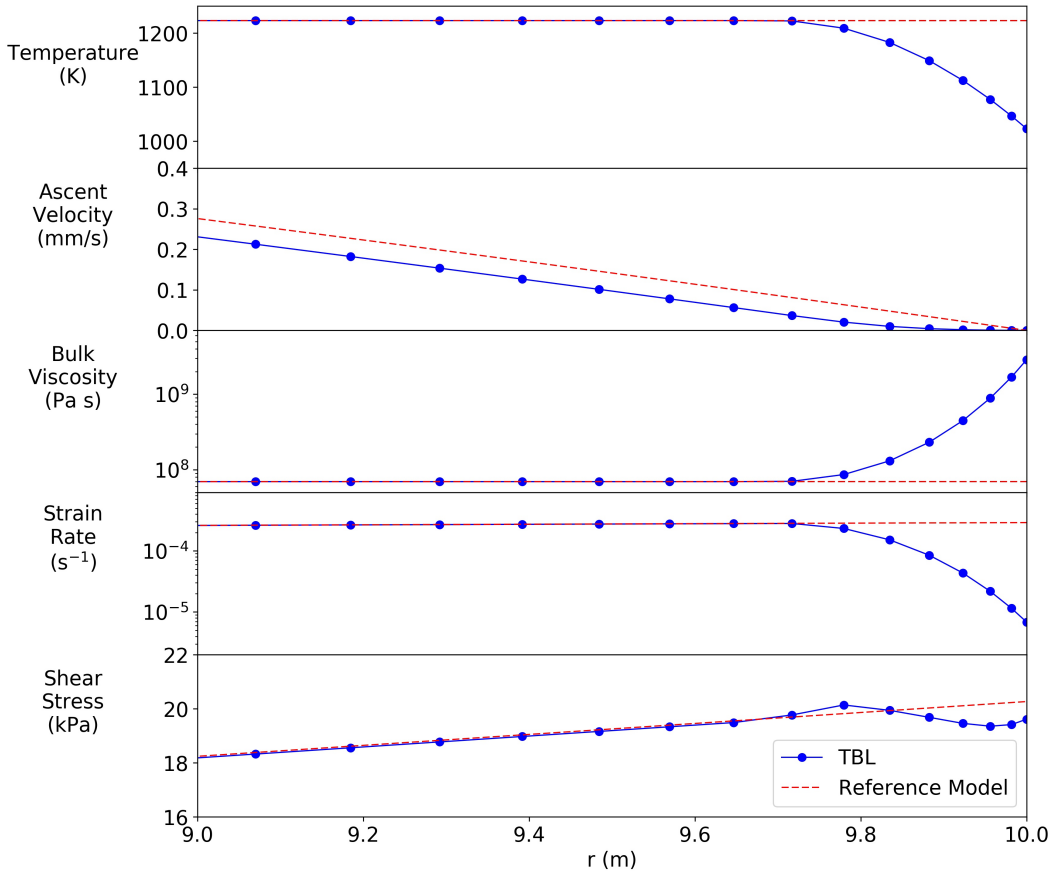

Figure 2.5: Horizontal profiles of (from top to bottom) temperature, ascent velocity, bulk viscosity, strain rate and shear stress at 2000 m in the reference flow model. Zoomed to within one metre of the conduit wall ($9 \leq r \leq 10$). We compare flow models run with (solid) and without (dashed) a TBL of 0.3 m thickness, with a temperature difference of 200 K. Dots show the location of mesh node points. Note that the shear stress at the conduit wall is similar in either case. Instabilities in the strain rate modelled towards the conduit wall arise from the difficulty in modelling such steep changes in melt viscosity with a sufficiently fine mesh size in a FEM.

The Young's modulus of intact rock samples of lava flows is often quoted to be on the order of tens of GPa (e.g. *Heap et al.*, 2010). However, volcanic edifices are exposed to successive fracturing due to stress perturbations, and are therefore intersected by faults and fractures (*Thomas et al.*, 2004), which can drastically reduce the strength of the entire rock mass (e.g. *Heap et al.*, 2014). Cyclic stressing experiments by *Heap et al.* (2010) on intact rock samples of both intrusive and extrusive basalts showed that successive fracturing can reduce the Young's modulus by up to 32 %. Additionally, after deposition, rocks are subject to chemical alteration due to hydrothermal activity and weathering, leading to the formation of primarily clay minerals which are weak in strength (*Pola et al.*, 2014). *Heap et al.* (2014) sampled andesites from Colima volcano, Mexico, and found the Young's modulus to be as low as 6.38 GPa. The Young's modulus is also known to be lower where the rock porosity is higher (*Heap et al.*, 2014).

Unlike intact rock samples, rock masses do not always behave elastically, but deform and fail along fracture surfaces. Instead of the Young's modulus, we use the deformation modulus E_m to quantify how an entire rock mass deforms, similarly defined as the ratio of applied stress to strain exerted, but accounting for elastic and inelastic behaviour (*Hoek and Diederichs*, 2006). The deformation modulus of a volcanic edifice is poorly constrained, in part due to the difficulty in determining E_m in the laboratory, as one needs to test a rock mass volume sufficiently large to be a good representation of the heterogeneity in reality. For this reason, the deformation modulus is generally smaller when a larger sample size is used (*Pinto de Cunha and Muralha*, 1990), and E_m can be orders of magnitude lower than the Young's modulus (e.g. *Hoek and Diederichs*, 2006). *Isik et al.* (2008) attempted to quantify the deformation modulus of heavily jointed and highly weathered andesites underlying northern Ankara, Turkey, and measured a mean value of $E_\mathrm{m} = 34.8$ MPa, with a standard deviation of 25.8 MPa, obtained from pressuremeter tests. Alternatively, E_m can be estimated empirically based on other properties of the rock (e.g. *Hoek and Diederichs*, 2006). However, estimates of E_m obtained through any of the discussed methods are only representative of the area around the test or sample site, whilst deeper in the edifice the weakening effects of temperature and degree of alteration may be considerably higher.

To address this uncertainty, the tilt induced by either shear stress, pressure, or both, has been modelled using a suite of different deformation moduli (Figure 2.6). A Poisson's ratio of 0.25 and edifice density of 2650 kg/m^3 (*Hall et al.*, 1999) are used in each test. Where the deformation modulus E_m is 10 MPa, a tilt at RETU of 67 µrad is modelled using shear stress alone, 24 µrad through pressure alone, and 91 µrad where both sources contribute. Where the deformation modulus is a factor of 10 larger, the tilt modelled is a factor of 10 smaller, as stated by Hooke's law. It has been suggested that conduit pressure is able to explain observed changes in tilt if the conduit is surrounded by a weak zone (*Voight et al.*, 2006); however here we show that regardless of the strength of the edifice, shear stress dominates the tilt at Tungurahua. This is despite

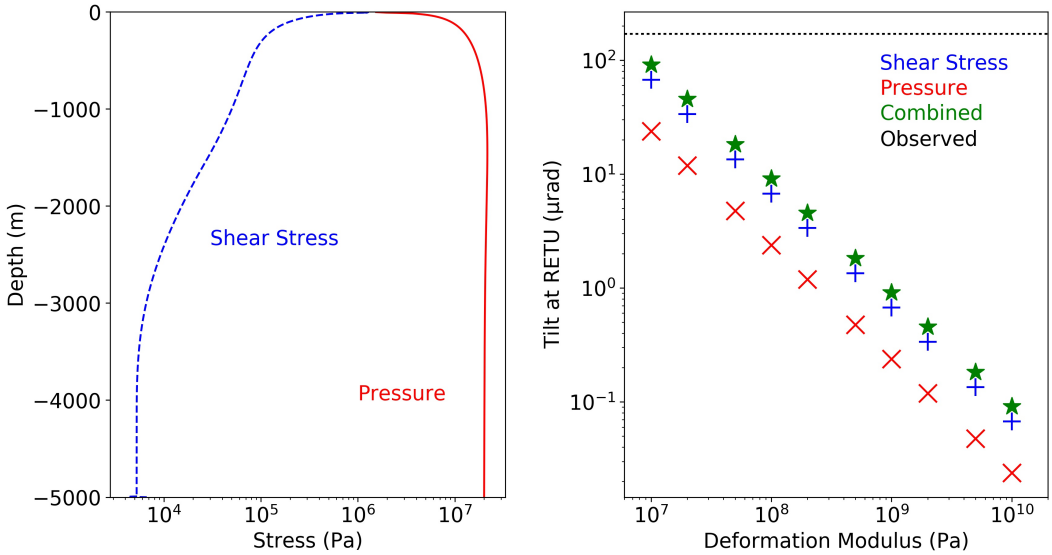

Figure 2.6: Left: Shear stress (blue dashed) and pressure (red solid) profiles obtained from the reference flow model. Note the difference in amplitude between the shear and pressure stresses. Right: Modelled tilt at RETU induced by shear stress (+), pressure (x) or both (star) for a suite of edifice deformation moduli. The tilt modelled due to shear stress is a factor of 2.8 higher than due to pressure, regardless of the deformation modulus used. A deformation modulus of around 10 MPa is required to model 170 μrad of tilt at RETU as observed (black dotted line) (Figure 2.2).

the shear stress obtained from flow modelling being several orders of magnitude smaller than the pressure at most depths.

2.4 Changes in tilt through time

In this section, we investigate how shear stress and conduit pressure change as key factors to the ascent dynamics, such as the volatile content and driving pressure gradient, are varied. At Tungurahua an increase in tilt of around 140 μrad is observed following the first major explosion in the period of interest on July 14th 2013, before decreasing significantly in the days leading up to the three proceeding major explosions (Figure 2.2). We use a constant deformation modulus E_{m} of 10 MPa, required to model the observed amplitude of tilt variations using both shear stress and pressure from the reference flow model (Figure 2.6). In each test we vary only one parameter in our flow model at a time.

Firstly, we consider the July 14th 2013 explosion to be the first event in a sequence. *Hall et al.* (2015) suggested that the cyclic Vulcanian explosions observed between 2013 and 2014 at Tungurahua were the result of pressurisation below tightly sealed viscous plugs. If friction at the conduit wall where this plug has formed is sufficient to impede ascent of magma, the magma ascent velocity and therefore shear stress at the wall would be zero (Eq. 2.1), assuming the magma is behaving as a fluid. Shear stress would still be

exerted only in the uppermost section of the conduit where magma completely solidifies. In a transitional regime, a viscoelastic treatment would be appropriate. As pressure increases below the plug, tilt would increase, but if the contribution of pressure to the tilt is small, this change in tilt would be small, as observed prior to the explosion on July 14th 2013 (Figure 2.2).

Consider that the conduit was vacated following the first eruption, magma would again begin to ascend and fill up the conduit due to the reduction in confining pressure. Pressure and shear stress would be progressively exerted on a greater proportion of the conduit walls, causing tilt to increase through time. This could explain why tilt increases over the weeks following each Vulcanian explosion. Tilt then decreases for several days leading up to the next Vulcanian explosion. *Hall et al.* (2015) suggested that each eruption is preceded by the formation of a viscous plug in the upper conduit. Should this occur, the ascending magma would decelerate, thus causing shear stress to decrease. As shear stress tends to dominate over pressure (Figure 2.7), this may explain why tilt decreases prior to the three latter Vulcanian explosions, despite the pressurisation of the system. As viscosity continues to increase, the magma goes through the ductile-brittle transition zone and fails in a brittle manner, triggering seismicity and causing shear stress to drop further (*Neuberg et al.*, 2018). However, to appropriately model these transient processes, and quantify the resultant changes in tilt, time dependent models that account for disequilibrium in the system must be developed in future work.

Alternative explanations for what has previously triggered major explosions at Tungurahua include the injection of a fresh batch of mafic magma into the magma chamber prior to the paroxysmal events in July and August 2006 (*Samaniego et al.*, 2011), which is potentially volatile rich (*Myers et al.*, 2014, *Andújar et al.*, 2017). This could induce changes in the volatile content of the magma and the pressure at the base of the conduit, which *Thomas and Neuberg* (2014) previously demonstrated can significantly influence ascent dynamics and therefore pressure and shear stress. Here we attempt to quantify how realistic variations in these parameters will influence the tilt.

Figure 2.7a-c shows that the tilt induced by both shear stress and pressure increases linearly as a function of the excess pressure in the conduit, since the ascent velocity and therefore the shear stress are proportional to the driving pressure gradient (Eq. 2.1).

An increase in the initial H_2O content will result in a higher gas volume fraction and a decrease in the bulk magma density. This will facilitate magma ascent through increased buoyancy. Our results suggest that whilst the melt viscosity is lower where the H_2O content is greater, the ascent velocity and therefore shear stress in the upper conduit are both higher. Again, this points to the dominance of ascent rate over viscosity in the trade-off between the two key parameters. Additionally, this leads to an increase in the exsolved volatile content, hence to a higher pressure in the conduit.

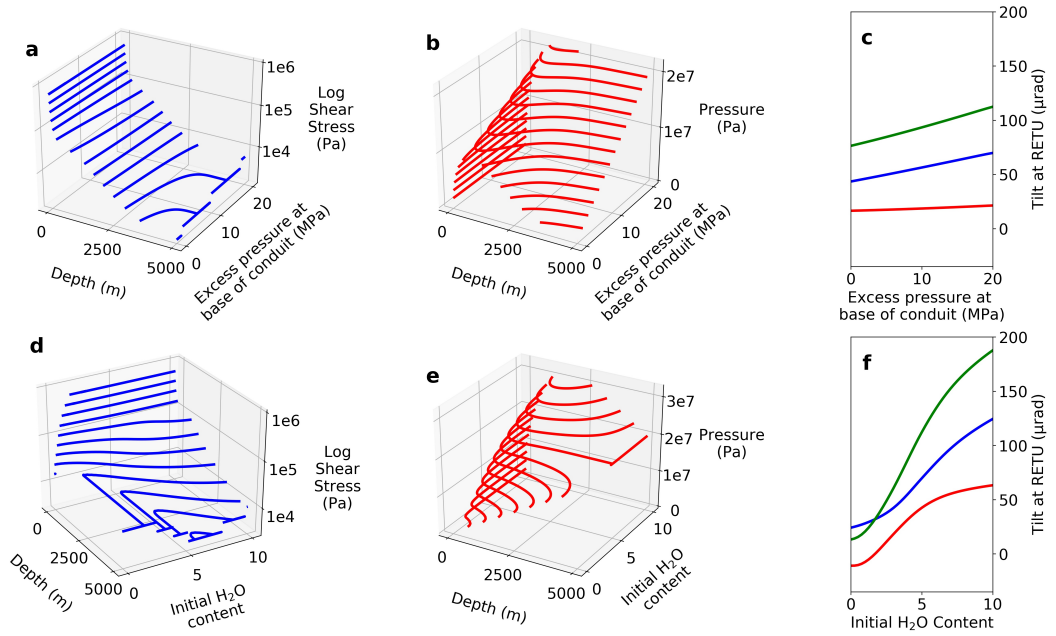

Figure 2.7: Modelled variations in shear stress (left column) and pressure (middle column) with depth from flow modelling and modelled tilt at RETU (right column), each as a function of the excess pressure at the base of the conduit (top row) and the initial H_2O content (bottom row). The combined contribution of shear stress (blue) and pressure (red) to the tilt is plotted in green.

Figure 2.7d-f shows that changing the initial volatile content can significantly influence the shear stress, pressure and resulting tilt, with a maximum combined tilt of 188 μrad for the maximum H_2O content of 10 wt.%. Where the H_2O content is below 1.5 wt.%, a negative radial tilt induced by pressure reduces the combined tilt to only 13 μrad.

We have shown that observed changes in tilt at RETU, in excess of 100 μrad, can be explained by moderate changes in the volatile content or the increase of excess pressure in the conduit. Interestingly, the relative contribution of shear stress and pressure to the combined modelled tilt varies considerably depending on the volatile content. However, the contribution of shear stress to the combined tilt is always greater or equal to the contribution of pressure in all of our models. In some cases, the shear stress and pressure induce opposing and almost counterbalancing tilts. In other cases, the combined tilt is made up almost entirely of the contribution of shear stress. Obviously there is a trade-off between the change in stress required and the deformation modulus of the edifice, to explain observed tilt variations. It is therefore challenging to estimate how much the volatile content or excess pressure did vary through time from the observed tilt variations alone. However, we suggest that with additional information, such as changes in gas flux or the broader deformation pattern, tilt observations can be used to assess how these parameters are varying through time.

2.5 Conclusions

- By quantitatively linking magma ascent to deformation for the first time, we confirm that shear stress exerted on the conduit walls generally dominates over pressurisation as a deformation source of tilt observed close to the conduit. Whilst our model is tuned to Tungurahua volcano, the contribution of both shear stress and pressure should be considered at all silicic volcanoes.

- Previous attempts to link near-field changes in tilt to overpressure or shear stress have used large values for the applied stress. Here, we have used flow modelling to constrain these values. Our results suggest that for tilt variations at RETU to be the result of changes in either shear stress or overpressure in the conduit, the deformation modulus of Tungurahua's edifice must be lower than previously assumed, perhaps on the order of tens of MPa. This suggests that the edifice is either heavily fractured, highly altered, or highly porous, and most likely a combination of the three.

- Realistic variations in the driving pressure gradient and the volatile content are key parameters in driving changes in shear stress, pressure and therefore tilt through time. These variations could be more pronounced due to the non-linear relationships that exist between discharge rate and both crystallisation and gas loss (*Melnik and Sparks*, 1999). Given the large uncertainties in parameters such as crystal content and permeability, we neglect crystallisation during magma ascent and keep the gas loss profile constant. The relative contributions of shear stress and pressure to the tilt vary considerably as a function of the volatile content.

- As magma refills the conduit following a major eruption, shear stress and pressure are progressively exerted on a greater proportion of the conduit wall. Therefore one may expect tilt to increase as this occurs, as observed following Vulcanian explosions at Tungurahua. However, to properly simulate this, or other transient volcanic processes, fully time dependent flow models must be developed, that are able to keep track of changes in the ascent dynamics.

- A decrease in tilt prior to a major explosion can be explained by a decrease in shear stress as ascending magma grinds to a halt below a fixed plug and a pressurisation in the upper conduit. Alternatively, this decrease in tilt could be explained by the onset of seismicity that leads to frictional heating and a subsequent decrease in the magma viscosity. This allows the magma column to accelerate to critical ascent rates without transferring shear stress across the conduit wall. This explanation would require further investigations into the rheology of magma, including frictional heating, and strength recovery of magma. Additionally it is

important to quantify how much shear stress reduction is achieved by a seismic swarm and define the seismicity and tilt rates that point to critical magma ascent.

2.6 Acknowledgements

We would like to thank all the staff at the IGEPN, Ecuador, for their ongoing monitoring operations on Tungurahua, and the OVT staff who keep the monitoring equipment optimally functioning, and *vigías* who provide observations during periods of activity. Luke Marsden was funded by a studentship from the NERC-SPHERES Doctoral Training Partnership (NE/L002574/1). Jürgen Neuberg is partially funded by the Centre for the Observation and Modelling of Earthquakes, Volcanoes and Tectonics (COMET NE/J01978X/1). We acknowledge Amy Collinson for her useful contributions to discussions and for providing help with the modelling. We would like to thank Shigekazu Kusumoto, Oleg Melnik, and Larry Mastin for their constructive reviews.

References

Albino, F., V. Pinel, H. Massol, and M. Collombet (2011), Conditions for detection of ground deformation induced by conduit flow and evolution, *Journal of Geophysical Research: Solid Earth*, *116*(B6).

Andújar, J., C. Martel, M. Pichavant, P. Samaniego, B. Scaillet, and I. Molina (2017), Structure of the Plumbing System at Tungurahua Volcano, Ecuador: Insights from Phase Equilibrium Experiments on July–August 2006 Eruption Products, *Journal of Petrology*, *58*(7), 1249–1278.

Beauducel, F., F.-H. Cornet, E. Suhanto, T. Duquesnoy, and M. Kasser (2000), Constraints on magma flux from displacements data at Merapi volcano, Java, Indonesia, *Journal of Geophysical Research: Solid Earth*, *105*(B4), 8193–8203.

Bell, A. F., M. Naylor, S. Hernandez, I. G. Main, H. Elizabeth Gaunt, P. Mothes, and M. Ruiz (2018), Volcanic eruption forecasts from accelerating rates of drumbeat long-period earthquakes, *Geophysical Research Letters*.

Blake, S. (1990), Viscoplastic models of lava domes, in *Lava flows and domes*, pp. 88–126, Springer.

Burgisser, A., S. Poussineau, L. Arbaret, T. H. Druitt, T. Giachetti, and J.-L. Bourdier (2010), Pre-explosive conduit conditions of the 1997 Vulcanian explosions at Soufrière Hills Volcano, Montserrat: I. Pressure and vesicularity distributions, *Journal of Volcanology and Geothermal Research*, *194*(1), 27–41.

Cluzel, N., D. Laporte, A. Provost, and I. Kannewischer (2008), Kinetics of heterogeneous bubble nucleation in rhyolitic melts: implications for the number density of bubbles in volcanic conduits and for pumice textures, *Contributions to Mineralogy and Petrology*, *156*(6), 745–763.

Collier, L., and J. Neuberg (2006), Incorporating seismic observations into 2D conduit flow modeling, *Journal of Volcanology and Geothermal Research*, *152*(3), 331–346.

Diller, K., A. Clarke, B. Voight, and A. Neri (2006), Mechanisms of conduit plug formation: Implications for vulcanian explosions, *Geophysical Research Letters*, *33*(20).

Dingwell, D. B. (1996), Volcanic dilemma: flow or blow?, *Science*, *273*(5278), 1054.

Engineering Toolbox (2018), Minerals - density, [Online; accessed 21-February-2018].

Faber, T. E. (1995), *Fluid dynamics for physicists*, Cambridge university press.

Gardner, J. E., R. A. Ketcham, and G. Moore (2013), Surface tension of hydrous silicate melts: Constraints on the impact of melt composition, *Journal of Volcanology and Geothermal Research*, *267*, 68–74.

Gaunt, H. E., P. R. Sammonds, P. G. Meredith, R. Smith, and J. S. Pallister (2014), Pathways for degassing during the lava dome eruption of Mount St. Helens 2004–2008, *Geology*, *42*(11), 947–950.

Giordano, D., J. K. Russell, and D. B. Dingwell (2008), Viscosity of magmatic liquids: a model, *Earth and Planetary Science Letters*, *271*(1), 123–134.

Green, D., J. Neuberg, and V. Cayol (2006), Shear stress along the conduit wall as a plausible source of tilt at Soufrière Hills volcano, Montserrat, *Geophysical Research Letters*, *33*(10).

Hall, M. L., C. Robin, B. Beate, P. Mothes, and M. Monzier (1999), Tungurahua Volcano, Ecuador: structure, eruptive history and hazards, *Journal of Volcanology and Geothermal Research*, *91*(1), 1–21.

Hall, M. L., A. L. Steele, B. Bernard, P. A. Mothes, S. X. Vallejo, G. A. Douillet, P. A. Ramón, S. X. Aguaiza, and M. C. Ruiz (2015), Sequential plug formation, disintegration by Vulcanian explosions, and the generation of granular Pyroclastic Density Currents at Tungurahua volcano (2013–2014), Ecuador, *Journal of Volcanology and Geothermal Research*, *306*, 90–103.

Heap, M., D. Faulkner, P. Meredith, and S. Vinciguerra (2010), Elastic moduli evolution and accompanying stress changes with increasing crack damage: implications for stress changes around fault zones and volcanoes during deformation, *Geophysical Journal International*, *183*(1), 225–236.

Heap, M., Y. Lavallée, L. Petrakova, P. Baud, T. Reuschle, N. Varley, and D. B. Dingwell (2014), Microstructural controls on the physical and mechanical properties of edifice-forming andesites at Volcán de Colima, Mexico, *Journal of Geophysical Research: Solid Earth*, *119*(4), 2925–2963.

Hidalgo, S., J. Battaglia, S. Arellano, A. Steele, B. Bernard, J. Bourquin, B. Galle, S. Arrais, and F. Vásconez (2015), SO_2 degassing at Tungurahua volcano (Ecuador) between 2007 and 2013: Transition from continuous to episodic activity, *Journal of Volcanology and Geothermal Research*, *298*, 1–14.

Hoek, E., and M. S. Diederichs (2006), Empirical estimation of rock mass modulus, *International Journal of Rock Mechanics and Mining Sciences*, *43*(2), 203–215.

Hreinsdóttir, S., F. Sigmundsson, M. J. Roberts, H. Björnsson, R. Grapenthin, P. Arason, T. Árnadóttir, J. Hólmjárn, H. Geirsson, R. A. Bennett, et al. (2014), Volcanic plume height correlated with magma-pressure change at Grímsvötn Volcano, Iceland, *Nature geoscience*, *7*(3), 214.

Isik, N. S., V. Doyuran, and R. Ulusay (2008), Assessment of deformation modulus of weak rock masses from pressuremeter tests and seismic surveys, *Bulletin of Engineering Geology and the Environment*, *67*(3), 293–304.

Johnson, J. H., M. P. Poland, K. R. Anderson, and J. Biggs (2019), A cautionary tale of topography and tilt from Kīlauea Caldera, *Geophysical Research Letters*, *46*(8), 4221–4229.

Klug, C., and K. V. Cashman (1996), Permeability development in vesiculating magmas: implications for fragmentation, *Bulletin of Volcanology*, *58*(2-3), 87–100.

Laumonier, M., L. Arbaret, A. Burgisser, and R. Champallier (2011), Porosity redistribution enhanced by strain localization in crystal-rich magmas, *Geology*, *39*(8), 715–718.

Lensky, N., V. Lyakhovsky, and O. Navon (2002), Expansion dynamics of volatile-supersaturated liquids and bulk viscosity of bubbly magmas, *Journal of fluid mechanics*, *460*, 39–56.

Llewellin, E., and M. Manga (2005), Bubble suspension rheology and implications for conduit flow, *Journal of Volcanology and Geothermal Research*, *143*(1), 205–217.

Mader, H., E. Llewellin, and S. Mueller (2013), The rheology of two-phase magmas: A review and analysis, *Journal of Volcanology and Geothermal Research*, *257*, 135–158.

Maron, S. H., and P. E. Pierce (1956), Application of Ree-Eyring generalized flow theory to suspensions of spherical particles, *Journal of colloid science*, *11*(1), 80–95.

McGuire, W. (1996), Volcano instability: a review of contemporary themes, *Geological Society, London, Special Publications*, *110*(1), 1–23.

Melnik, O., and R. Sparks (1999), Nonlinear dynamics of lava dome extrusion, *Nature*, *402*(6757), 37.

Melnik, O., and R. Sparks (2005), Controls on conduit magma flow dynamics during lava dome building eruptions, *Journal of Geophysical Research: Solid Earth*, *110*(B2).

Molina, I., H. Kumagai, J.-L. Le Pennec, and M. Hall (2005), Three-dimensional P-wave velocity structure of Tungurahua Volcano, Ecuador, *Journal of volcanology and geothermal research*, *147*(1), 144–156.

Mothes, P. A., H. A. Yepes, M. L. Hall, P. A. Ramón, A. L. Steele, and M. C. Ruiz (2015), The scientific–community interface over the fifteen-year eruptive episode of Tungurahua Volcano, Ecuador, *Journal of Applied Volcanology*, *4*(1), 9.

Mueller, S., E. Llewellin, and H. Mader (2011), The effect of particle shape on suspension viscosity and implications for magmatic flows, *Geophysical Research Letters*, *38*(13).

Myers, M. L., D. J. Geist, M. C. Rowe, K. S. Harpp, P. J. Wallace, and J. Dufek (2014), Replenishment of volatile-rich mafic magma into a degassed chamber drives mixing and eruption of Tungurahua volcano, *Bulletin of Volcanology*, *76*(11), 872.

Neuberg, J., H. Tuffen, L. Collier, D. Green, T. Powell, and D. Dingwell (2006), The trigger mechanism of low-frequency earthquakes on Montserrat, *Journal of Volcanology and Geothermal Research*, *153*(1), 37–50.

Neuberg, J. W., A. S. Collinson, P. A. Mothes, M. C. Ruiz, and S. Aguaiza (2018), Understanding cyclic seismicity and ground deformation patterns at volcanoes: Intriguing lessons from Tungurahua volcano, Ecuador, *Earth and Planetary Science Letters*, *482*, 193–200.

Okumura, S., and T. Kozono (2017), Silicic lava effusion controlled by the transition from viscous magma flow to friction controlled flow, *Geophysical Research Letters*, *44*(8), 3608–3614.

Okumura, S., M. Nakamura, T. Nakano, K. Uesugi, and A. Tsuchiyama (2010), Shear deformation experiments on vesicular rhyolite: Implications for brittle fracturing, degassing, and compaction of magmas in volcanic conduits, *Journal of Geophysical Research: Solid Earth*, *115*(B6).

Pinto de Cunha, A., and J. Muralha (1990), About LNEC experience on scale effects in the deformability of rock masses, in *Int workshop on scale effects in rock masses, Loen. Ed. Balkema, 219*, vol. 229.

Pola, A., G. B. Crosta, N. Fusi, and R. Castellanza (2014), General characterization of the mechanical behaviour of different volcanic rocks with respect to alteration, *Engineering Geology*, *169*, 1–13.

Romero, J. E., G. A. Douillet, S. V. Vargas, J. Bustillos, L. Troncoso, J. D. Alvarado, and P. Ramón (2017), Dynamics and style transition of a moderate, Vulcanian-driven eruption at Tungurahua (Ecuador) in February 2014: pyroclastic deposits and hazard considerations, *Solid Earth*, *8*(3), 697.

Ruiz, M. C., J. M. Lees, and J. B. Johnson (2006), Source constraints of Tungurahua volcano explosion events, *Bulletin of volcanology*, *68*(5), 480–490.

Rust, A., and M. Manga (2002), Effects of bubble deformation on the viscosity of dilute suspensions, *Journal of non-newtonian fluid mechanics*, *104*(1), 53–63.

Samaniego, P., J.-L. Le Pennec, C. Robin, and S. Hidalgo (2011), Petrological analysis of the pre-eruptive magmatic process prior to the 2006 explosive eruptions at Tungurahua volcano (Ecuador), *Journal of Volcanology and Geothermal Research*, *199*(1), 69–84.

Sparks, R. S. J. (1997), Causes and consequences of pressurisation in lava dome eruptions, *Earth and Planetary Science Letters*, *150*(3-4), 177–189.

Spera, F. J. (2000), Physical properties of magma, *Encyclopedia of volcanoes*, *176*.

Thomas, M. E., and J. Neuberg (2012), What makes a volcano tick-A first explanation of deep multiple seismic sources in ascending magma, *Geology*, *40*(4), 351–354.

Thomas, M. E., and J. W. Neuberg (2014), Understanding which parameters control shallow ascent of silicic effusive magma, *Geochemistry, Geophysics, Geosystems*, *15*(11), 4481–4506.

Thomas, M. E., N. Petford, and E. N. Bromhead (2004), Volcanic rock-mass properties from Snowdonia and Tenerife: implications for volcano edifice strength, *Journal of the Geological Society*, *161*(6), 939–946.

Truby, J., S. Mueller, E. Llewellin, and H. Mader (2015), The rheology of three-phase suspensions at low bubble capillary number, in *Proc. R. Soc. A*, vol. 471, p. 20140557, The Royal Society.

Tsvetkova, Y. D., and O. Melnik (2018), The influence of non-newtonian properties of magma on flow in a volcanic conduit, in *Doklady Physics*, vol. 63, pp. 485–488, Springer.

Voight, B., R. Sparks, A. Miller, R. Stewart, R. Hoblitt, A. Clarke, J. Ewart, W. Aspinall, B. Baptie, E. Calder, et al. (1999), Magma flow instability and cyclic activity

at Soufrière Hills Volcano, Montserrat, British West Indies, *Science*, *283*(5405), 1138–1142.

Voight, B., A. Linde, I. Sacks, G. Mattioli, R. Sparks, D. Elsworth, D. Hidayat, P. Malin, E. Shalev, C. Widiwijayanti, et al. (2006), Unprecedented pressure increase in deep magma reservoir triggered by lava-dome collapse, *Geophysical Research Letters*, *33*(3).

Zhang, Y., Z. Xu, M. Zhu, and H. Wang (2007), Silicate melt properties and volcanic eruptions, *Reviews of Geophysics*, *45*(4).

Chapter 3

Topography and tilt at volcanoes

L. Marsden[1], J. Neuberg[1], M. Thomas[1]

[1] *School of Earth and Environment, University of Leeds, Leeds, United Kingdom*

Citation: **Marsden, L. H.**, Neuberg, J., Thomas, M. (2019). *Topography and tilt at volcanoes*. Frontiers in Earth Science 7, 317

Abstract

For optimal monitoring of the deformation of a volcano, instrumentation should be deployed at the location most sensitive to changes at the suspected deformation source. The topographic effect on tilt depends strongly on the orientation of the deformation field relative to the surface on which the instrument is deployed. This fact has long been understood and corrected for in tilt measurements related to body tides and referred to as "cavity" or "topographic effects" (*Harrison*, 1976). Despite this, and whilst topography at volcanoes is often significant, until now the topographic effect on tilt at volcanoes has not been systematically explored. Here, we investigate the topographic effect on tilt produced by either the pressurisation of a reservoir or conduit, or shear stress as magma ascends through a conduit, using 2D axisymmetric and 3D finite element deformation modelling. We show that topography alone can amplify or reduce the tilt by more than an order of magnitude, and control the orientation of the maximum tilt. Therefore, a decrease in tilt can even be caused by an increase in deformation at the source. Hence, inverting for the source stress using simple analytical models that neglect topography could potentially lead to a misinterpretation of how the volcanic system is evolving. Since topographic features can amplify the tilt signal, they can be exploited when deciding upon an installation site.

3.1 Introduction

Deformation at volcanoes can be generated by a number of different sources. Broad centimetre to metre-scale uplift and subsidence over periods of months to years can be indicative of inflation and deflation of a magma reservoir at depth (*Mogi*, 1958). Close to the conduit, cyclic variations in tilt have been linked to shear stress exerted on the conduit wall as magma ascends (*Beauducel et al.*, 2000, *Neuberg et al.*, 2018, *Marsden et al.*, 2019). Near-field deformation has also been linked to a pressure source in the upper edifice (*Voight et al.*, 1999, *Hautmann et al.*, 2009, *Widiwijayanti et al.*, 2005). Inversion and forward modelling can be performed to estimate the source geometry and the amplitude of the stress responsible for the observed deformation, taking key factors such as viscoelasticity (*Del Negro et al.*, 2009, *Newman et al.*, 2006), topography (*Cayol and Cornet*, 1998, *McTigue and Segall*, 1988, *Ronchin et al.*, 2015), and mechanical heterogeneity (*Trasatti et al.*, 2003, *Hautmann et al.*, 2010, *Hickey and Gottsmann*, 2014) into account.

Tiltmeters are commonly deployed at volcanoes to measure deformation, and are typically sensitive to a precision of at least 1 µrad, equivalent to an uplift of 1 mm over a horizontal distance of 1 km. Due to this precision, tilt is highly sensitive to small changes in the stress field, as observed in the local vicinity of topographic features such as valleys, cliffs and ridges. *Harrison* (1976) showed that tilt caused by earth tides can

be significantly higher on the slopes of a valley than on a flat surface. However, how topography affects tilt is dependent on the orientation of the deformation field relative to the surface on which the instrument is deployed. Volcanoes often have considerable relief and complex topography. Hence, we systematically explore the effect of volcanic topography on the monitored tilt signal.

We investigate how tilt induced by either shear stress, conduit or reservoir pressure is influenced by topography, using the finite element numerical modelling software COMSOL Multiphysics v5.4. We show that topography alone can amplify, reduce, or even reverse the polarity of the tilt signal. Firstly, in Section 3.2 we show analytically that tilt is dependent on the original slope angle. In Section 3.3, we present results of 2D axisymmetric modelling to investigate the influence that the relief of the edifice has on tilt by varying the elevation of volcanic topography defined by a simple Gaussian function. We then, in Section 3.4, show how the local topography affects the tilt by introducing changes in slope into our models. Finally, in Section 3.5, we assess how tilt varies spatially across real topography by incorporating 10 × 10 m digital elevation models of Tungurahua volcano, Ecuador, and Soufrière Hills volcano, Montserrat (SHV) into 3D models. We also show how topography can be exploited to enhance the signal amplitude.

In each of the following sections, we consider the following three axisymmetric deformation sources:

- Reservoir pressure: A spherical reservoir centred directly below the summit at a depth of 8 km below the mean elevation, with a radius of 500 m and a pressure of 20 MPa.
- Conduit shear stress: Reference depth-variant shear stress profile from *Marsden et al.* (2019), derived through flow modelling, extending from the surface to a depth of 5 km.
- Conduit pressure: Depth-variant over-pressure profile from the same model in *Marsden et al.* (2019), similarly extending from the surface to a depth of 5 km.

In section 5, we also discuss the topographic effect on tilt produced by 3D deformation sources, where the orientation of the maximum tilt is not radial from the source even in the absence of topography.

3.2 Influence of the original slope angle

Tilt is dependent on both the source stress and the orientation of the displacement field relative to the surface where tilt is measured. Consider a purely vertical displacement field along a simple slope, where the amount of displacement decreases linearly from w

to 0 at distance x (Figure 3.1A). The change in slope, or tilt, $\Delta\theta$, is a function of the original slope angle θ,

$$\tan(\theta + \Delta\theta) = \frac{w + z}{x} \tag{3.1}$$

$$\tan(\theta + \Delta\theta) = \frac{w}{x} + \tan\theta \tag{3.2}$$

$$\Delta\theta = \arctan\left(\frac{w}{x} + \tan\theta\right) - \theta \tag{3.3}$$

where $z = x\tan\theta$. By solving Equation 3.3 for a suite of slope angles θ, holding w and x constant, we show that the tilt $\Delta\theta$ is greatest where the original slope is horizontal, and no tilt is generated where the slope is vertical (Figure 3.1A). Results are normalised by the maximum tilt, $\Delta\theta_{\max}$.

Similarly, we can consider a purely horizontal displacement field where the amount of displacement decreases linearly from u to 0 at distance x (Figure 3.1B).

$$\tan(\theta + \Delta\theta) = \frac{z}{x - u} \tag{3.4}$$

$$\tan(\theta + \Delta\theta) = \frac{x\tan\theta}{x - u} \tag{3.5}$$

$$\Delta\theta = \arctan\left(\frac{x\tan(\theta)}{x - u}\right) - \theta \tag{3.6}$$

Holding u and x constant, Equation 3.6 shows that no tilt is produced where the ground is horizontal or vertical, and the highest tilt, $\Delta\theta/\Delta\theta_{\max}$, is produced where the slope is at 45° (Figure 3.1B).

Inflation or deflation of a magma reservoir is commonly modelled analytically using a point source (*Mogi*, 1958), where the orientation of the displacement field at the surface varies with horizontal distance from the source. The point source approximation is valid for a spherical source where the source radius is small with respect to the distance from that source. Addressing the influence of topography, *Cayol and Cornet* (1998) showed that displacement produced by reservoir pressure is greater at lower elevation, where the surface is closer to the source. Delving further, *Ronchin et al.* (2015) found that the slope angle θ is a secondary control on the displacement. Through numerical modelling, they showed that the maximum displacement is produced where the surface is perpendicular to a line between the surface and source, where the *exposure* to the pressure source is greatest. We refer to the slope angle with the maximum exposure to the source at any point as θ_{maxexp}, and the deviation from this angle as $\theta - \theta_{\text{maxexp}}$. Hence, tilt generated by a point or spherical source is influenced by the slope angle. We vary this over a 90° range around a point centred at $x = 3\,\text{km}$, $z = 3\,\text{km}$

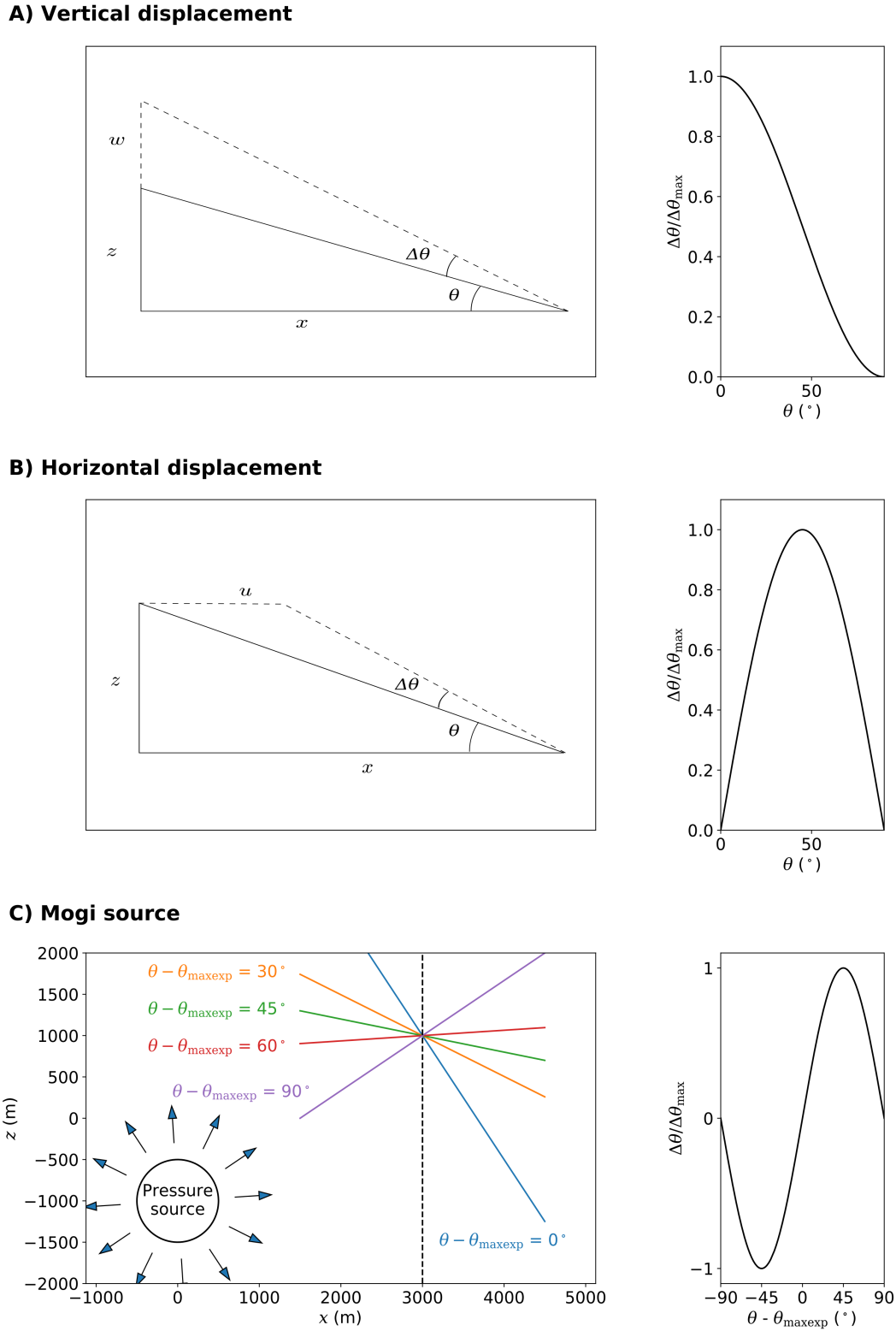

Figure 3.1: Tilt produced by purely vertical (A) or horizontal (B) displacement that decreases linearly with distance from the conduit, as a function of the original angle of the slope θ. (C): Tilt induced by a spherical source, as a function of slope angle, where $\theta - \theta_{\text{maxexp}} = 0$ when the slope is perpendicular to the displacement field.

(Figure 3.1C). We calculate u and w at each point along the slope using it's distance from the centre of a Mogi source ($x = 0\,\text{km}$, $z = -1\,\text{km}$)

$$\begin{bmatrix} u \\ v \\ w \end{bmatrix} = \alpha^3 \Delta P \frac{1-\nu}{E_\text{m}} \begin{bmatrix} x/R^3 \\ y/R^3 \\ d/R^3 \end{bmatrix}, \tag{3.7}$$

where ΔP is the change in pressure, α is the source radius, d is the vertical distance between each point and the source centre, ν is the Poisson's ratio and E is the Young's modulus. v is the displacement in the y direction, which is not used in this 2D example, but is considered in the 3D modelling later in Section 3.5. The new slope angle can be computed as the derivative of the new coordinates for each point along the slope, $x+u$ and $z+w$. The tilt $\Delta\theta$ is then calculated as the change in slope angle. We find that the tilt $\Delta\theta/\Delta\theta_\text{max}$ is greatest where the surface is 45° from the angle of maximum exposure, i.e. where $\theta - \theta_\text{maxexp} = 45°$ (Figure 3.1C). In other words, no tilt is produced where the surface is parallel or perpendicular to the displacement field, and the highest tilt is generated where the surface is 45° from this. This, unsurprisingly, is as previously shown for a purely horizontal displacement field.

3.3 Relief of the edifice

The surface directly above a point source in an elastic half-space is pushed vertically upwards as pressure increases, as the surface is perpendicular to the displacement field. Moving horizontally away from this point, the surface rotates outwards, away from the source, which we define as a positive radial tilt. *McTigue and Segall* (1988) showed that where the relief of the edifice is considerable, such that the surface vertically above the source is further from the source than a point down slope, the surface rotates inwards, hence a negative radial tilt is produced. In this case, the amplitude of displacement is greater at a point down slope than directly above the source. Whilst this relationship has been examined for a point source, the topographic effect on tilt produced by conduit pressure or shear stress has not been investigated. Here, we perform 2D axisymmetric deformation modelling using COMSOL Multiphysics v5.4 to investigate how edifice relief influences the tilt produced by conduit pressure and shear stress. We include a volcanic edifice, where the elevation z is defined using a Gaussian function

$$z = z_\text{max} e^{-\left(\frac{x^2}{2 \times 2500^2}\right)}, \tag{3.8}$$

where x is the horizontal distance from the source, and the maximum relief z_max is varied between 0-3 km. Roller boundary conditions that allow vertical motion only are applied to the lateral model boundaries. The base of the model is fixed in all

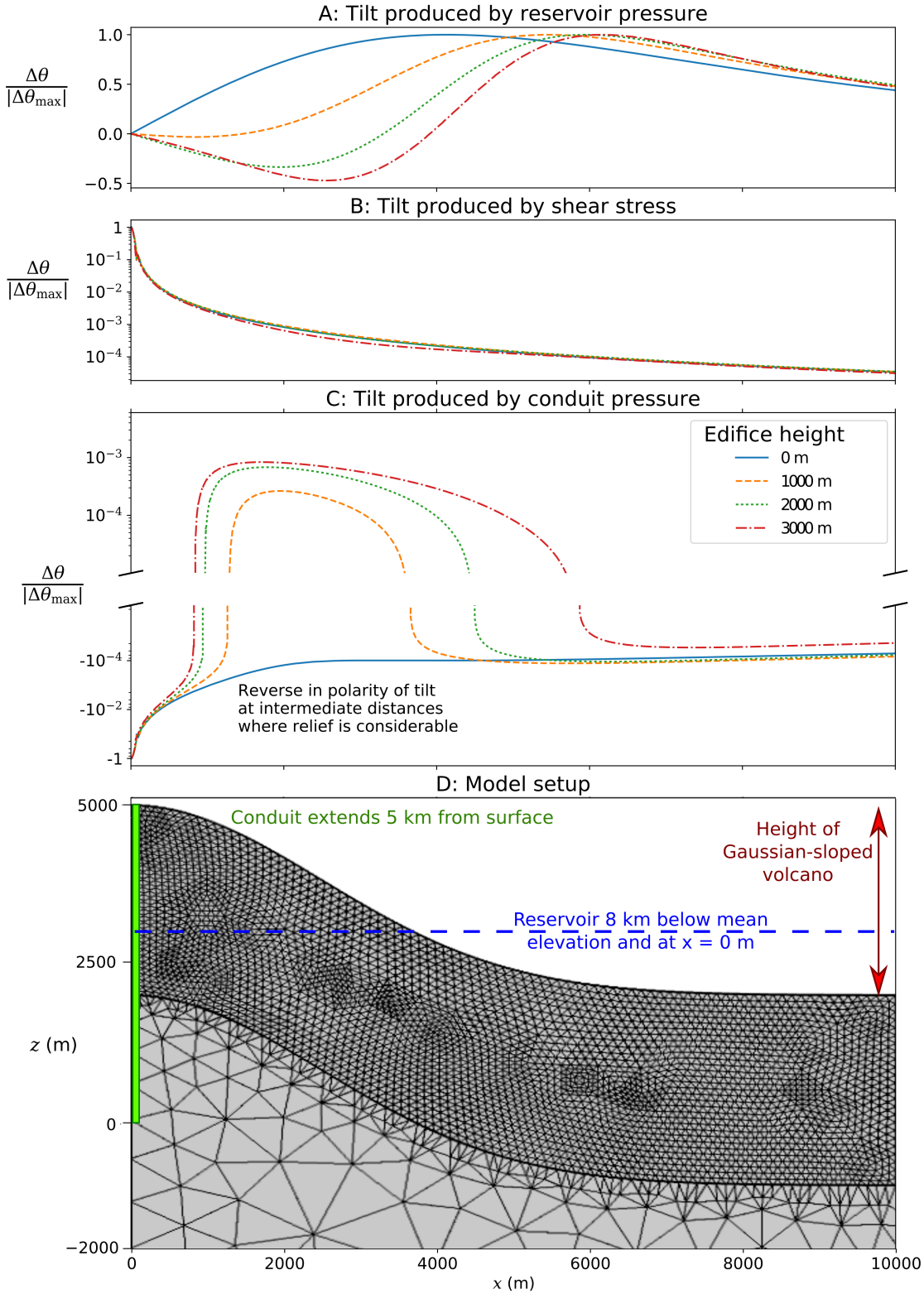

Figure 3.2: Modelled tilt $\Delta\theta$ produced by A) reservoir pressure, B) shear stress or C) conduit pressure, each as a function of horizontal distance from the conduit x. The height of the volcano is varied. D) Model setup. A high resolution mesh is used to a depth of 3 km below the surface, to a horizontal distance of 10 km, with a minimum element size of around 30 m

directions. The model is extended to a radius of 40 km and a depth of 50 km to avoid numerical effects from these boundary conditions. The surface may deform freely. A spatially-variant triangular mesh is used, that allows complex geometries to be suitably meshed easily. A finer mesh is used in the upper 3 km below the surface to a horizontal distance of 10 km, where the modelled solution is examined, and thus a higher degree of accuracy is required (Figure 3.2D). A minimum element size of around 30 m is used within this region. A sensitivity analysis was necessary to ensure that a sufficiently fine mesh was used, until the solution was consistent if the mesh was refined further. The Young's modulus and Poisson's ratio of the medium are set at 1 GPa and 0.25 respectively. The numerical models were benchmarked against the analytical solution for a Mogi source.

For both a shear stress or a conduit pressure source, the strongest tilt signal can be seen close to the conduit while it decreases with increasing distance (Figure 3.2). The influence of the relief on tilt produced by shear stress appears to be minimal, and the resulting tilt is always positive, irrespective of the relief. In the absence of relief, a negative radial tilt is induced by conduit pressure at all locations, because the component of displacement perpendicular to the surface (vertical in this case) decreases with increasing distance from the conduit (Figure 3.3a). Hence, the surface rotates inwards towards the conduit. However, where the relief is considerable, such that the component of the displacement pushing the surface perpendicularly outwards decreases with increasing distance from the conduit (Figure 3.3d), a positive radial tilt is modelled at intermediate distances from the conduit. Here, one must consider how both the total displacement, and the alignment of the displacement field with the surface, vary with distance from the conduit.

3.4 Local topography

To investigate the effect of local topography on tilt, we introduce breaks in slope into our model (Figure 3.4). A tapering feature was used to avoid sharp edges at the breaks in slope. We include one slope facing away from the centre of the model, hereon referred to as the proximal slope. This is opposed by a slope facing towards the centre of the model, hereon referred to as the distal slope. The opposing slopes each dip at 60° from horizontal and are separated by a horizontal distance of 100 m. With this pair of opposing slopes, we attempt to represent topographic features such as cliffs and valleys. We focus on this morphology, as *Johnson et al.* (2019) have shown that anomalous tilt measurements can be produced in close proximity to the cliffs of a caldera rim. The resolution of the triangular mesh is increased in the close vicinity of each break in slope, to a minimum element size of around 20 cm. The location of these opposing slopes is varied.

Since the topographic effect on tilt is predominantly limited to the extent of the

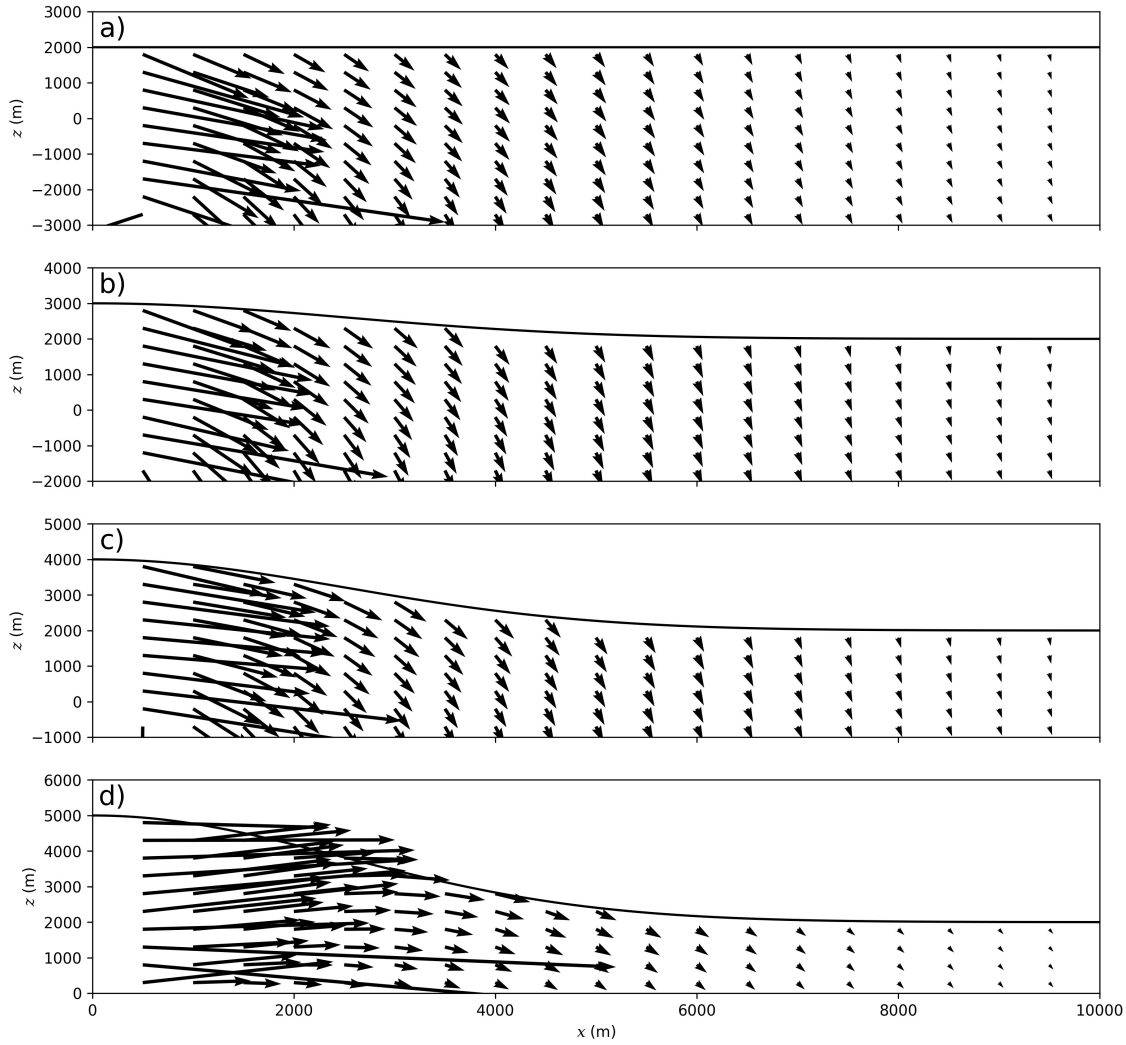

Figure 3.3: Deformation field produced by overpressure of the conduit for a suite of values for the edifice relief. In each case the pressure source extends from the surface to 5 km below. The arrows depict the amplitude and orientation of the displacement field at each point.

topographic feature (*Harrison*, 1976), the topographic effect of each break in slope can be considered in isolation. Thus, the topographic effect of a range of features can be inferred based on our models, such as cliffs, ridges and valleys. Whilst *Harrison* (1976) investigated how tilt induced by earth tides is affected by the inclusion of a cavity or valley, the topographic effect on tilt generated by volcanic sources may be considerably different, due to 1) differences in the orientation of the deformation field with respect to the surface, and 2) the spatial extent of deformation is much smaller for shallow volcanic sources than generated by earth tides, and can be similar to the scale of typical topographic features found at volcanoes (Figure 3.2).

To isolate the topographic effect on tilt, in each case the radial tilt $\Delta\theta$ is divided by the 'reference' tilt, $\Delta\theta_{\mathrm{r}}$, modelled for relief defined by a Gaussian function or flat surface, at the same x coordinate, in the absence of local topography. We introduce

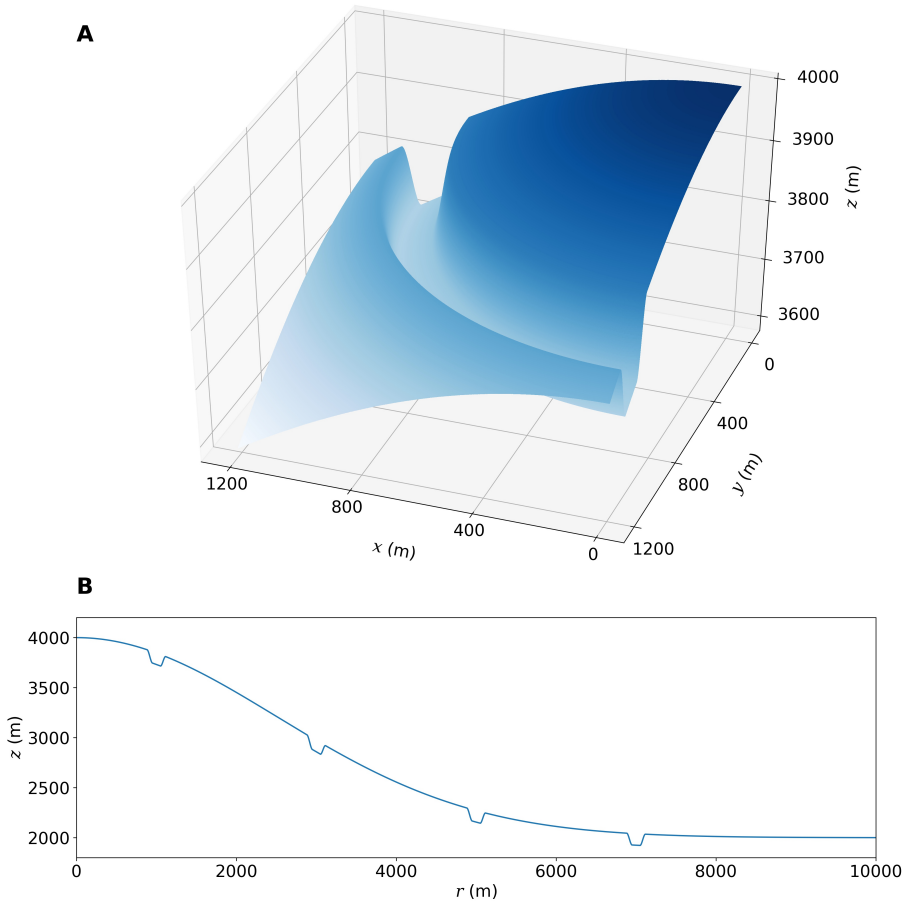

Figure 3.4: Two opposing slopes introduced onto the edifice defined by Eq. 3.8, in A) 3D and B) 2D axisymmetric space.

the following parameters that are used in the following sections:

- $\Delta\theta_{\mathrm{AMP}} = \Delta\theta/\Delta\theta_{\mathrm{r}}$ is the factor by which topography has amplified or reduced tilt. In the absence of local topography, $\Delta\theta_{\mathrm{AMP}} = 1$.
- $\Delta\theta_{\mathrm{DIFF}} = (\Delta\theta - \Delta\theta_{\mathrm{r}})/|\Delta\theta_{\mathrm{r}}|$ is the difference in tilt due to topography. In the absence of local topography $\Delta\theta_{\mathrm{DIFF}} = 0$. Where $\Delta\theta_{\mathrm{DIFF}}$ is positive, the radial tilt is higher due to the presence of the local topography. Note that $\Delta\theta$ and $\Delta\theta_{\mathrm{r}}$ could still be either positive or negative depending on the direction of the slope rotation.

By plotting how these parameters vary across the topography, as opposed to the tilt $\Delta\theta$, our results are not masked by the decrease in tilt with distance from the source. Also, the absolute amplitude of the tilt $\Delta\theta$ is strongly dependent on the mechanical properties of the edifice, which are often poorly constrained. However, $\Delta\theta_{\mathrm{AMP}}$ and $\Delta\theta_{\mathrm{DIFF}}$ are not, and so they can be used to quantify the topographic effect on tilt irrespective of these mechanical properties.

3.4.1 Reservoir pressure

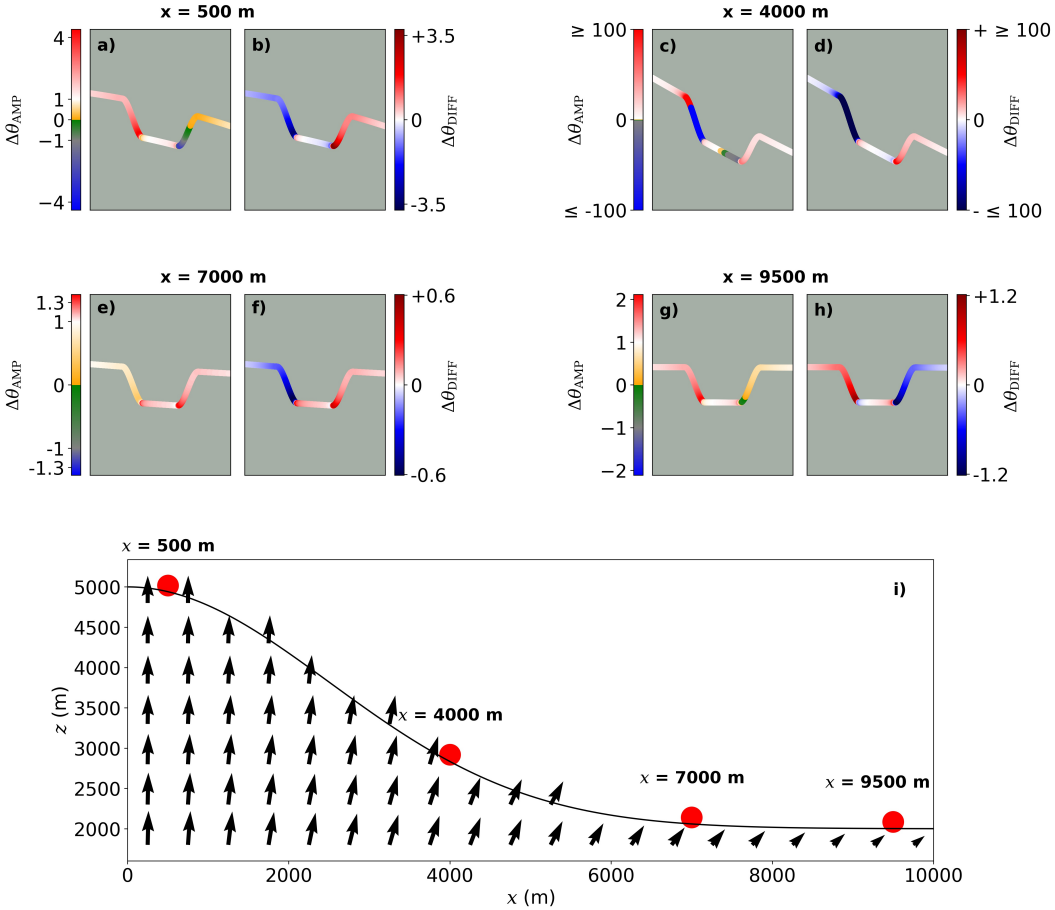

Figure 3.5: **a-h**: Amplification factor and difference due to the topographic effect on tilt generated by reservoir pressure, where opposing slopes are included at either $x = 500\,\text{m}$, 4000 m, 7000 m or 9500 m, as indicated by red dots. **i**: Amplitude and orientation of the displacement field produced by reservoir pressure.

Here, we investigate the topographic effect on tilt produced by the pressurisation of a magma reservoir, for opposing slopes centred at either $x = 0.5\,\text{km}$, 4 km, 7 km or 9.5 km (Figure 3.5). For a spherical pressure source, the total displacement decreases with increasing distance from the source. For an edifice with a relief of 3 km as shown here, the summit is not the closest point to the source. How tilt varies across the slopes depends on the relative amount of vertical and horizontal displacement, w and u respectively. The vertical component of displacement, w, is greater at the base of each slope than at the top, hence the height of each slope reduces. Each slope must become shallower to accommodate this. Competing against this, since the horizontal component u is greater on the proximal slope than the distal slope, the opposing slopes are pushed closer together and steepen. For opposing slopes introduced at $x < 7\,\text{km}$, where $u < w$, the radial tilt is reduced on the proximal slope ($\Delta\theta_{\text{DIFF}} < 0$) and increased on the distal slope ($\Delta\theta_{\text{DIFF}} > 0$, Figure 3.5b,d). For opposing slopes centred at $x =$

0.5 km, where the displacement field is predominantly vertical, the polarity of the radial tilt is reversed towards the base of the distal slope due to topography ($\Delta\theta_{\mathrm{AMP}} < 0$, Figure 3.5a). Here, $\Delta\theta_{\mathrm{r}}$ is negative (Figure 3.2A). However, if the relief of the edifice is less pronounced, $\Delta\theta_{\mathrm{r}}$ would be positive, and thus $\Delta\theta_{\mathrm{AMP}}$ would be negative on the proximal slope. For opposing slopes introduced at $x > 7$ km, whilst each slope tilts away from the source, the radial tilt is increased on the proximal slope ($\Delta\theta_{\mathrm{DIFF}} > 0$) and reduced on the distal slope due to topography ($\Delta\theta_{\mathrm{DIFF}} < 0$, Figure 3.5h). For opposing slopes introduced at $x = 7$ km, $\Delta\theta_{\mathrm{AMP}}$ is close to one at most points, meaning that the topographic effect on tilt is in this case small (Figure 3.5e). This topographic effect on tilt is, however, more pronounced in close proximity of the base of each slope.

Irrespective of the location of the opposing slopes, the effect on tilt is greatest close to the base of each slope ($|\Delta\theta_{\mathrm{AMP}}|$ is high, (Figure 3.5a,c,e,g)). The highest values of $|\Delta\theta_{\mathrm{AMP}}|$ are obtained with the opposing slopes centred at $x = 4$ km (Figure 3.5c). Here, the reference tilt, $\Delta\theta_{\mathrm{r}}$, is close to zero (Figure 3.2A) and is insensitive to changes in the reservoir pressure. Interestingly however, the surface of the edifice at this point is close to perpendicular to the displacement field. Consequently, the amount by which the base and top of each slope move closer together is relatively large here, and the tilt is amplified significantly on the slopes. This suggests that for two points in close proximity at the same elevation and distance from the source, a relatively high tilt can be produced at one, and no tilt at the other, with the local topography being the only difference.

3.4.2 Conduit shear stress

Shear stress produces a predominantly vertical displacement field, but the ratio u/w increases with distance from the conduit (Figure 3.6f). Opposing slopes introduced at any location will each rotate away from the conduit as a result of shear stress (i.e. $\Delta\theta$ is positive). Whilst in our models the tilt $\Delta\theta$ is always higher on the proximal slope than the distal, due to tilt decreasing significantly with increasing distance from the conduit (Figure 3.2B), the topographic effect on the tilt varies between the opposing slopes, and depends on the location of the topographic feature. Here we show that this depends on whether the slopes are located in a predominantly extensional (where du/dx is positive) or compressional (where du/dx is negative) regime horizontally. We present results for an edifice with a relief of 2 km (Figure 3.6f), such that opposing slopes at $x = 2.5$ km are situated in an extensional regime, whilst opposing slopes at 9 km are situated in a compressional regime (Figure 3.6g). The distance between opposing slopes at $x = 2.5$ km increases due to extension, and so the modelled tilt is reduced $\Delta\theta_{\mathrm{AMP}} < 1$ on the proximal slope, and amplified on the distal slope $\Delta\theta_{\mathrm{AMP}} > 1$ (Figure 3.6a). Contrary to this, the distance between opposing slopes centred at $x = 9$ km decreases due to compression, so the modelled tilt is amplified $\Delta\theta_{\mathrm{AMP}} > 1$ on the proximal slope, and reduced towards the base of the distal slope $\Delta\theta_{\mathrm{AMP}} < 1$ (Figure 3.6c). In both cases,

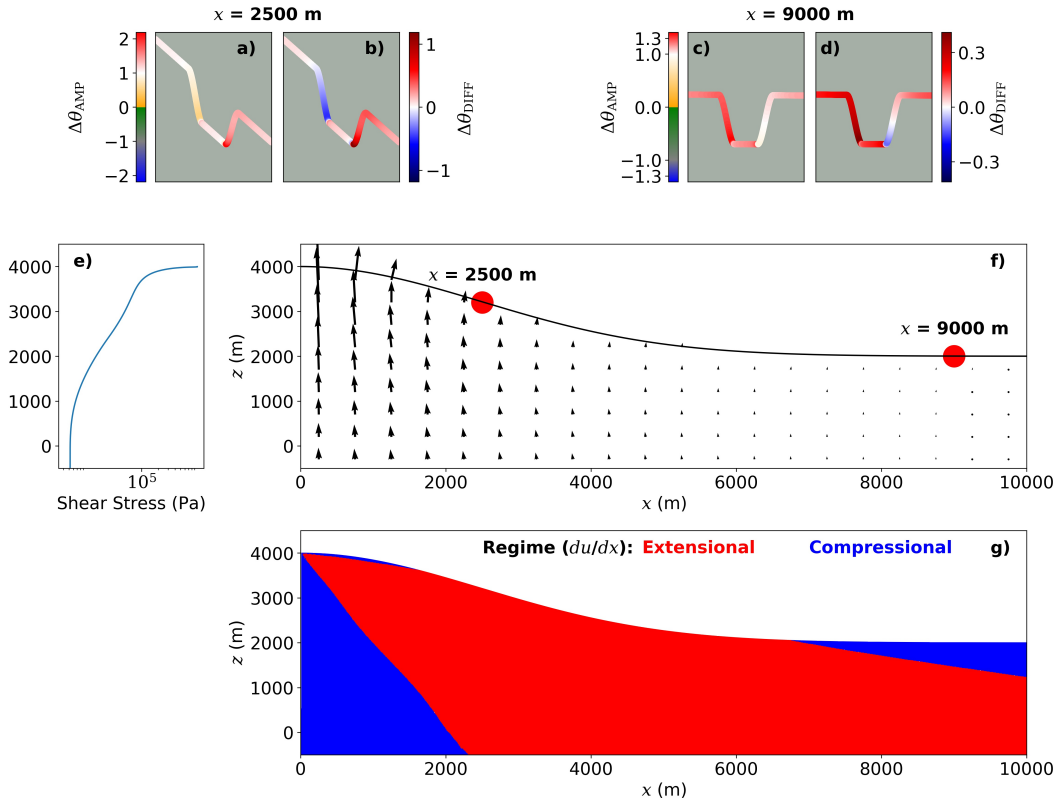

Figure 3.6: **a-d**: Amplification factor and difference due to the topographic effect on tilt produced by shear stress, where opposing slopes are included at either $x = 2500$ m or 9000 m, as indicated by red dots. **e**: Depth variant shear stress profile from flow modelling of *Marsden et al.* (2019). **f**: Amplitude and orientation of the displacement field produced by shear stress. **g**: du/dx, red where positive and horizontal displacement is increasing with increasing x, and so the horizontal distance between points is increasing (extension), blue where negative and the horizontal distance between points is decreasing (compression)

the tilt is amplified at the base of the each slope.

If the surface is flat, an extensional regime is only observed close to the surface within a few hundred metres of the conduit (Figure 3.7). However, where the relief is considerable, an extensional regime is exerted at the surface at much greater distances from the conduit. Therefore, whether the tilt is amplified or reduced by local topography depends on the relief of the edifice and the location of the topographic feature.

3.4.3 Conduit pressure

Conduit pressure produces a predominantly horizontal displacement field close to the conduit (Figure 3.3), and the amplitude of this displacement decreases with increasing distance from the conduit (Figure 3.2C). Wherever this is the case, opposing slopes introduced close to the conduit will be pushed closer together by conduit pressure and steepen, i.e. $\Delta\theta_{\mathrm{DIFF}}$ will be positive on the proximal slope and negative on the distal

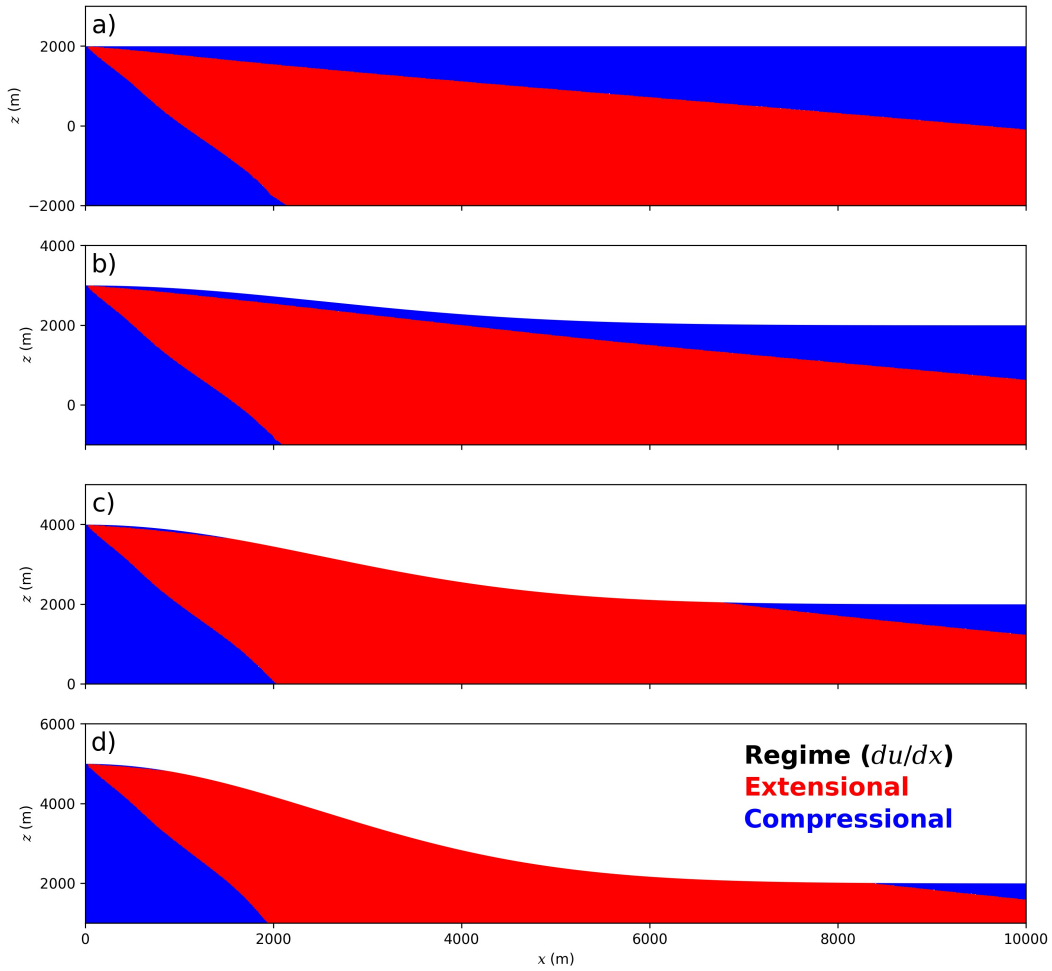

Figure 3.7: du/dx, red where positive and horizontal displacement is increasing with increasing x, and so the horizontal distance between points is increasing (extension). Blue where negative, and the horizontal distance between points is decreasing (compression). Results are presented for edifices with heights between 2000 and 5000 m.

slope (Figures 3.8b and 3.8d). In the absence of local topography, the polarity of the reference tilt, $\Delta\theta_{\mathrm{r}}$, depends on the relief of the edifice and distance from the conduit (Section 3.3), and therefore so too does $\Delta\theta_{\mathrm{AMP}}$ (Figures 3.8a and 3.8c). Where an edifice with a relief of 1 km is modelled, $\Delta\theta_{\mathrm{r}}$ is negative at $x = 0.5$ km and positive at $x = 1.5$ km. Hence, when opposing slopes are introduced at $x = 500$ m, the tilt is reduced ($\Delta\theta_{\mathrm{AMP}} < 1$) on the proximal slope and amplified ($\Delta\theta_{\mathrm{AMP}} > 1$) on the distal slope (Figure 3.8). In contrast to this, when opposing slopes are introduced at $x = 1.5$ km, the tilt is amplified on the proximal slope ($\Delta\theta_{\mathrm{AMP}} > 1$), whilst on the distal slope, $\Delta\theta_{\mathrm{AMP}} < -1$. This means that the tilt is amplified and reversed in polarity on the distal slope in this case. Therefore, topography can amplify, reduce, or reverse the polarity of tilt induced by conduit pressure depending on the relief of the edifice and the distance between the topographic feature and the conduit.

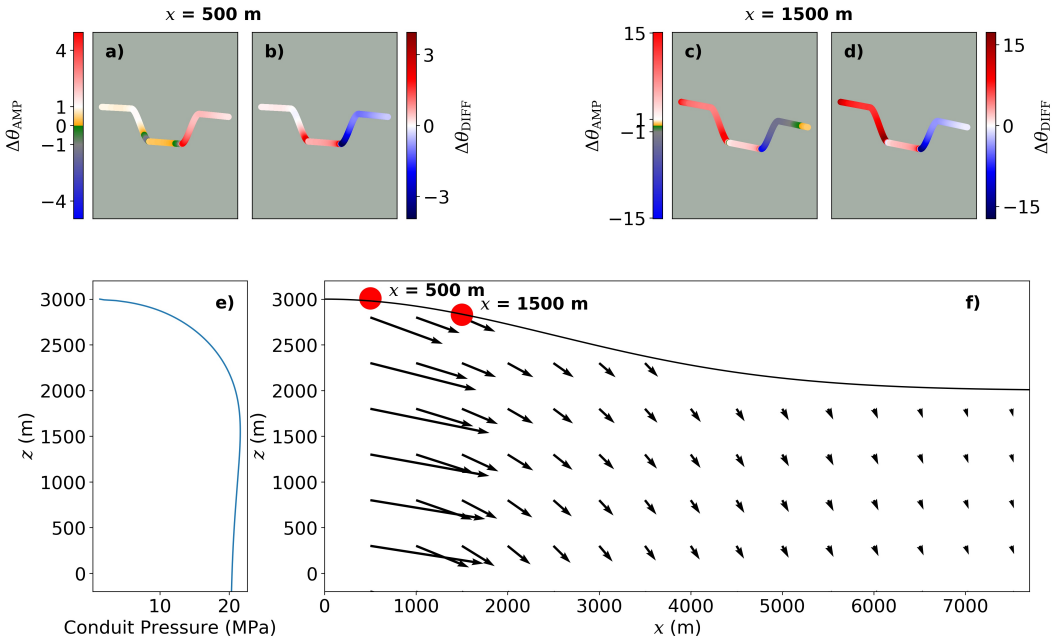

Figure 3.8: **a-d**: Amplification factor and difference due to the topographic effect on tilt produced by conduit pressure, where opposing slopes are included at either $x = 500\,\text{m}$ or $1500\,\text{m}$, as indicated by red dots. **e**: Depth variant pressure profile from flow modelling of *Marsden et al.* (2019). **f**: The amplitude and orientation of the displacement field produced by shear stress.

3.5 Real topography

The 2D axisymmetric models in Sections 3.3 and 3.4 are useful in demonstrating how exaggerated features of simplified topography can affect the tilt. However, it is important to consider whether the effect of real topography is significant or negligible. To do this, we present results of 3D deformation modelling, using $10\,\text{m} \times 10\,\text{m}$ digital elevation models (DEMs) of Tungurahua volcano, Ecuador and Soufrière Hills volcano, Montserrat (SHV), and compare how tilt varies spatially across both DEMs where topography is the only variable. We again asses the topographic effect on tilt induced by each of the sources described in Section 3.1. The mesh must be suitably fine such that the resolution of the DEM is matched. A spatially variant triangular mesh is used across the entire DEM, to a distance of almost $8\,\text{km}$ in x and y from the conduit, with a minimum element size of approximately $1\,\text{m}$ where the topography is most complex. The model is extrapolated to distance of $40\,\text{km}$ in x and y and a depth of $50\,\text{km}$, to ensure that the deformation within the region that the DEM covers is not affected by the boundary constraints, described in Section 3.3. A much coarser mesh (maximum element size approximately $7\,\text{km}$) is used for this extrapolation. We consider the maximum tilt for $\Delta\theta$, which is always positive and not necessarily radial to the source.

In defining the reference tilt, $\Delta\theta_\text{r}$, we followed the common practice where topography is not considered. Therefore, $\Delta\theta_\text{AMP}$ is the factor by which the modelled tilt is

scaled when topography is considered relative to the common practice when it is not. For tilt generated by reservoir pressure, an analytical solution was used (*Mogi*, 1958) (Equation 3.7), taking the x, y, z coordinates of each individual point across the mesh to calculate $\Delta\theta_r$. For tilt produced by conduit pressure or shear stress, in the absence of an available analytical solution, we obtain $\Delta\theta_r$ from 2D axisymmetric models using a constant slope, based on the average dip angle radially away from the summit for each edifice. The computation of this average dip angle, and a full description of these 2D axisymmetric models, is included in the supplementary material, Section B.1.

Figure 3.9 shows how the topographic effect on tilt generated by each source varies spatially across each DEM. The gradient of the topography is used to generate an illumination model, that highlights how $\Delta\theta_{AMP}$ correlates with the topography. Particularly for the reservoir or conduit pressure sources, the azimuth of the maximum tilt is often not radial to the source. Thus, if the radial rather than maximum tilt is used when inverting for the source stress, the stress amplitude could be greatly underestimated. Where the maximum tilt is orientated towards the source, an increase in stress would be falsely interpreted as a decrease in stress.

The topographic effect on tilt is most obviously apparent for tilt induced by reservoir pressure, where tilt is clearly amplified and reduced on opposing sides of topographic features such as ridges and valleys. In some cases $\Delta\theta_{AMP}$ varies by over an order magnitude over horizontal distances of just tens of metres. $\Delta\theta_{AMP}$ is very high directly above the deformation source, where $\Delta\theta_r$ approaches zero. Close to the summit, the surface tilts inwards towards the centre of the model, due to the summit being further away from the centre of the source that the surface further down slope (*McTigue and Segall*, 1988). At a large distance from the summit, the surface tilts away from the summit. At an intermediate distance between the two, $\Delta\theta$, and therefore $\Delta\theta_{AMP}$, approach zero.

The radial tilt induced by conduit pressure intercepts zero at a certain distance from the conduit, as shown in Section 3.3. Rings of apparently high $\Delta\theta_{AMP}$ values are therefore visible in Figure 3.9e-f, at constant distances from the conduit, where $\Delta\theta_r$ approaches zero. Elsewhere, tilt generated by conduit pressure is amplified or reduced by over an order of magnitude at many locations. For a shear stress source, whilst $\Delta\theta_{AMP}$ is generally closer to 1, and the direction of the maximum tilt is close to radial from the source, the topographic effect on tilt is apparent nonetheless.

Other volcanic deformation sources, such as the pressurisation of a dyke, are non-axisymmetric and so even in the absence of topography the tilt produced must be described in 3D (Figure 3.10b). Here we consider a NW-SE striking dyke, 2 m wide, 450 m long and extending from 1.2 km to 5 km below the summit, the inferred geometry of a dyke at SHV (*Costa et al.*, 2007a,b, *Hautmann et al.*, 2009). The dyke is modelled as a cuboid for simplicity, centred at $x = 0$ km, $y = 0$ km, and a pressure of 20 MPa is applied along the length of both walls of the dyke. $\Delta\theta_r$ is obtained through forward

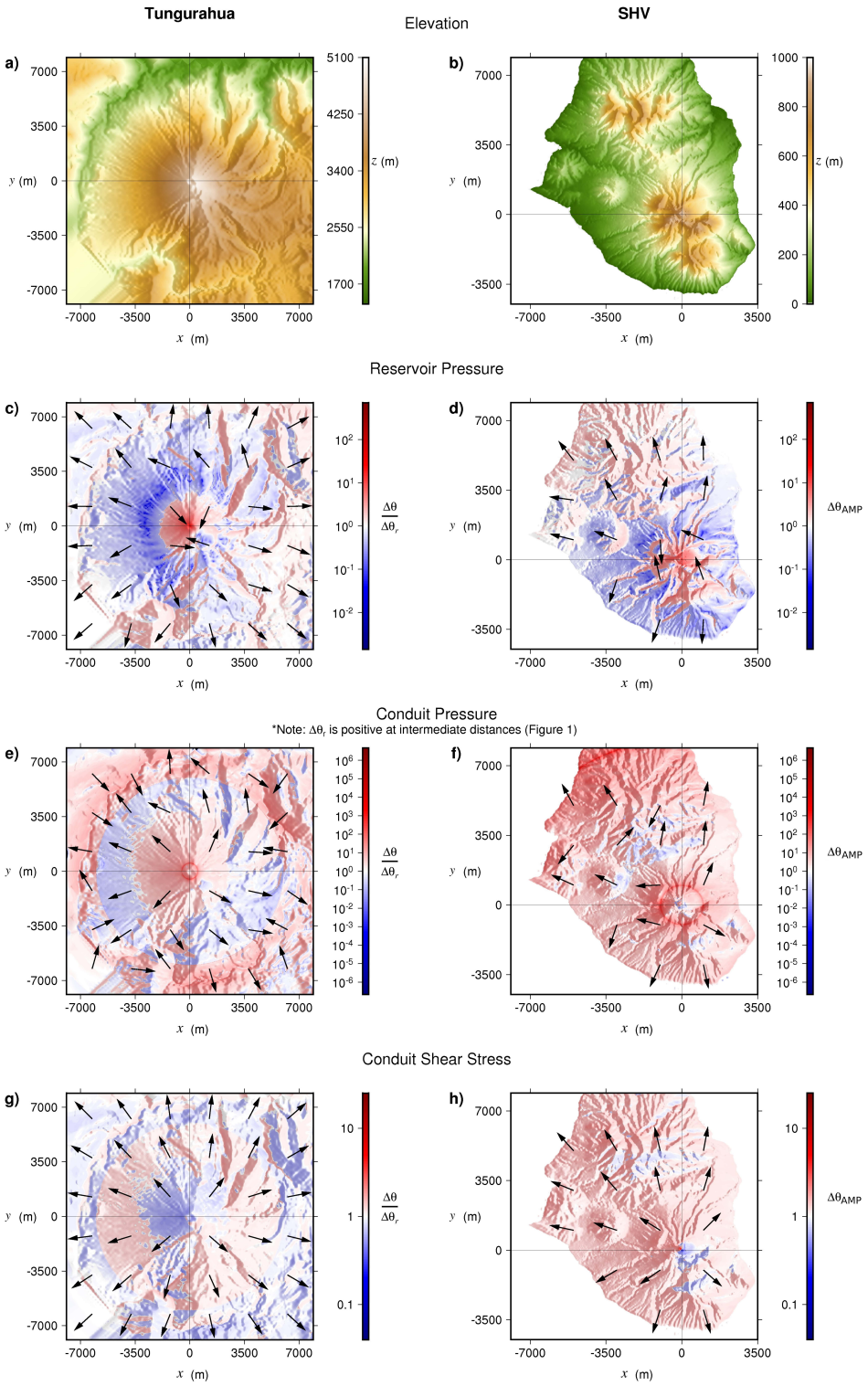

Figure 3.9: DEMs of Tungurahua volcano (left) and SHV (right) (**a-b**). Amplification factor due to the topographic effect on tilt produced by reservoir pressure (**c-d**), conduit pressure (**e-f**) or shear stress (**g-h**). The arrows depict the orientation of the maximum tilt. Note that this is often not radial to the source, located at $x = 0\,\mathrm{m}$, $y = 0\,\mathrm{m}$ in each case.

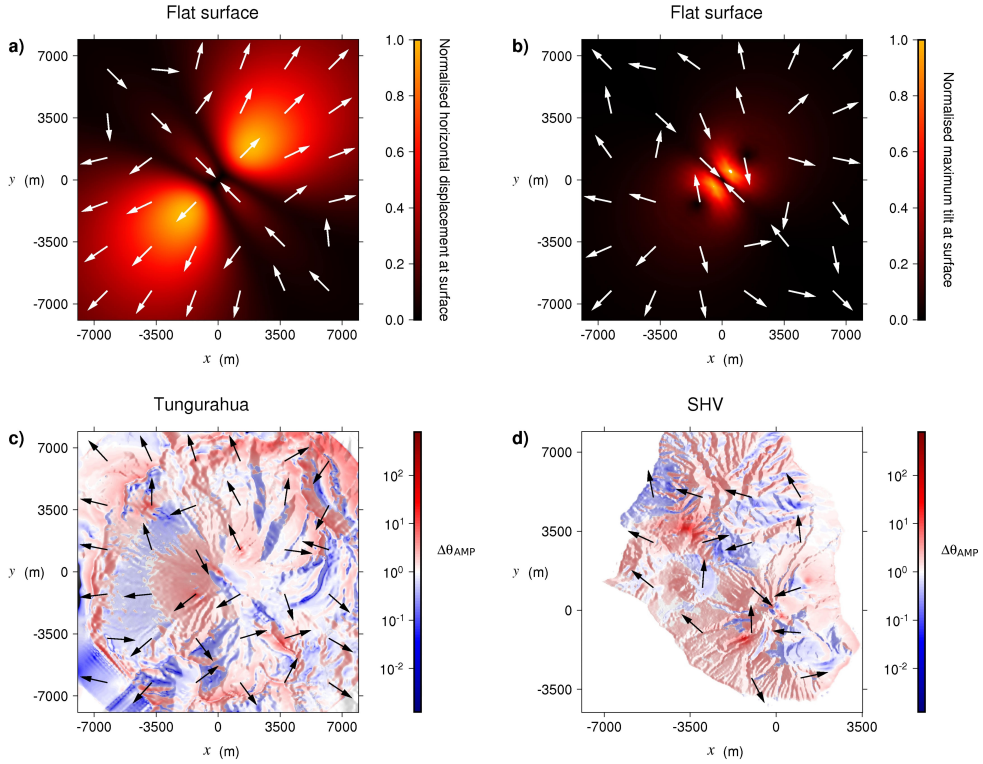

Figure 3.10: Deformation produced by the pressurisation of a NW-SE striking dyke. a) Normalised amplitude and orientation of the displacement field for a dyke 1.2 km below a flat surface, b) Normalised amplitude and orientation of the maximum tilt for the same dyke below a flat surface. c) Amplification factor due to the topographic effect on tilt for the same dyke 1.2 km below the summit of Tungurahua and d) SHV. The dyke is located at $x = 0$ m, $y = 0$ m in each case.

modelling, using an axisymmetric geometry for the edifice as used in the modelling of conduit pressure or shear stress. Hence, this modelling is performed in 3D model space to enable us to include an elongate source. The topographic effect on the tilt is complex (Figure 3.10c-d), and depends on many factors such as the dyke geometry, strike, location and depth below the surface. Since the orientation of the displacement field varies spatially (Figure 3.10a), and because there is compression and extension at different locations with respect to the dyke, it is difficult to discern generalised relationships that describe the topographic effect on tilt in this case. This emphasizes the complexity of the issue and why topography must be considered when interpreting tilt data on a case-by-case basis.

We have shown that topography can amplify, reduce, or change the direction of the maximum tilt measured. If not accounted for in the modelling processes, the topographic effect on tilt will appear as misfit between data and model output and be wrongly absorbed by inferred source parameters. This trade-off can only be avoided by deploying several stations. *Johnson et al.* (2019) showed that if multiple tiltmeters are deployed, the topographic effect on tilt can be identified as anomalous measurement at

an individual station.

3.6 Deployment recommendations

When deciding where to deploy a tiltmeter, performing 3D deformation modelling that includes a DEM and a best guess of the source type, location and geometry would be beneficial. This will enable one to assess how tilt will vary spatially due to stress for several source types. Besides deployment and maintenance, the following issues should be considered for each potential deformation source:

Reservoir pressure

- The azimuth of the maximum tilt is often not radial to the source. If the edifice has considerable relief, a decrease in the radial tilt could be induced by an increase in pressure.
- Tilt can be either significantly amplified or reduced on slopes that are considerably steeper than the surrounding topography, depending on the orientation of the displacement field relative to that slope. This is best determined through modelling.

Conduit shear stress

- A tiltmeter should be deployed as close to the conduit as possible to monitor changes in shear stress.
- Tilt can be either amplified or reduced towards the base of steep slopes, depending on the relief of the edifice, the distance from the conduit, and whether the slope is facing towards or away from the conduit.
- However, the topographic effect on tilt produced by shear stress is relatively small in most cases, and deploying a tiltmeter close to the conduit is key.

Conduit pressure

- Tilt produced due to changes in conduit pressure is greatest close to the conduit.
- An increase in pressure could be recorded as either an increase or decrease in tilt, depending on the distance between the tiltmeter and conduit and the relief of the edifice. This is best determined through modelling.
- Tilt may be smaller where the surface is parallel or perpendicular to the displacement field, and largest when the angle between the surface and deformation field is 45°. However, the strong effect of local topography will dominate over the general orientation.
- The direction of the maximum tilt is often not radial to the source.

- Tilt can be either amplified or reduced on slopes that are significantly steeper than the surrounding topography, depending on the relief of the edifice and the distance from the conduit.

3.7 Conclusions

- Through numerical modelling, we have shown that topography can amplify or reduce tilt at volcanoes by over an order of magnitude.
- The direction of maximum tilt is often not radial to the source, and in some cases an increase in stress can cause the surface to tilt inwards towards the summit of the volcano, causing a polarity change.
- If topography is not considered when inverting for the source stress, the source stress can be under or overestimated significantly. In some cases a decrease in tilt could be falsely interpreted as a decrease in stress. This could potentially have serious ramifications for forecasting changes in activity using tilt data.
- Tiltmeters can be deployed strategically near topographic features to increase the sensitivity of the instrument to changes in source stress. If a DEM is available, it is relatively simple to use numerical modelling to predict how tilt will vary spatially at any volcano, and it would be of great benefit to make this assessment prior to deploying a tiltmeter.

3.8 Acknowledgements

Luke Marsden was funded by a studentship from the NERC-SPHERES Doctoral Training Partnership (NE/L002574/1). Jürgen Neuberg is partially funded by the Centre for the Observation and Modelling of Earthquakes, Volcanoes and Tectonics (COMET NE/J01978X/1). We would like to thank Eisuke Fujita and Silvio De Angelis for providing helpful and constructive reviews and suggestions.

References

Beauducel, F., F.-H. Cornet, E. Suhanto, T. Duquesnoy, and M. Kasser (2000), Constraints on magma flux from displacements data at Merapi volcano, Java, Indonesia, *Journal of Geophysical Research: Solid Earth*, *105*(B4), 8193–8203.

Cayol, V., and F. H. Cornet (1998), Effects of topography on the interpretation of the deformation field of prominent volcanoes-Application to Etna, *Geophysical Research Letters*, *25*(11), 1979–1982.

Costa, A., O. Melnik, and R. Sparks (2007a), Controls of conduit geometry and wall-rock elasticity on lava dome eruptions, *Earth and Planetary Science Letters*, *260*(1), 137–151.

Costa, A., O. Melnik, R. Sparks, and B. Voight (2007b), Control of magma flow in dykes on cyclic lava dome extrusion, *Geophysical Research Letters*, *34*(2).

Del Negro, C., G. Currenti, and D. Scandura (2009), Temperature-dependent viscoelastic modeling of ground deformation: application to Etna volcano during the 1993–1997 inflation period, *Physics of the Earth and Planetary Interiors*, *172*(3-4), 299–309.

Harrison, J. (1976), Cavity and topographic effects in tilt and strain measurement, *Journal of Geophysical Research*, *81*(2), 319–328.

Hautmann, S., J. Gottsmann, R. S. J. Sparks, A. Costa, O. Melnik, and B. Voight (2009), Modelling ground deformation caused by oscillating overpressure in a dyke conduit at Soufrière Hills Volcano, Montserrat, *Tectonophysics*, *471*(1), 87–95.

Hautmann, S., J. Gottsmann, R. S. J. Sparks, G. S. Mattioli, I. S. Sacks, and M. H. Strutt (2010), Effect of mechanical heterogeneity in arc crust on volcano deformation with application to Soufrière Hills Volcano, Montserrat, West Indies, *Journal of Geophysical Research: Solid Earth*, *115*(B9).

Hickey, J., and J. Gottsmann (2014), Benchmarking and developing numerical finite element models of volcanic deformation, *Journal of Volcanology and Geothermal Research*, *280*, 126–130.

Johnson, J. H., M. P. Poland, K. R. Anderson, and J. Biggs (2019), A cautionary tale of topography and tilt from Kīlauea Caldera, *Geophysical Research Letters*, *46*(8), 4221–4229.

Marsden, L. H., J. Neuberg, M. Thomas, P. Mothes, and M. Ruiz (2019), Combining magma flow and deformation modelling to explain observed changes in tilt, *Frontiers in Earth Science*, *7*, 219.

McTigue, D., and P. Segall (1988), Displacements and tilts from dip-slip faults and magma chambers beneath irregular surface topography, *Geophysical Research Letters*, *15*(6), 601–604.

Mogi, K. (1958), Relations between the eruptions of various volcanoes and the deformations of the ground surfaces around them, *Bulletin of the Earthquake Research Institute, University of Tokyo*, *36*, 99–134.

Neuberg, J. W., A. S. Collinson, P. A. Mothes, M. C. Ruiz, and S. Aguaiza (2018), Understanding cyclic seismicity and ground deformation patterns at volcanoes: Intriguing lessons from Tungurahua volcano, Ecuador, *Earth and Planetary Science Letters*, *482*, 193–200.

Newman, A. V., T. H. Dixon, and N. Gourmelen (2006), A four-dimensional viscoelastic deformation model for Long Valley Caldera, California, between 1995 and 2000, *Journal of volcanology and geothermal research*, *150*(1-3), 244–269.

Ronchin, E., A. Geyer, and J. Martí (2015), Evaluating topographic effects on ground deformation: insights from finite element modeling, *Surveys in Geophysics*, *36*(4), 513–548.

Trasatti, E., C. Giunchi, and M. Bonafede (2003), Effects of topography and rheological layering on ground deformation in volcanic regions, *Journal of Volcanology and Geothermal Research*, *122*(1-2), 89–110.

Voight, B., R. Sparks, A. Miller, R. Stewart, R. Hoblitt, A. Clarke, J. Ewart, W. Aspinall, B. Baptie, E. Calder, et al. (1999), Magma flow instability and cyclic activity at Soufrière Hills Volcano, Montserrat, British West Indies, *Science*, *283*(5405), 1138–1142.

Widiwijayanti, C., A. Clarke, D. Elsworth, and B. Voight (2005), Geodetic constraints on the shallow magma system at Soufrière Hills Volcano, Montserrat, *Geophysical Research Letters*, *32*(11).

Chapter 4

Evidence for the top-down control of lava domes on magma ascent dynamics

Abstract

Lava domes form as extruded, viscous magma builds up above the conduit vent. A number of eruptions ceased with domes hundreds of metres high emplaced atop the volcano, suggestive of a top-down control. Here, we use time-dependent flow modelling in COMSOL Multiphysics to investigate how dome growth influences magma ascent. We simulate ascent through a cylindrical conduit, and progressively increase the pressure exerted at the conduit exit as a function of the extruded volume. We focus on Soufrière Hills volcano (SHV), where since 1995 multiple lava domes have grown to approximately the same height before dome collapse or extrusion ceased. We show that pressure and frictional forces involved in the formation of large domes can be sufficient to overcome the forces driving ascent and stall an eruption. However, an eruption can resume if the forces impeding ascent are overcome.

4.1 Introduction

Lava domes are formed as viscous magma extrudes from a volcanic conduit and builds up above it. As they grow, the loading pressure, P_{L}, and the resulting vertical force, F_{L}, at the top of the conduit increases as a function of the mean height of the dome above the conduit, h_{d}, such that

$$P_{\mathrm{L}} = \rho_{\mathrm{d}} g h_{\mathrm{d}}, \tag{4.1}$$

where ρ_{d} is the density of the dome and g is gravity. Dome collapse and the resultant

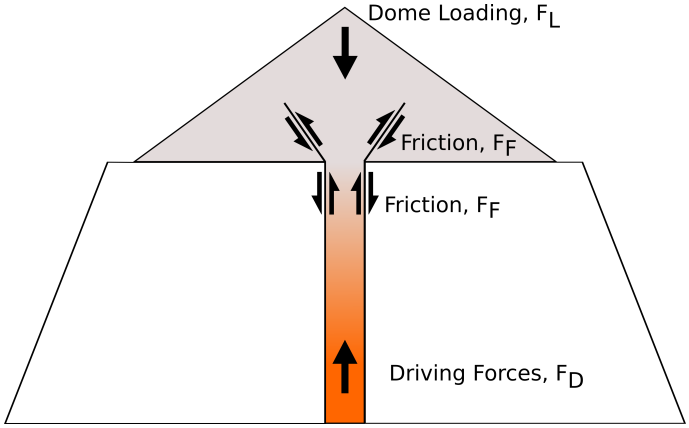

Figure 4.1: Schematic diagram depicting the forces that govern magma ascent in dome forming eruptions. F_D: Magma ascent is driven by it's buoyancy relative to the surrounding edifice and overpressure depth. F_L: The dome exerts a loading force on the conduit vent, proportional to the dome height. F_F: Friction must be overcome for magma to ascent, both at the conduit wall and in breaking and displacing overlying dome rock.

decompression within the conduit can lead to Vulcanian explosions and hazardous pyroclastic flows and surges. Whilst much work has been published that investigates dome growth (e.g. *Hale*, 2008, *Harnett et al.*, 2018) or possible triggers of their collapse (e.g. *Ui et al.*, 1999, *Elsworth et al.*, 2004, *Harnett et al.*, 2019), fewer studies focus on their their top-down control on ascent dynamics.

One can consider the ascent of magma through a conduit to be governed by a vertical, loading force, F_L, that opposes the forces that drive magma extrusion, F_D (Figure 4.1). These driving forces include the buoyancy of magma relative to the surrounding edifice, and an upwards force resulting from the overpressure at depth. *Melnik and Sparks* (1999) showed that the ascent velocity decreases as the loading force due to dome growth increases. This allows more time for crystallisation and outgassing, which further inhibit magma ascent. *Chevalier et al.* (2017) showed that the increase in loading force causes the permeability of the conduit and surrounding edifice to decrease, leading to an increase in overpressure in the upper conduit.

Domes at a number of volcanoes remain stable long after emplacement, including at La Soufriére, St Vincent (*Boudon et al.*, 2008) and Redoubt volcano, USA (*Bull et al.*, 2013). It has been suggested that if the dome is sufficiently tall, the ascending magma column reaches equilibrium ($F_L = F_D$), and so extrusion ceases (*Bull et al.*, 2013). One must also consider that where magma solidifies in or above the upper conduit, a frictional force, F_F, must also be overcome for magma to ascend (*Iverson et al.*, 2006). This frictional force encompasses both friction at conduit wall and dome rock that must be fractured and pushed out of the way to allow ascent. This conceptual model offers a simple explanation as to why some eruptions cease with a large dome emplaced above the vent. However, the height of uncollapsed, stable domes varies significantly from one volcano to the next. In this study, we investigate how ascent

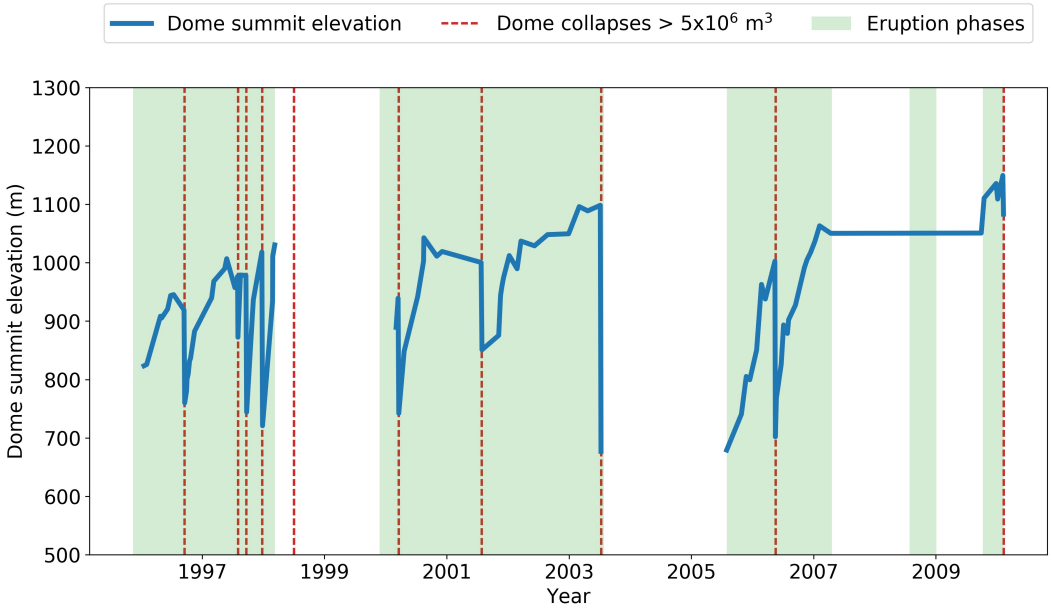

Figure 4.2: Maximum elevation of the dome at SHV through time. Elevations within phases 1-5 from *Wadge et al.* (2014). Dome collapse events with deposit greater than $5 \times 10^6\,\mathrm{m}^3$ (*Harnett et al.*, 2019). The conduit vent was at an approximate elevation of 710 m in July 2003 (*S.A.C. on Montserrat Volcanic Activity*, 2004)

dynamics evolve through time due to dome growth, and what key factors control the critical height that a dome can grow to before the eruption stalls. We focus on Soufrière Hills volcano (SHV), Montserrat, which has a well-documented history (*Wadge et al.*, 2014) of multiple cycles of dome growth and collapse between 1995 and 2010 (Figure 4.2).

4.2 The model

We build upon the 2D axisymmetric flow modelling of *Collier and Neuberg* (2006), *Thomas and Neuberg* (2014) and *Marsden et al.* (2019a), using the Laminar Flow module in COMSOL Multiphysics v5.4. A reference flow model has been parameterised based on SHV (Table 4.1), and we investigate what key parameters influence the height a dome can grow to. To appropriately simulate transient volcanic processes that evolve over relatively short time periods, a fully time dependent flow model must be used, that can model disequilibrium in the system. The ascent of isothermal magma through a cylindrical conduit is governed by a compressible form of the Navier Stokes equation and the continuity equation. To represent dome loading, the loading pressure exerted on the conduit exit is increased through time as a function of the extruded volume, or more precisely the height of the dome (Eq. 4.1). We use a constant value for the density of the dome, $\rho_\mathrm{d} = 2560\,\mathrm{kg/m}^3$, based on the bulk density of fully out-gassed magma at the top of the conduit at time zero in our reference flow model. We model

the dome as a cone, the gradient of which is held constant through time at 35°. The dome height and radius increase with the extruded volume (Figure 4.3). We map how key parameters vary spatially within the conduit and track how the system evolves through time. We investigate which key parameters govern the critical dome height at which an eruption ceases, assuming that conditions at depth remain constant through time.

Symbol	Description	Values in reference model [range considered]	Reference
T	Magma temperature	1100 K	*Devine et al.* (2003)
R	Conduit radius	10 m	
L	Conduit length	5 km	*Barclay et al.* (1998)
P_a	Atmospheric pressure	0.1 MPa	
P_e	Excess pressure at conduit base	10 MPa [0,20 MPa]	*Sparks* (1997)
ρ_e	Density of edifice	2680 kg/m^3	
ρ_d	Density of dome	2560 kg/m^3	
ρ_c	Average crystal density	2700 kg/m^3	*Burgisser et al.* (2010)
ϕ_{ph}	Initial content of phenocrysts	40 vol.%	*Barclay et al.* (1998)
ϕ_c^{max}	Max. packing fraction	0.595	*Mueller et al.* (2011)
C_{wi}	Initial H_20 content	4.5 wt.% [0,10 wt.%]	*Barclay et al.* (1998)
g	Acceleration due to gravity	9.81 m/s^2	
γ	Constant corresponding to crystal growth rate	4×10^{-6} s^{-1} [10^{-6}-7.3×10^{-6} s^{-1}]	
θ_d	Slope angle of lava dome	35°	

Table 4.1: Key parameters and variables used in the reference flow model, based on SHV.

We consider water as the only volatile species, and assume homogeneous bubble nucleation as a function of pressure *Zhang et al.* (2007). An empirically derived depth-dependent profile is used to account for outgassing in the upper conduit (*Marsden et al.*, 2019a). The melt viscosity, η_m, (*Giordano et al.*, 2008) and density (*Spera*, 2000) are each a function of the composition (*Barclay et al.*, 1998), pressure, P, and temperature, T. The bulk magma is considered a three-phase non-Newtonian fluid, and the bulk viscosity, η_b, is modulated by the gas and crystal content and strain rate (*Truby et al.*, 2015)

$$\eta_b = \eta_m \left(\eta_{r\infty} + \frac{\eta_{r0} - \eta_{r\infty}}{1 + KCa^m} \right) \left(1 - \frac{\phi_c}{\phi_c^{max}} \right)^{-2}, \tag{4.2}$$

where Ca is the capillary number, a function of the strain rate (*Rust and Manga*, 2002). η_{r0} and $\eta_{r\infty}$ are the zero and infinite shear rate relative viscosities, respectively, each a function of the gas volume fraction (*Llewellin and Manga*, 2005). $K = 6/5$ and $m = 2$ are empirical constants (*Mader et al.*, 2013). The bulk viscosity increases as the crystal content, ϕ_c, approaches the maximum packing fraction ϕ_c^{max}, at which point the suspension is assumed jammed. We include decompression-induced crystallisation using the following equation used in recent numerical magma ascent models (*Kozono and Koyaguchi*, 2012, *Okumura and Kozono*, 2017), based on experimental data by

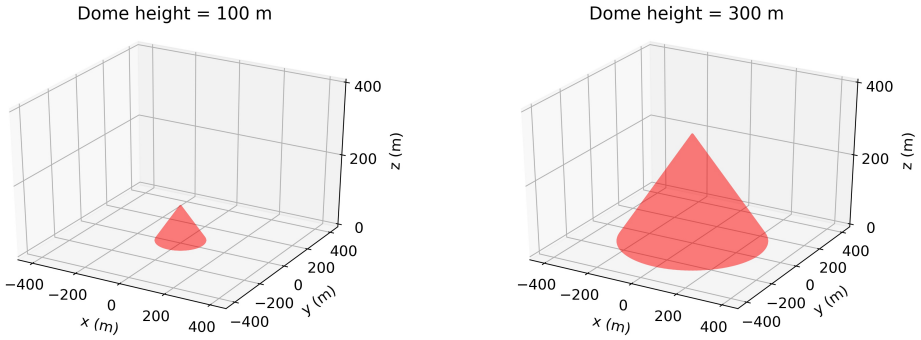

Figure 4.3: A conical geometry is assumed for the dome, the slope of which is held constant as the dome grows.

Couch et al. (2003a).

$$\frac{d\phi_c}{dt} + v_z \frac{d\phi_c}{dz} = \gamma \phi_c^{2/3} \left(\phi_c^{eq} - \phi_c\right). \tag{4.3}$$

The rate of crystallisation, $d\phi_c/dt$, is a function of the ascent velocity, v_z, and a constant that corresponds to the crystal growth rate, γ. ϕ_c^{eq} is the equilibrium crystal content, a function of pressure, P, derived experimentally by *Couch et al.* (2003b), such that

$$\begin{aligned} &\phi_c^{eq} = \phi_{ph} + (1 - \phi_{ph}) \left[C_0 + C_1 \ln\left(10^{-6} P\right) + C_2 \left\{ \ln\left(10^{-6} P\right) \right\}^2 \right] \\ &C_0 = 0.842; \quad C_1 = -9.54 \times 10^{-2}; \quad C_2 = -1.16 \times 10^{-2}. \end{aligned} \tag{4.4}$$

The content of phenocrysts, ϕ_{ph}, is the initial value set at the base of the conduit. The crystal content at any depth, ϕ_c, comprises phenocrysts and microlites, and depends heavily on γ. Since γ is poorly constrained, and is dependent on the magma viscosity (*Arzilli et al.*, 2015), we tune this parameter to achieve a critical dome height in our reference model consistent with that observed at SHV (Figure 4.2).

As the ascent rate decreases, crystals have more time to grow, and therefore the bulk viscosity of the magma increases, which causes the ascent rate to decrease further. *Melnik and Sparks* (2002) showed that an unrealistically high loading pressure is required to stall magma ascent if this process is neglected. Due to the non-linear relationship between crystallisation and ascent rate, small changes in factors that drive ascent can lead to significant changes in ascent rate. Where $\phi_c = \phi_c^{max}$, magma is assumed to behave as a solid that can no longer flow. The solidified magma can be incremently pushed up the conduit by the ascending magma beneath it (*Iverson et al.*, 2006), whilever $F_D > F_L + F_F$. As this solidified region at the top of the conduit extends, F_F increases until the eruption ceases. Equation 4.2 approaches a singularity where ϕ_c approaches ϕ_c^{max}. Hence, we terminate our model run at the time that

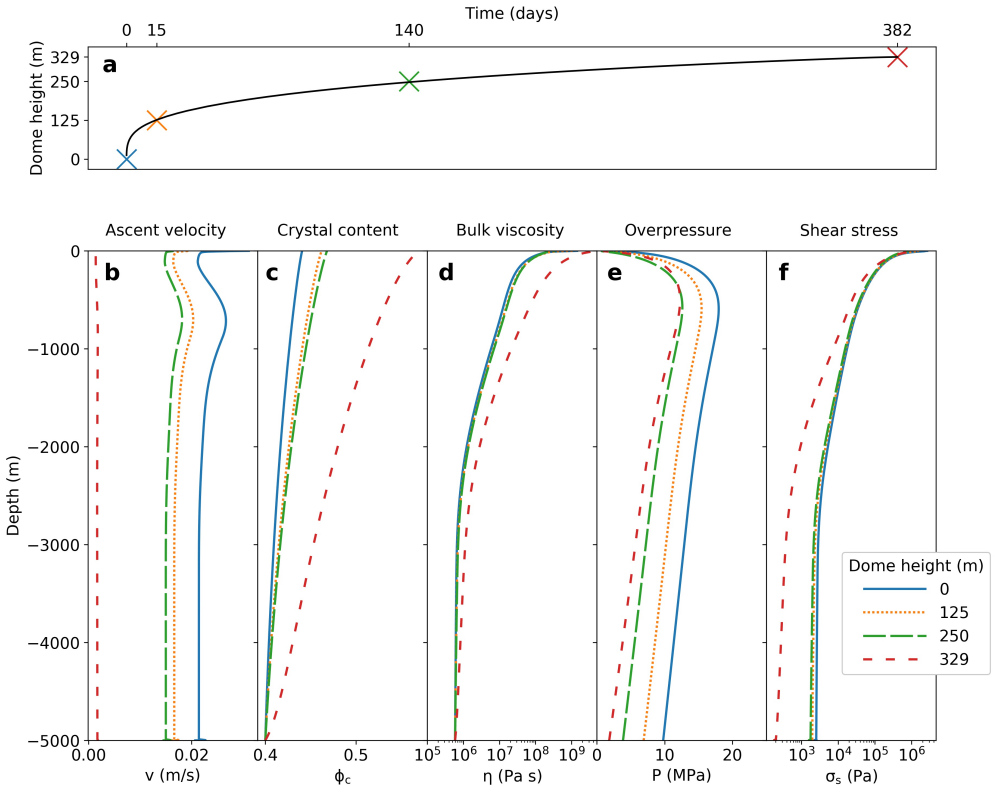

Figure 4.4: Parameters obtained from the reference flow model. a) Dome height through time. Depth profiles of key variables obtained from the reference flow model, at the conduit centre (b) - (d), at the conduit wall (e) - (f).

$\phi_c/\phi_c^{max} = 97\,\%$ at any point in the model, at which point $\eta_b/\eta_m = 1000$. Approaching this point, the extrusion rate is slow relative to the rate that ϕ_c is increasing. Beyond this point, further dome growth is negligible. A full description of the model is provided in the supplementary material (Section C).

4.3 Dome growth through time

Figure 4.4 shows how dome growth through time influences ascent dynamics in our reference model. The rate at which the ascent velocity decreases, and the crystal content and therefore magma viscosity increase, accelerates approaching the critical dome height, due to the feedback cycle between ascent velocity and crystallisation. The modelled extrusion rates of up to $4\,m^3/s$ are consistent with typical estimated extrusion rates at SHV (*Harnett et al.*, 2019, *Wadge et al.*, 2010). The modelled dome growth through time also follows a similar profile to observed dome growth beginning 1st October 1996 at SHV (Figure 4.5), that stalled after approximately 60 days (*Melnik and Sparks*, 2002). Low extrusion rates and strong deformation of the volcano's flanks were measured before extrusion temporarily ceased in early December, 1996 (*Young*

et al., 1998). Near-field deformation can be driven by changes in shear stress exerted on the conduit walls as magma ascends, that pulls the surrounding edifice upwards, or overpressure that pushes the edifice outwards (*Marsden et al.*, 2019a). Our modelling suggests that this strong flank deformation was driven by changes in shear stress, which changes most significantly as the dome approaches its critical height (Figure 4.4f). Conversely, changes in overpressure are more pronounced earlier during the dome growth (Figure 4.4e). Subsidence due to the increasing weight of the dome can mask deformation induced by changes in shear stress or overpressure (*Odbert et al.*, 2015, *Chevalier et al.*, 2017). However, in early December 1996 when dome growth was slow, deformation produced by changes in shear stress may not have been masked by subsidence from changes in the weight of the dome.

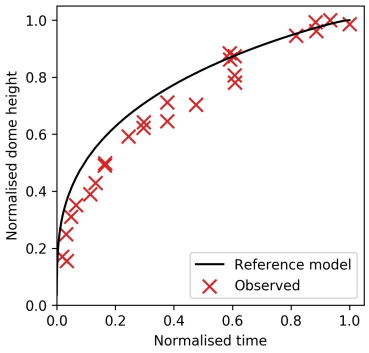

Figure 4.5: Normalised dome height through time. Observed dome heights from dome growth at SHV that began on 1st October 1996 (*Melnik and Sparks*, 2002) versus obtained through the reference flow model.

4.4 Key factors controlling the critical dome height

At SHV, lava domes have repeatedly grown to, but never exceeded, a maximum elevation of 1150 m above sea level, approximately 400-500 m above the assumed elevation of the conduit vent (*S.A.C. on Montserrat Volcanic Activity*, 2004). The consistency of a critical dome height is suggestive that there is a consistent loading pressure that, when reached, magma ascent ceases. However, domes with a range of heights have remained stable long after eruption ceased at other volcanoes (Figure 4.6). At some volcanoes, magma stalls in the upper conduit, forming a plug that causes ascent to stall without the extrusion of a dome, hence friction and load exerted by the magma plug are sufficient.

The critical dome height to which a dome can grow before extrusion stalls is dependent on several factors. It is sensitive to the relative rates of magma ascent and crystallisation (Figure 4.7a). If crystallisation is slow with respect to the ascent velocity, the eruption may not cease until the dome is greater than 1000 m in height, at which point dome loading balances the forces that drive magma ascent. However, if the rate

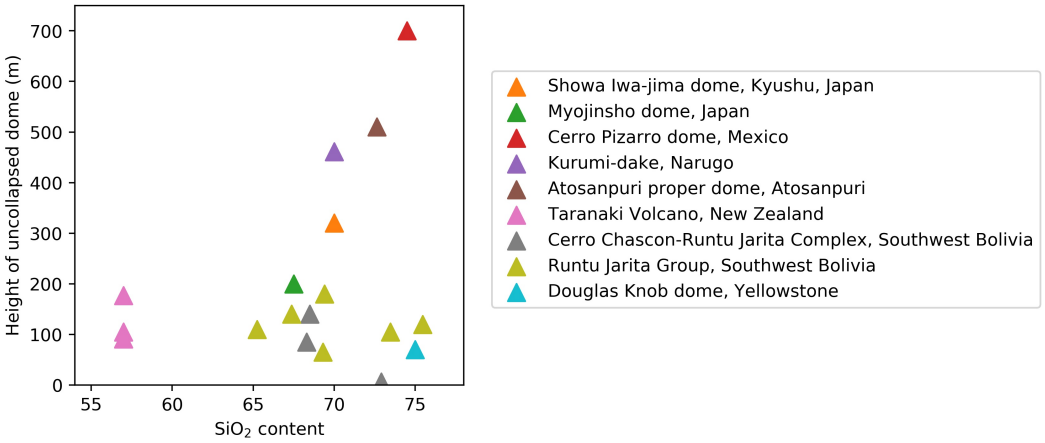

Figure 4.6: Heights of uncollapsed domes from their base to top, plotted against SiO_2 content, from (*Harnett et al.*, 2019) and references therein. There does not appear to be any clear correlation between dome height and SiO_2 content, which suggests that other factors control the height a dome can grow to before extrusion stalls.

of crystallisation is relatively quick, frictional forces also impede ascent, and extrusion ceases with a much smaller dome above the conduit. If the rate of crystallisation is sufficiently quick, magma may solidify in the upper conduit, forming a viscous plug and no dome at the surface. The rate of crystallisation is poorly constrained and dependent on the viscosity (*Arzilli et al.*, 2015), therefore one should note that the critical dome height is sensitive to relative changes in the rate of crystallisation and not the absolute values used for γ in this particular modelling attempt.

One may expect the critical height a dome can grow to be a function of the melt composition, which influences the viscosity *Giordano et al.* (2008) and therefore ascent rate. However, data from the GLADIS database of global lava domes (*Harnett et al.*, 2019) suggest that there is no correlation between the height an uncollapsed dome reached before extrusion stalled and the SiO_2 content (Figure 4.6), a key control on melt viscosity (*Giordano et al.*, 2008). This critical dome height must therefore be mainly controlled by other factors that govern the relative rates of crystallisation and magma ascent. The permeability of the magma column, surrounding edifice, and dome influence the amount of exsolved gas that can escape from the conduit, and therefore the buoyancy of the magma column. Figure 4.7d shows that if more gas is able to escape, the loading pressure required to stall the eruption is smaller. An increase in gas flux can alternatively be explained by an injection of volatile rich magma at depth. Conversely, an increase in the initial volatile content of the melt, C_{wi}, would cause the buoyancy of the magma column to increase, making it possible for a larger dome to form (Figure 4.7c). Therefore, monitoring how the extrusion rate changes through time could help one to constrain whether an observed increase in gas flux is a consequence of an injection of volatiles into the system (extrusion rate predicted to increase) or an increase in how much gas is able to escape (extrusion rate predicted to

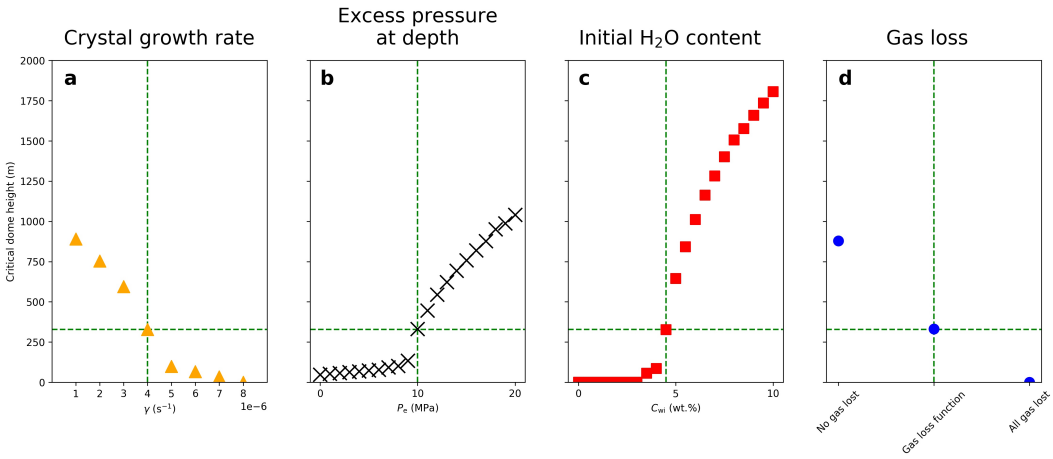

Figure 4.7: Changes in the critical height that a dome can grow to before extrusion stalls, as a function of the a) rate of crystallisation, b) excess pressure at the base of the conduit, c) initial volatile content, d) amount of gas that is lost from the conduit. Values used in the reference flow model are given where the dashed lines intersect.

decrease). Additionally, higher loading pressure is required to balance against larger excess pressure at depth, P_e (Figure 4.7b). Hence, observed inflation of the edifice linked to pressurisation of a shallow magma reservoir (*Mogi*, 1958) could lead to an increase in the extrusion rate, or cause a stalled eruption to recommence.

Moderate changes in the driving pressure gradient, volatile content, outgassing or crystal growth rate can significantly influence the critical height that a dome can reach (Figure 4.7). In other words, forces driving ascent, F_D, and consequently the amplitude of the forces required to balance them, F_L and F_F, are highly sensitive to changes in these parameters. At SHV, extrusion has repeatedly stalled at a fairly consistent dome height. This implies that the forces driving the eruption, F_D, and the conditions at depth, may have also remained relatively constant throughout the lifespan of the eruption. Changes in the dome height and the loading pressure it exerts may have been the main factor modulating the extrusion rate and eruption dynamics.

4.5 Conclusions

Loading pressure from the growth of a lava dome impedes magma ascent, and can cause it to stall. This is an example of a top-down control mechanism on ascent dynamics, and may explain why some eruptions cease with a metastable dome emplaced for decades after the eruption. The critical height that a dome can grow to mainly depends on the excess pressure in the system, the volatile content of the magma and how much gas can escape from the conduit (Figure 4.7). Where crystallisation is slow relative to the ascent velocity of magma, a large dome can form. However, where crystallisation is faster, magma may solidify in the upper conduit, forming a plug. Ascent is impeded by friction at the conduit walls, but can continue as long as friction between the solidified

plug and the surrounding edifice is exceeded by forces driving ascent. If frictional forces are sufficiently large, ascent may cease without the extrusion of a lava dome. At SHV, lava domes have repeatedly grown to a similar elevation (Figure 4.2). Hence, we speculate that conditions at depth have remained stable throughout the lifespan of the eruption, and changes in dome height through time have been the main controlling factor modulating eruption dynamics.

We have shown that ascent dynamics change most significantly as the dome approaches its critical height (Figure 4.4), due to the non-linear control of crystallisation (*Melnik and Sparks*, 1999) on the ascent velocity. Consequently, an observed decrease in the extrusion rate could be a precursor to extrusion stalling. It may be possible to observe deformation driven by an increase in shear stress (*Marsden et al.*, 2019a) as the dome approaches its critical height. Instrumentation has to be deployed strategically, i.e. close enough to the conduit and considering the topographic effect on tilt (*Marsden et al.*, 2019b). However, this effect may be masked by deformation due to dome loading (*Odbert et al.*, 2015).

This research demonstrates that top-down controls within the volcanic plumbing system can be significant and can cause an eruption to stall, at least temporarily. However, an increase in the forces that drive magma ascent, e.g. resulting from an injection of a fresh batch of magma, could overcome the loading and frictional forces impeding ascent, and cause an eruption to resume. Alternatively, lava domes can collapse without any precursory unrest, due to gravitational collapse (*Swanson et al.*, 1987), or external triggers such as intense rainfall (*Elsworth et al.*, 2004) or earthquakes (*Platz et al.*, 2012) for example. This would lead to an instantaneous reduction in the loading pressure, which could cause an eruption to resume even after a long period of quiescence.

References

Arzilli, F., C. Agostini, P. Landi, A. Fortunati, L. Mancini, and M. Carroll (2015), Plagioclase nucleation and growth kinetics in a hydrous basaltic melt by decompression experiments, *Contributions to Mineralogy and Petrology*, *170*(5-6), 55.

Barclay, J., M. J. Rutherford, M. Carroll, M. Murphy, J. Devine, J. Gardner, and R. Sparks (1998), Experimental phase equilibria constraints on pre-eruptive storage conditions of the Soufrière Hills magma, *Geophysical Research Letters*, *25*(18), 3437–3440.

Boudon, G., J.-C. Komorowski, B. Villemant, and M. P. Semet (2008), A new scenario for the last magmatic eruption of La Soufrière of Guadeloupe (Lesser Antilles) in 1530 AD Evidence from stratigraphy radiocarbon dating and magmatic evolution of erupted products, *Journal of Volcanology and Geothermal Research*, *178*(3), 474–490.

Bull, K. F., S. W. Anderson, A. K. Diefenbach, R. L. Wessels, and S. M. Henton (2013), Emplacement of the final lava dome of the 2009 eruption of Redoubt Volcano, Alaska, *Journal of Volcanology and Geothermal Research*, *259*, 334–348.

Burgisser, A., S. Poussineau, L. Arbaret, T. H. Druitt, T. Giachetti, and J.-L. Bourdier (2010), Pre-explosive conduit conditions of the 1997 Vulcanian explosions at Soufrière Hills Volcano, Montserrat: I. Pressure and vesicularity distributions, *Journal of Volcanology and Geothermal Research*, *194*(1), 27–41.

Chevalier, L., M. Collombet, and V. Pinel (2017), Temporal evolution of magma flow and degassing conditions during dome growth, insights from 2D numerical modeling, *Journal of Volcanology and Geothermal Research*, *333*, 116–133.

Collier, L., and J. Neuberg (2006), Incorporating seismic observations into 2D conduit flow modeling, *Journal of Volcanology and Geothermal Research*, *152*(3), 331–346.

Couch, S., R. Sparks, and M. Carroll (2003a), The kinetics of degassing-induced crystallization at Soufrière Hills Volcano, Montserrat, *Journal of Petrology*, *44*(8), 1477–1502.

Couch, S., C. Harford, R. Sparks, and M. Carroll (2003b), Experimental constraints on the conditions of formation of highly calcic plagioclase microlites at the Soufrière Hills Volcano, Montserrat, *Journal of Petrology*, *44*(8), 1455–1475.

Devine, J., M. Rutherford, G. Norton, and S. Young (2003), Magma storage region processes inferred from geochemistry of Fe–Ti oxides in andesitic magma, Soufriere Hills Volcano, Montserrat, WI, *Journal of Petrology*, *44*(8), 1375–1400.

Elsworth, D., B. Voight, G. Thompson, and S. Young (2004), Thermal-hydrologic mechanism for rainfall-triggered collapse of lava domes, *Geology*, *32*(11), 969–972.

Giordano, D., J. K. Russell, and D. B. Dingwell (2008), Viscosity of magmatic liquids: a model, *Earth and Planetary Science Letters*, *271*(1), 123–134.

Hale, A. (2008), Lava dome growth and evolution with an independently deformable talus, *Geophysical Journal International*, *174*(1), 391–417.

Harnett, C. E., M. E. Thomas, M. D. Purvance, and J. Neuberg (2018), Using a discrete element approach to model lava dome emplacement and collapse, *Journal of Volcanology and Geothermal Research*, *359*, 68–77.

Harnett, C. E., M. E. Thomas, E. S. Calder, S. K. Ebmeier, A. Telford, W. Murphy, and J. Neuberg (2019), Presentation and analysis of a worldwide database for lava dome collapse events: the Global Archive of Dome Instabilities (GLADIS), *Bulletin of Volcanology*, *81*(3), 16.

Iverson, R. M., D. Dzurisin, C. A. Gardner, T. M. Gerlach, R. G. LaHusen, M. Lisowski, J. J. Major, S. D. Malone, J. A. Messerich, S. C. Moran, et al. (2006), Dynamics of seismogenic volcanic extrusion at Mount St Helens in 2004–05, *Nature*, *444*(7118), 439–443.

Kozono, T., and T. Koyaguchi (2012), Effects of gas escape and crystallization on the complexity of conduit flow dynamics during lava dome eruptions, *Journal of Geophysical Research: Solid Earth*, *117*(B8).

Llewellin, E., and M. Manga (2005), Bubble suspension rheology and implications for conduit flow, *Journal of Volcanology and Geothermal Research*, *143*(1), 205–217.

Mader, H., E. Llewellin, and S. Mueller (2013), The rheology of two-phase magmas: A review and analysis, *Journal of Volcanology and Geothermal Research*, *257*, 135–158.

Marsden, L. H., J. Neuberg, M. Thomas, P. Mothes, and M. Ruiz (2019a), Combining magma flow and deformation modelling to explain observed changes in tilt, *Frontiers in Earth Science*, *7*, 219.

Marsden, L. H., J. Neuberg, and M. Thomas (2019b), Topography and tilt at volcanoes, *Frontiers in Earth Science*, *7*, 317.

Melnik, O., and R. Sparks (1999), Nonlinear dynamics of lava dome extrusion, *Nature*, *402*(6757), 37.

Melnik, O., and R. Sparks (2002), Dynamics of magma ascent and lava extrusion at Soufrière Hills Volcano, Montserrat, *Geological Society, London, Memoirs*, *21*(1), 153–171.

Mogi, K. (1958), Relations between the eruptions of various volcanoes and the deformations of the ground surfaces around them, *Bulletin of the Earthquake Research Institute, University of Tokyo*, *36*, 99–134.

Mueller, S., E. Llewellin, and H. Mader (2011), The effect of particle shape on suspension viscosity and implications for magmatic flows, *Geophysical Research Letters*, *38*(13).

Odbert, H., B. Taisne, and J. Gottsmann (2015), Deposit loading and its effect on co-eruptive volcano deformation, *Earth and Planetary Science Letters*, *413*, 186–196.

Okumura, S., and T. Kozono (2017), Silicic lava effusion controlled by the transition from viscous magma flow to friction controlled flow, *Geophysical Research Letters*, *44*(8), 3608–3614.

Platz, T., S. J. Cronin, J. N. Procter, V. E. Neall, and S. F. Foley (2012), Non-explosive, dome-forming eruptions at Mt. Taranaki, New Zealand, *Geomorphology*, *136*(1), 15–30.

Rust, A., and M. Manga (2002), Effects of bubble deformation on the viscosity of dilute suspensions, *Journal of non-newtonian fluid mechanics*, *104*(1), 53–63.

S.A.C. on Montserrat Volcanic Activity (2004), Assessment of the hazards and risks associated with the Soufrière Hills volcano, Montserrat. Second Report of the Scientific Advisory Committee on Montserrat Volcanic Activity. Part 2, Technical Report.

Sparks, R. S. J. (1997), Causes and consequences of pressurisation in lava dome eruptions, *Earth and Planetary Science Letters*, *150*(3-4), 177–189.

Spera, F. J. (2000), Physical properties of magma, *Encyclopedia of volcanoes*, *176*.

Swanson, D., D. Dzurisin, R. Holcomb, E. Iwatsubo, W. Chadwick Jr, T. Casadevall, J. Ewert, and C. Heliker (1987), Growth of the lava dome at Mount St. Helens, Washington (USA), *The emplacement of silicic domes and lava flows, Geological Society of America, Boulder, Special Paper*, *212*, 1–16.

Thomas, M. E., and J. W. Neuberg (2014), Understanding which parameters control shallow ascent of silicic effusive magma, *Geochemistry, Geophysics, Geosystems*, *15*(11), 4481–4506.

Truby, J., S. Mueller, E. Llewellin, and H. Mader (2015), The rheology of three-phase suspensions at low bubble capillary number, in *Proc. R. Soc. A*, vol. 471, p. 20140557, The Royal Society.

Ui, T., N. Matsuwo, M. Sumita, and A. Fujinawa (1999), Generation of block and ash flows during the 1990–1995 eruption of Unzen Volcano, Japan, *Journal of Volcanology and Geothermal Research*, *89*(1-4), 123–137.

Wadge, G., R. Herd, G. Ryan, E. Calder, and J.-C. Komorowski (2010), Lava production at Soufrière Hills Volcano, Montserrat: 1995–2009, *Geophysical Research Letters*, *37*(19).

Wadge, G., B. Voight, R. Sparks, P. Cole, S. Loughlin, and R. Robertson (2014), An overview of the eruption of Soufrière Hills Volcano, Montserrat from 2000 to 2010, *Geological Society, London, Memoirs*, *39*(1), 1–40.

Young, S. R., R. S. J. Sparks, W. P. Aspinall, L. L. Lynch, A. D. Miller, R. E. Robertson, and J. B. Shepherd (1998), Overview of the eruption of Soufriere Hills volcano, Montserrat, 18 July 1995 to December 1997, *Geophysical Research Letters*, *25*(18), 3389–3392.

Zhang, Y., Z. Xu, M. Zhu, and H. Wang (2007), Silicate melt properties and volcanic eruptions, *Reviews of Geophysics*, *45*(4).

Chapter 5

Discussion and summary

In this chapter, I firstly discuss the limitations of, and assumptions made in, the modelling throughout this thesis (Section 5.1). Secondly, the key outcomes of the thesis are summarised (Section 5.2), before I discuss the broader implications of this work (Section 5.3). Finally, I outline what future work could be done to build upon the progress I have made (Section 5.6).

5.1 Limitations and assumptions

All numerical models attempt to simulate one or several aspects of a real system and, therefore, are limited by simplifications and assumptions that must be acknowledged and understood. The greater the number of variables included in a model, the greater the uncertainty in the solution. Therefore, where available, previous work must be used to determine which physical phenomena should be considered and which can be neglected. Scientific research is often progressed by challenging whether commonly accepted assumptions are justified. In this section, I firstly in discuss the sensitivity of my results to changes in key parameters in Section 5.1.1. In Section 5.1.2 I then discuss more broadly what effect incorporating factors or processes not currently considered in my modelling may have, and by doing so introduce potential opportunities for future research.

5.1.1 Sensitivity to changes in key parameters

A major strength of numerical modelling is in quantifying the sensitivity of a process to changes in key parameters. A number of key parameters that control magma ascent and deformation remain poorly constrained, and so it is difficult to assign appropriate values to model parameters. Therefore, when interpretting model results, one must consider that similar solutions can be obtained using different model setups due to trade-offs that exist between key parameters.

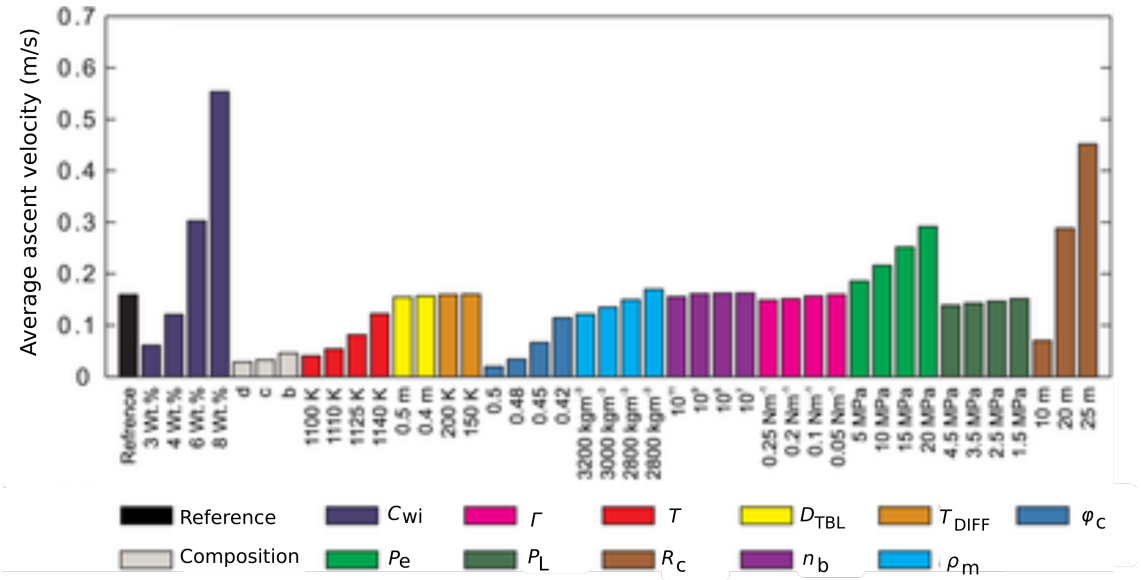

Figure 5.1: Sensitivity of ascent velocity through a volcanic conduit to several key parameters, where a single parameter is varied from a reference flow model. Edited from *Thomas and Neuberg* (2014).

Thomas and Neuberg (2014) analysed the sensitivity of ascent velocity through a volcanic conduit to several key parameters (Figure 5.1), including the composition of the melt, the initial dissolved H_2O content, C_{wi}, excess pressure at the base of the conduit, P_e, bubble surface tension, Γ, temperature, T, loading pressure at the top of the conduit, P_L, conduit radius, R_c, thickness of the thermal boundary layer, D_{TBL}, bubble number density, n_b, temperature difference within the thermal boundary layer, T_{DIFF}, melt density, ρ_m, and crystal content, ϕ_c. Factors such as the temperature, composition and crystal content influence the bulk viscosity of the magma (*Giordano et al.*, 2008, *Maron and Pierce*, 1956), and therefore the ascent velocity. To investigate how changes in the bulk viscosity influence the shear stress exerted at the conduit wall, I have multipled the visocisty profile in the reference flow model of Chapter 2 (Figure 2.4, before scaling discussed in Section 2.2.1) by a suite of constant values (Figure 5.2). Due to a trade-off between ascent velocity and bulk viscosity (Eq. 2.1), similar shear stress and overpressure profiles are modelled at the conduit wall in each case. One should note that this is a simplification, and does not consider nonlinear controls of crystallisation and gas loss on bulk viscosity and ascent velocity (*Melnik and Sparks*, 1999), for example. Spatial variations in the viscosity, as a result of such as crystallisation and gas loss towards the surface, have a more significant influence on shear stress and overpressure (Figure 4.4). In Figure 4.7 I show how ascent dynamics and dome growth are influenced by the rates of crystallisation and gas loss.

Thomas and Neuberg (2014) also identified the driving pressure gradient, radius of the conduit, and the initial dissolved H_2O content as factors in governing magma ascent velocity. In Figure 2.7s, I present the sensitivity of the shear stress, overpressure and

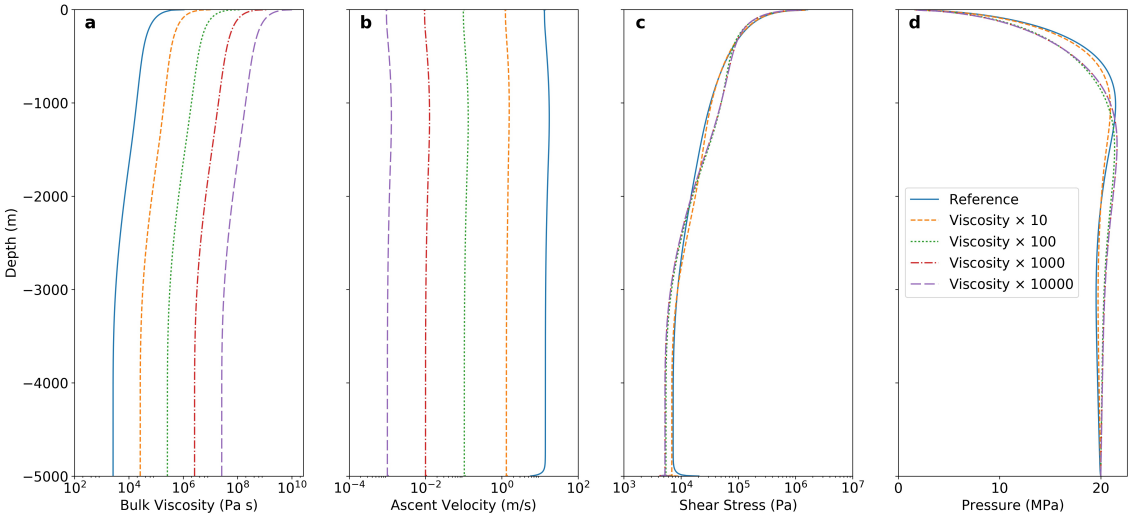

Figure 5.2: **a**) Bulk viscosity at the centre of the conduit, from multiplying the reference viscosity profile (Figure 2.2.4) by a constant. **b**) The resultant changes in ascent velocity at the conduit centre and **c**) shear stress at the conduit wall. Note that similar shear stress profiles are obtained in each case.

modelled tilt to changes in the driving pressure gradient and initial volatile content of the melt. In Figure 4.7 I show these factors influence the maximum height a dome can grow to. The radius of the conduit is poorly constrained, particularly at depth, since it cannot be directly measured using even modern methods. *Thomas and Neuberg* (2014) showed that magma ascends 5 times faster through a conduit with a radius of 25 m compared to a conduit with a radius of 10 m as used in Chapter 2. I speculate that since the difference in bulk viscosity would be less significant, the shear stress could also be approximately 5 times higher than obtained in Chapter 2 in this case. An increase in the conduit radius would also increase the maximum height that a dome could grow to, because an increase in ascent velocity provides less time for crystallisation (Eq. 4.3).

In Chapter 2, a simple 2D axisymmetric edifice with a constant slope is used to represent Tungurahua volcano, where RETU is at approximately the correct horizontal and vertical distance from the top of the conduit. However, in Chapter 3 the topographic effect on tilt is shown to be potentially significant. Table 5.1 shows the tilt produced by either shear stress or overpressure, and compares results where either the 2D axisymmetric model in Chapter 2 or the 3D model in Chapter 3 is used, where topography is the only difference. The relative contribution of shear stress and overpressure to the tilt at RETU is similar when topography is accounted for, although the contribution of shear stress is still greater than that of overpressure.

Whilst in Chapters 2, 3 and 4 I show how varying a single parameter in turn can influence my results, the combined effect of varying multiple parameters could be much more significant. For example, if the driving pressure gradient, volatile content and radius of the conduit are all greater than the values used in my reference model, shear

	2D	3D
Shear stress	67 µrad	79 µrad
Overpressure	24 µrad	67 µrad

Table 5.1: Modelled tilt at RETU, from the 2D axisymmetric modelling in Chapter 2 and the 3D modelling in Chapter 3. The deformation modulus of the edifice is equal to 10 MPa in each case.

stress and overpressure in the conduit would be much greater (Figure 2.7). This would have implications for the value of the deformation modulus required (Figure 2.6) to model a tilt of 170 µrad as observed at RETU (Figure 2.2). If the rate of crystallisation at SHV is higher than assumed in my reference model in Chapter 4 (Figure 4.7a), for a dome to grow to the height of 400-500 m as observed, the conduit radius, excess pressure at depth (Figure 4.7b) and/or the initial volatile content of the magma (Figure 4.7c) would have to be higher. Alternatively, the rate of gas loss from the conduit may have been slower than assumed (Figure 4.7d).

5.1.2 Factors not considered

Deviations from a cylindrical conduit

Conduits are typically modelled as being cylindrical and vertical, supported by observations of the geometry of extruded lava spines (*Voight et al.*, 1999) or exposed, vacated conduits (*Johnson et al.*, 2018). A circular cross-section is also the most stable geometry as stresses at any depth are constant around the circumference of the conduit. Deviations from a cylindrical geometry would influence the magma ascent dynamics, and hence the shear stress, overpressure, and the induced deformation and seismicity. Conduits in some cases may be elliptical, with the alignment dictated by the orientation of the regional stress field. One would expect the shear stress exerted on the walls at opposing ends of the minor axis to be greater than on the walls at opposing ends of the major axis, as shear stress is inversely proportional to the radius (Equation 1.10). This would yield an asymmetric deformation pattern at the surface. At depth, conduits transition into elongate dykes (*Eichelberger et al.*, 1986, *Costa et al.*, 2007) or shallow magma reservoirs (*Cashman et al.*, 2017). However, it is generally unclear how deep conduits extend. This influences the buoyancy of the magma column, which is driven upwards by less dense, bubbly magma closer to the surface, and weighed down by relatively denser magma at depth.

Volcanic conduits can be widened through time due to pressure-driven elastic deformation, and erosion due to shear stress (*Aravena et al.*, 2017). *Aravena et al.* (2018) modelled an upwards widening of the conduit, since shear stress increases towards the surface (Figure 2.4). Magma ascends faster through wider conduits, and thus exerts more shear stress on the conduit walls. Shear stress can be amplified locally by where the conduit geometry changes with depth (*Thomas and Neuberg*, 2012). This explains

how low-frequency seismicity can be triggered at depth of a few kilometres, where the shear stress would otherwise be far lower than the shear strength of the magma (Figure 2.4). How changes in conduit geometry with depth influence ascent dynamics and deformation induced is yet to be fully explored.

Variations in magma temperature

Magma with a higher temperature has a lower viscosity (*Giordano et al.*, 2008), and so spatial or temporal variations in the temperature can influence ascent dynamics. Heat loss due to conduction is negligible over time-scales of an eruption (*Mastin*, 2005), and in Chapter 2 I show that shear stress exerted on the conduit walls is insensitive to the presence of a thermal boundary layer. The release of latent heat during crystallisation can cause magma to increase in temperature by up to 100 °C in the upper few kilometres of the conduit (*Blundy et al.*, 2006, *Hale et al.*, 2007). Additionally, shear heating that results from viscous dissipation can significantly influence ascent dynamics over relatively short time-scales (*Mastin*, 2005, *Hale et al.*, 2007).

The temperature change due to shear heating through time, dT/dt, can be given as

$$\frac{dT}{dt} = \frac{1}{\rho_\mathrm{b} c_\mathrm{p}} \left\{ \sigma_\mathrm{s} \frac{dv_\mathrm{z}}{dr} \right\}, \tag{5.1}$$

a function of the shear stress, σ_s, strain rate, dv_z/dr, bulk density, ρ_b, and specific heat capacity, c_p (*Bird et al.*, 2002). Shear heating is more significant towards the conduit boundary, where dv_z/dr, and consequently σ_s (Eq. 1.3) are greater. The bulk viscosity, η_b, is smaller where the temperature is higher (*Giordano et al.*, 2008), hence magma towards the conduit wall will accelerate due to shear heating, in turn causing strain rate to increase. A positive feedback loop between strain rate, viscosity and temperature may lead to a runaway effect that has been hypothesised to potentially play an important role in ascent dynamics (*Mastin*, 2005, *Wright and Weinberg*, 2009). Magma towards the conduit walls accelerates, producing a plug-shaped velocity profile (*Mastin*, 2005). It is unclear whether shear stress, which is proportional to both the strain rate and viscosity (Eq. 1.3), would increase or decrease as a consequence of shear heating.

Solidification of magma

Due to crystallisation and the exsolution of volatiles from the melt, the viscosity of magma increases by several orders of magnitude as it ascends (Figure 4.4). This can culminate in the solidification of magma in the upper conduit, forming a plug (*Hall et al.*, 2015), the ascent of which cannot be simulated through viscous flow modelling alone. How deep this solidification extends into the conduit is not well known. As a plug forms, ascending magma below it decelerates (*Albino et al.*, 2011), and pressurises. Modelling magma only as a fluid, if ascent ceases no shear stress would be exerted on the

conduit walls (Equation 1.3). However, if magma has solidified in the upper conduit, shear stress is still exerted as forces driving ascent work against friction at the conduit walls (*Iverson et al.*, 2006), producing near-field deformation.

Unerupted magma

The amount of gas emitted from a volcano often exceeds the amount that can be dissolved in estimated volumes of erupted magma alone (*Edmonds et al.*, 2010). Additionally, volcanic edifices are thought to grow quicker than can be explained through only exogenous growth (*Annen et al.*, 2001). Endogenous growth through the intrusion of magma is thought to be significant. In more silicic systems, underplating of unerupted mafic magma has been suggested as a potential source of excess gas (*Edmonds et al.*, 2010).

Excess gas in the system from unerupted magma would increase the gas volume fraction and consequently the buoyancy of the magma column. However, given the potentially greater uncertainty in how much gas escapes from the system (Section A.4), excess gas is justifiably neglected throughout this thesis. In basaltic systems, the presence of excess gas can be partially explained by convection of magma in the conduit (*Kazahaya et al.*, 1994). Buoyant, gas-rich magma ascends and degasses, and consequently increases in density and sinks. However, convection of highly viscous magma is only possible where the conduit radius is large. Modelling by *Kazahaya et al.* (2002) suggested that a radius of 25 m is necessary for flow to be sufficiently fast for effective convection of rhyolitic magma, hence convection is neglected in this study.

Overpressure in the upper conduit can exceed the tensile strength of the edifice, causing the edifice to fracture, potentially leading to the formation of lateral intrusions (*Sparks*, 1997). If the fractured region is fluid saturated, the radius of the overpressured region could exceed that of the conduit (*Widiwijayanti et al.*, 2005). However, one would expect the overpressure to decrease as a result (*Collinson and Neuberg*, 2012). It is unclear how this would influence the contribution of overpressure to the deformation, as a trade-off exists between source radius and pressure (*Mogi*, 1958), nor how such a process would affect ascent dynamics.

Mechanical properties of the edifice

Throughout my deformation modelling, I assume that the edifice is homogeneous, and use constant values for the density, deformation modulus and Poisson's ratio. In reality, volcanic edifices are formed from the diverse deposits of numerous eruptions. It is unrealistic to expect to determine single values for the mechanical properties that are representative of the entire edifice. As discussed in Section 2.3, edifices can be heavily fractured, chemically altered, and poorly consolidated, and can therefore be much weaker than intact rocks, particularly on the scale of an edifice. To account for this

uncertainty, in Chapter 2 results are presented for a suite of deformation moduli. In Chapter 3, I normalise my results by the equivalent value produced when using a simplified or analytical model, and therefore the results are insensitive to the mechanical properties of the edifice used in the modelling.

The mechanical properties of a volcanic edifice vary spatially, influenced by variations in such factors as rock-type (*Bass*, 1995, *Heap et al.*, 2019), pressure and temperature (*Del Negro et al.*, 2009), porosity (*Heap et al.*, 2019), water-saturation (*Castagna et al.*, 2018, *Heap et al.*, 2018), the fracture network (*Heap et al.*, 2014) and chemical alteration (*Pola et al.*, 2014). Modelling by *Hickey et al.* (2013) showed that this variability can influence the spatial deformation pattern. However, it was not necessary to consider spatial variations in the mechanical properties of the edifice in Chapter 2, since spatial variations in deformation are not the focus of this chapter. Furthermore, the uncertainty in the absolute value of the deformation modulus is significant, as discussed in Section 2.3. In Chapter 3, to isolate the influence of topography on tilt, constant values were used for the mechanical properties of the edifice. However, it may be insightful to investigate how spatial variations in the mechanical properties affect tilt, particularly if considered in conjunction with topographic effects.

5.2 Summary of key outcomes

In Chapter 2, combined numerical modelling of magma ascent and deformation was used to quantify the relative contribution of shear stress and overpressure to changes in tilt recorded close to the conduit. Whilst shear stress produced as magma ascends is, at most depths, orders of magnitude smaller than overpressure, shear stress generally contributes more to the tilt. In Chapter 3, I showed that the tilt recorded can be significantly influenced by topography. Topography can amplify, reduce, or reverse the polarity of the tilt. To quantitatively link changes in tilt to changes in source stress, forward modelling is hence often preferential over analytical methods to match observations. Such modelling requires a DEM and a starting model of the source geometry as well as mechanical properties of the edifice. In Chapter 4, I showed the growth of a lava dome above the conduit vent can impede ascent, and even cause it to stall. Shear stress changes most significantly as a lava dome approaches its critical height, whilst changes in overpressure are more pronounced during earlier stages of dome growth. Subsidence resulting from the increasing weight of the dome can mask deformation induced by changes in shear stress or overpressure (*Odbert et al.*, 2015). Hence changes in tilt recorded by any single tiltmeter may be driven by different sources as activity evolves at a volcano.

5.3 Broader implications

The work in this thesis sheds light on some of the key factors that govern magma ascent and the deformation induced. This work is particularly relevant to volcanologists interpretting tilt data recorded close to a volcanic conduit. An increase in the radial tilt is often assumed to be driven by an increase in pressure in the upper edifice (e.g. *Medina et al.*, 2017). However, in Chapter 2 I have shown that the contribution of shear stress must be considered as an important deformation source. I have presented key factors that can drive changes in ascent dynamics, shear stress, overpressure and therefore tilt through time, that volcanologists can consider when interpretting their data. This includes 1) shear stress and pressure being progressively exerted on a greater proportion of the conduit as magma refills the conduit (Section 2.5) 2) changes in the driving pressure gradient (Figures 2.7 & 4.4), 3) changes in the volatile content (Figure 2.7), 4) changes in the radius of the conduit (Section 5.1.1), 5) changes in how much gas can escape from the conduit (Figure 4.7d).

In Chapter 3, I have shown that due to the influence of topography, the maximum tilt is often not radial to the source (Figure 3.9). In some cases, negative radial tilt can be produced by an increase in pressure (Figure 3.9). Therefore, where possible, numerical modelling including a DEM to represent the topography of the volcano and a best guess of the deformation source should be attempted to aid interpretation. Geodetic data from multiple stations should be considered where possible (*Johnson et al.*, 2019).

Considering changes in tilt alongside data collected using other monitoring techniques may help one to constrain how a volcanic system is evolving through time. For example, it is often difficult to distinguish whether an increase in gas flux at a volcano is the result of an injection of volatiles into the system or an increase in the permeability of the system allowing more gas to escape (*Edmonds et al.*, 2003). These two processes yield opposing changes in the gas volume fraction, and therefore the buoyancy and ascent rate of the magma (Figure 4.7). Therefore, if one could identify that a change in tilt is predominantly controlled by changes in shear stress, linked to ascent velocity (Eq. 2.1), I speculate that one may be able to more easily distinguish what has caused the gas flux to increase. The total shear stress partitions between inducing deformation and generating low-frequency seismicity (*Neuberg et al.*, 2018). Hence, to fully understand and quantify changes in magma ascent dynamics, deformation and low-frequency seismicity must be considered simultaneously.

5.4 A link to seismicity

It is often logistically difficult to deploy tiltmeters close to the conduit of steep-sided silicic volcanoes. Hence, a negative correlation between low-frequency seismicity and

tilt, such as observed at Tungurahua (Figure 5.3) and SHV (Figure 1.4), is seldom observed, and has not been extensively explored. These data provided an opportunity to further investigate what drives this negative correlation. A number of models can conceptually explain why tilt decreases and low-frequency seismicity increases leading up to a Vulcanian explosion, as observed at Tungurahua, including;

1. The solidification of a viscous plug and/or the growth of a lava dome impedes magma ascent, causing shear stress to decrease, until ascent stalls (Chapter 4). Ascent recommences when the overpressure from the underlying magma overcomes friction at the conduit wall and is sufficient to fracture and displace dome rock. Ascent causes the overpressure to reduce until magma stalls again. Incremental stick-slip magma ascent triggers low-frequency seismicity at each slip event (*Iverson et al.*, 2006).

2. If shear stress exceeds the shear strength of the magma, τ_{m}, magma fails in a brittle manner (*Goto*, 1999, *Tuffen et al.*, 2003), triggering low-frequency seismicity (*Neuberg et al.*, 2006). The shear stress exerted at the conduit walls decreases as a result. The total shear stress is partitioned between deformation and seismicity, and therefore tilt decreases following the onset of seismicity (*Neuberg et al.*, 2018).

3. Brittle failure of magma generates fractures. Frictional heating along these fractures leads to a decrease in magma viscosity towards the conduit margins (*Kendrick et al.*, 2014), potentially causing the magma column to accelerate into a plug-like velocity profile without transferring shear stress across the conduit wall.

5.5 Discerning between conceptual models

With numerous conceptual models capable of explaining a negative correlation between low-frequency seismicity and tilt, different models may be applicable in different scenarios. A negative correlation between tilt and seismicity could be interpreted as being indicative of either an acceleration or deceleration of the ascending magma depending on the model assumed. This makes the interpretation of monitoring data challenging, and additional information is required to discern between models. In extrusive eruptions, the ascent rate may be able to be directly measured (*Wadge et al.*, 2010). Alternatively, changes in ascent velocity can be indirectly inferred. One would expect ascent rate to increase following injection of volatiles into the system (Figure 5.1), which could be inferred from an increase in gas flux measured at the surface. Broader inflation of the edifice could be the result of pressurisation of a shallow magma reservoir (*Mogi*, 1958), which also facilitates magma ascent (Figure 5.1).

There are key differences between the volcanic activity Tungurahua (Figure 5.3), and the activity at SHV that accompanied a negative correlation between seismicity

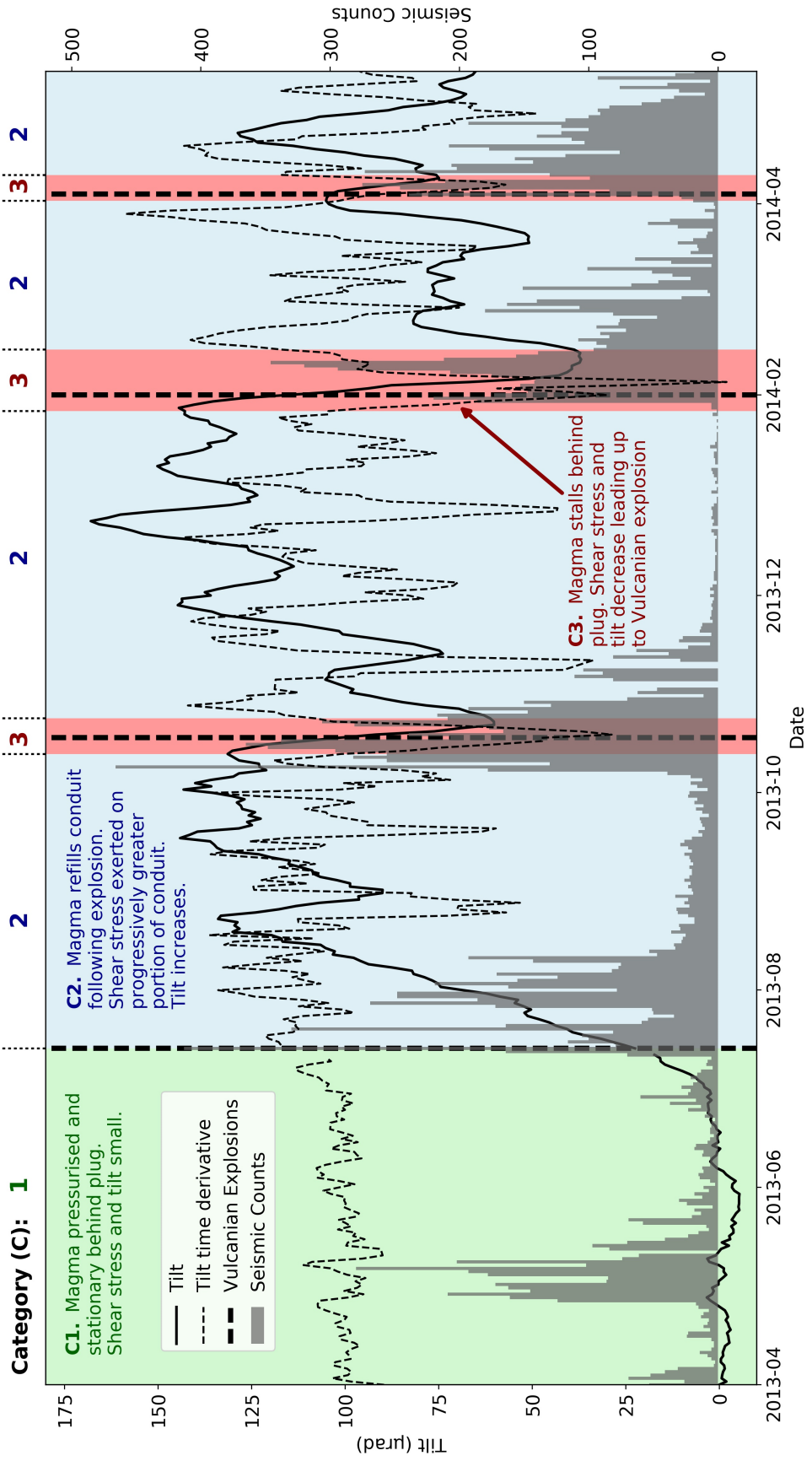

Figure 5.3: Daily averaged tilt, its time derivative, and low-frequency seismic earthquake count recorded at RETU, Tungurahua. The data is divided into 3 categories (C1, C2 and C3), based on interpretations as described in Section 5.5, annotated in green, blue and red respectively and labelled above the axis.

and tilt (Figure 1.4). Since 1995, activity at SHV has comprised numerous periods of dome growth and collapse. In 1997, 8-22 hour cycles of seismicity and tilt coincided with particularly rapid extrusion and periods of dome instability (*Green et al.*, 2006). A lava dome has not been observed at Tungurahua since activity recommenced in 1999. Instead, cycles of seismicity and tilt in 2013-4 begin and end with Vulcanian explosions approximately 3 months apart, separated by months of quiescence (Figure 5.3). I therefore speculate that fundamentally different processes drove the cyclic behaviour at the two volcanoes.

At SHV, low-frequency seismicity begins and ceases at inflection points in the tilt cycle (Figure 1.4), at depths of a few kilometres where magma is in a state of glass-transition (*Neuberg et al.*, 2006). This is consistent with the model that shear stress is partitioned between seismicity and deformation, where tilt decreases coincident with, or following, the onset of seismicity. Stick-slip motion of a plug is likely to occur only in the upper few hundred metres of the conduit (*Iverson et al.*, 2006). The source depth of low-frequency seismicity is poorly constrained at Tungurahua, since most low-frequency earthquakes are only clearly observed at RETU (*Bell et al.*, 2018). It can therefore not be used to discern between conceptual models in this case.

Prior to the Vulcanian explosion on February 1st 2014, a decrease in tilt precedes the onset of seismicity (Figure 1.6), which is difficult to explain using the shear stress partitioning model. Considering this model, one may expect the change in tilt to be greater if the timing between successive low-frequency events is shorter, or if they are larger in magnitude. However, there is no clear correlation between larger increases in the cumulative seismic energy and more significant decreases in tilt.

The Vulcanian explosion in July 2013 at Tungurahua was associated with an increase in both tilt and low-frequency seismicity, hence a positive correlation (Figure 5.3). This eruption was preceded by a power-law increase in the number of low-frequency events (*Bell et al.*, 2018) (Figure 5.4), distinguishing it further from the latter 3 Vulcanian explosions. The material failure law dictates that the *failure* time (in this case the time of eruption) can be predicted as the time when the rate of increase of an observable quantity, such as deformation or number of low-frequency earthquakes, reaches infinity (*Voight*, 1988). This is equivalent to where the inverse rate reaches zero. In Section 2.4, I speculate that stalled magma pressurised behind a tightly-sealed plug prior to the July 2013 explosion, exerting no shear stress on the conduit wall (Figure 5.3, C1). The decrease in the time interval between successive low-frequency earthquakes could be caused by pressure building below the plug, hence the plug is incrementally pushed up at progressively shorter time intervals. This pressurisation culminates in the explosion. Refilling of the conduit following the July 2013 explosion causes shear stress to be exerted on a greater proportion of the conduit wall, hence tilt increases (Figure 5.3, C2). As magma approaches the surface, decompression-induced crystallisation causes ascent rate to decrease (Figure 4.4), leading to the solidification of a viscous plug (*Hall*

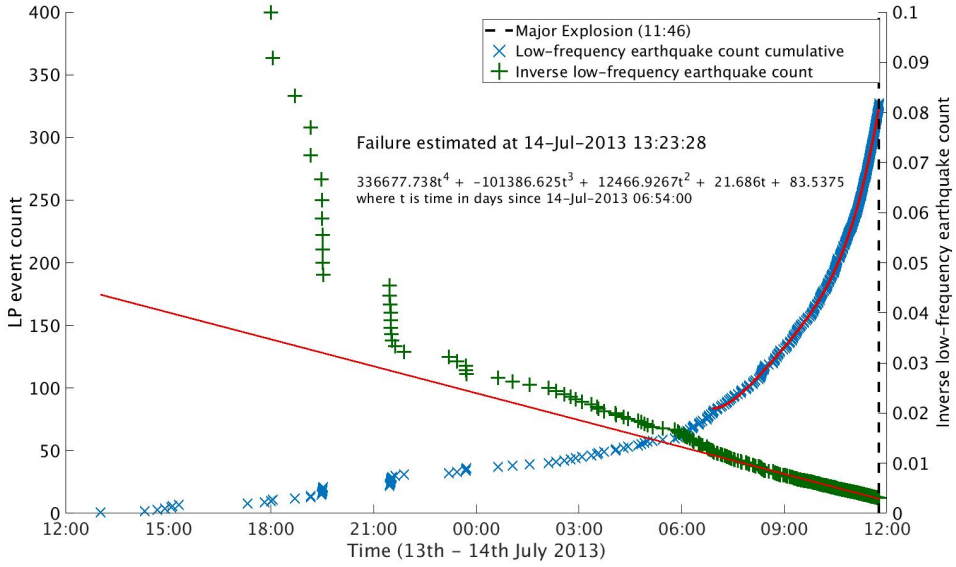

Figure 5.4: Power-law increase in the number of low-frequency earthquakes 24 hours leading up to a Vulcanian explosion at 11:46 UTC on 14th July 2013 at Tungurahua volcano. Earthquakes detected at RETU. Failure estimated as the time where the inverse of the low-frequency earthquake count, if continued, is predicted to reach zero.

et al., 2015), potentially explaining why tilt decreases prior to the next Vulcanian explosion (Figure 5.3).

Each Vulcanian explosion in the sequence may have been the culmination of pressurisation behind solid plugs (*Hall et al.*, 2015). However, the polarity of the tilt changes leading up to each explosion varies. Therefore, similar eruptive activity observed at the surface can be preceded by either a positive or negative correlation between seismicity and tilt, depending on how magma ascent dynamics evolve through time leading up to it. The polarity of the tilt, and therefore how it correlates with seismicity, also depends on both topography and the location of the tiltmeter with respect to the conduit (Chapter 3).

5.6 Future work

5.6.1 What could be achieved with more data?

With data from more silicic volcanoes, one could assess how low-frequency seismicity correlates with deformation in different systems, associated with different types of volcanic activity. Our modelling in Chapter 2 is constrained using data from only one tiltmeter at Tungurahua, RETU. Other tiltmeters deployed at a greater distance from the conduit are not sensitive to changes in ascent dynamics (*Neuberg et al.*, 2018), and a complimentary correlation with the data is not observed in the GPS data recorded at RETU (Figure 5.5). This is perhaps due to the higher sensitivity of a tiltmeter

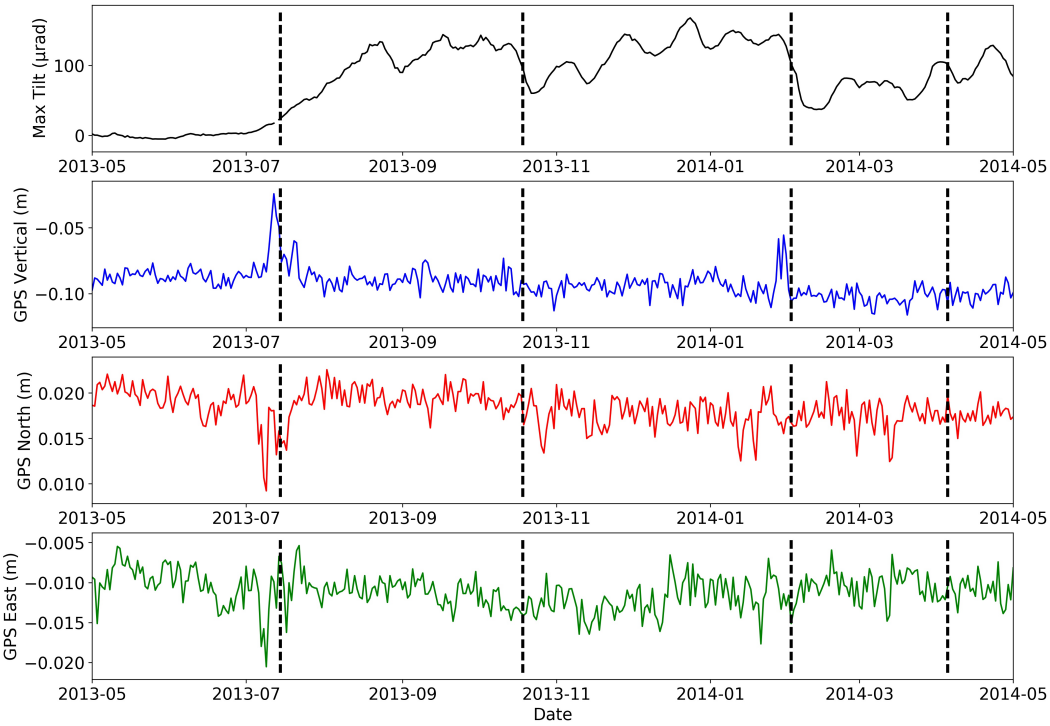

Figure 5.5: Maximum tilt and GPS data (vertical, north and east) recorded at RETU, Tungurahua. The timing of Vulcanian explosions is plotted using dashed black lines.

relative to GPS. Also, it should be noted that tiltmeters measure flank rotation, and the same tilt can be produced alongside uplift, subsidence, or no displacement at the same location.

Even a single strategically deployed tiltmeter was shown to be invaluable at forecasting that an eruption was imminent at Tungurahua in February 2014 (*Mothes et al.*, 2015). Nevertheless, care must be taken when constraining a model using a single data source. Similar tilt variations associated with eruptive activity, recorded in close proximity to the conduit, have been recorded at a number of silicic volcanoes, including Soufrière Hills volcano, Montserrat (SHV) (*Voight et al.*, 1998), Mount St. Helens, USA (*Anderson et al.*, 2010), Volcán de Colima, Mexico (*Zobin et al.*, 2007), and Galeras volcano, Colombia (*Medina et al.*, 2017). Therefore, near-field deformation such as recorded at RETU is not uncommon, and Chapter 2 provides insight more generally into what drives this.

Deploying tiltmeters close to the conduit at more silicic volcanoes would be beneficial. Other instrumentation should also be considered, and with improvements in the return period of InSAR satellites, monthly or even weekly deformation cycles such as seen at Tungurahua should now be detectable. My modelling suggests that for 170 µrad as observed at RETU (Figure 5.3) to be induced solely by shear stress, the summit should be uplifted by around a metre (Figure 5.6), which should be easily detectable using InSAR methodology. Furthermore, the spatial deformation pattern

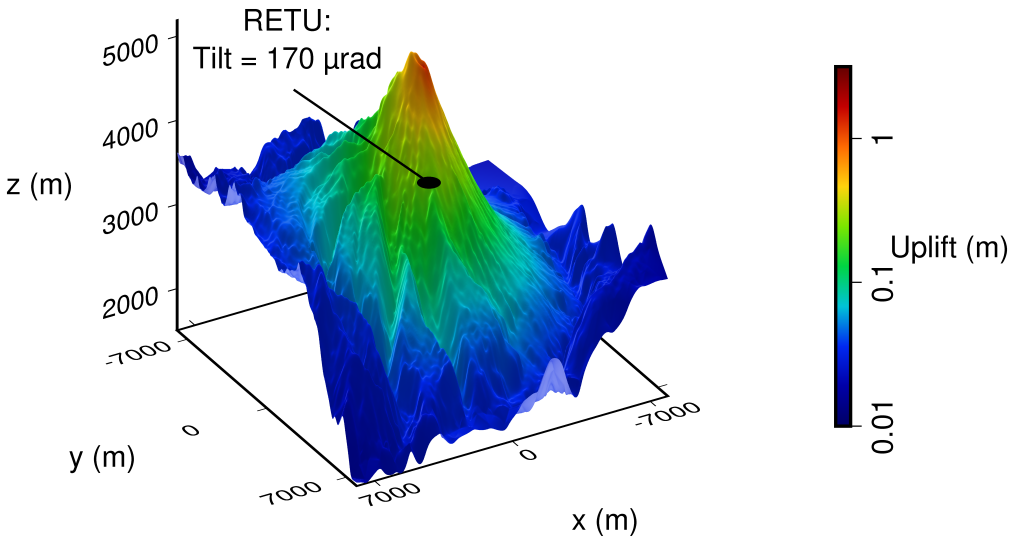

Figure 5.6: Uplift produced by only shear stress obtained from the reference flow model in Chapter 2 (Figure 2.4), using a 3D deformation including a 10 x 10 m DEM of Tungurahua volcano. A deformation modulus of 8.6 MPa has been applied, so that a tilt of 170 µrad is recorded at the location of RETU, as observed (Figure 5.3). Note that around a metre of uplift is modelled close to the summit.

produced by shear stress would differ significantly from that produced by overpressure, hence an enhanced spatial resolution would allow one to more easily quantify the relative contribution of the two sources. Nonaxisymmetric deformation could be produced if either the geometry of the conduit is more complex (Section 5.1.2), or if the mechanical properties of the edifice vary spatially, for example (Section 5.1.2).

5.6.2 Modelling the interaction between volcanic conduits and shallow magma reservoirs

InSAR methodology has been successfully used to infer changes in pressure or volume of shallow magma reservoirs (*Galetto et al.*, 2018, *Muller et al.*, 2018). Such deformation has a much broader wavelength than near-field deformation from changes in shear stress or overpressure in the conduit. Deformation from different sources can be superimposed on each other, and modelling can be used to isolate the relative contribution of each source. In Chapter 2, I showed that an increase in reservoir pressure causes shear stress and overpressure in the conduit to increase (Figure 2.7a-c). This would produce both near-field deformation due to changes in ascent dynamics, and broader deformation resulting from the pressurisation of the reservoir (Figure 5.7a). Alternatively, I showed that an increase shear stress, overpressure in the conduit and near-field deformation can be driven by an increase in the volatile content (Figure 2.7d-f), which may not necessarily coincide with an increase in reservoir pressure (Figure 5.7b). One can postulate that there are also scenarios that would lead to an increase in near-field

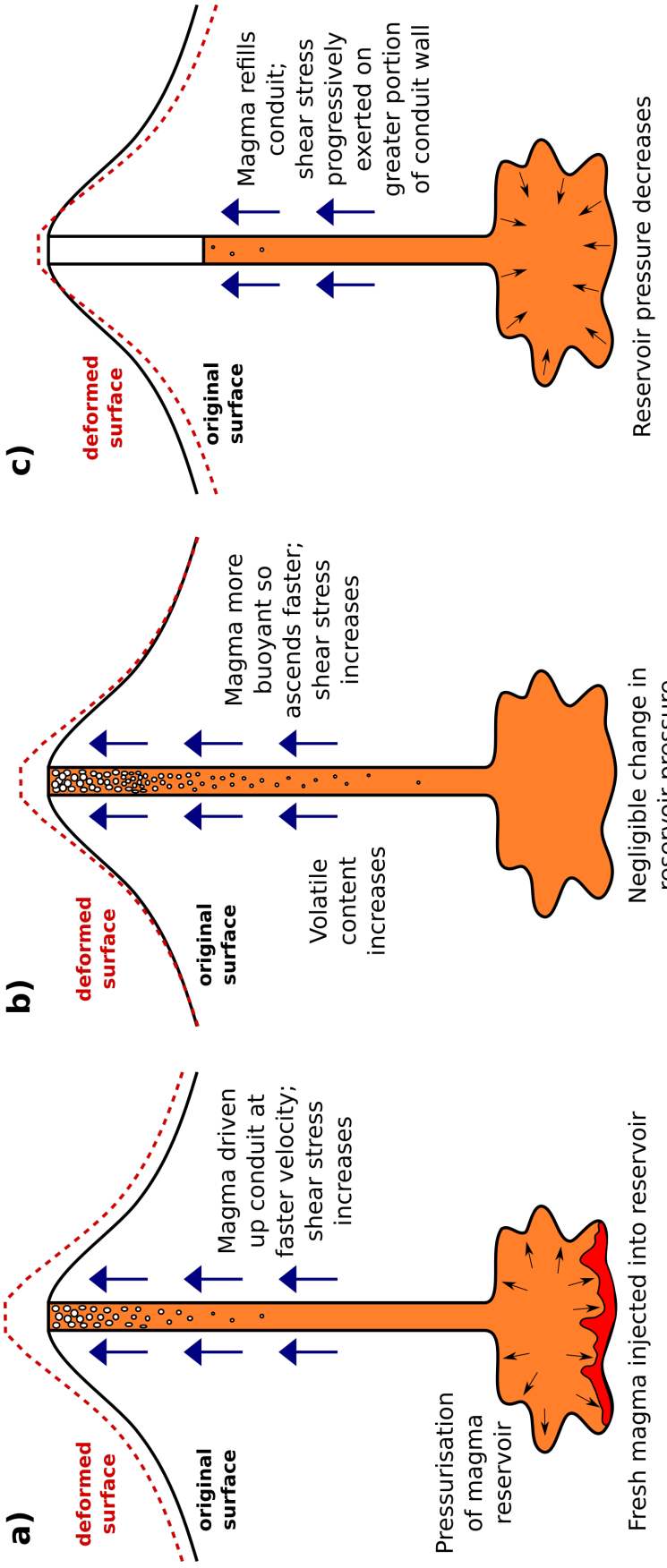

Figure 5.7: Examples of how an increase in tilt recorded close to the conduit can coincide with either a) an increase in pressure, b) undetectable change in pressure, or c) a decrease in pressure, of a shallow magma reservoir.

deformation driven by shear stress or overpressure, but a decrease in deformation driven by reservoir pressure. For example, magma vacating the reservoir as the conduit is refilled would cause an increase in near-field deformation driven by shear stress being progressively exerted on a greater portion of the conduit, whilst the magma reservoir depressurises (Figure 5.7c). An increased spatial resolution gained through InSAR could be used to distinguish between these scenarios, and provide insight into the lag time between changes in shallow magma reservoirs and ascent dynamics in the conduit, potentially allowing one to constrain the velocity at which magma ascends.

5.6.3 Towards a quantitative model

To move from conceptual to quantitative models that explain the correlation between seismicity and tilt, further investigations must be performed to derive quantitative relationships for various important volcanic processes, such as:

- How much shear stress reduction is achieved in a seismic swarm?
- How long does it take fractures to reseal and for magma to recover its shear strength?
- How does frictional heating influence the rheology?

A suitable seismic array is also required, that enables one to accurately determine the magnitude and location of each low-frequency earthquake. Non-planar fracture geometries should be considered in calculating the magnitude of an event, as a partial-ring geometry may be more appropriate than planar faults for brittle failure of magma in a cylindrical conduit (*Contreras-Arratia and Neuberg*, 2019). Quantitative relationships can be incorporated into combined time-dependent flow and deformation models, and one could model how the tilt changes through time following the onset of seismicity. This could allow one to discern between the various conceptual models, and retrospectively quantify how the magma ascent rate changed through time. This could ultimately lead to the development of a combined forecasting tool in the future, that considers both low-frequency seismicity and deformation.

References

Albino, F., V. Pinel, H. Massol, and M. Collombet (2011), Conditions for detection of ground deformation induced by conduit flow and evolution, *Journal of Geophysical Research: Solid Earth*, *116*(B6).

Anderson, K., M. Lisowski, and P. Segall (2010), Cyclic ground tilt associated with the 2004–2008 eruption of Mount St. Helens, *Journal of Geophysical Research: Solid Earth*, *115*(B11).

Annen, C., J.-F. Lénat, and A. Provost (2001), The long-term growth of volcanic edifices: numerical modelling of the role of dyke intrusion and lava-flow emplacement, *Journal of Volcanology and Geothermal Research*, *105*(4), 263–289.

Aravena, Á., M. d. Vitturi, R. Cioni, and A. Neri (2017), Stability of volcanic conduits during explosive eruptions, *Journal of Volcanology and Geothermal Research*, *339*, 52–62.

Aravena, A., R. Cioni, M. de Michieli Vitturi, M. Pistolesi, M. Ripepe, and A. Neri (2018), Evolution of conduit geometry and eruptive parameters during effusive events, *Geophysical Research Letters*, *45*(15), 7471–7480.

Bass, J. D. (1995), Elasticity of minerals, glasses, and melts, *Mineral physics and crystallography: A handbook of physical constants*, *2*, 45–63.

Bell, A. F., M. Naylor, S. Hernandez, I. G. Main, H. Elizabeth Gaunt, P. Mothes, and M. Ruiz (2018), Volcanic eruption forecasts from accelerating rates of drumbeat long-period earthquakes, *Geophysical Research Letters*.

Bird, R. B., W. E. Stewart, and E. N. Lightfoot (2002), Transport Phenomena 2ndEd, *John Wiley & Sons, New York*, *63*, b21.

Blundy, J., K. Cashman, and M. Humphreys (2006), Magma heating by decompression-driven crystallization beneath andesite volcanoes, *Nature*, *443*(7107), 76.

Cashman, K. V., R. S. J. Sparks, and J. D. Blundy (2017), Vertically extensive and unstable magmatic systems: a unified view of igneous processes, *Science*, *355*(6331), eaag3055.

Castagna, A., A. Ougier-Simonin, P. Benson, J. Browning, R. J. Walker, M. Fazio, and S. Vinciguerra (2018), Thermal damage and pore pressure effects of the brittle-ductile transition in comiso limestone, *Journal of Geophysical Research: Solid Earth*, *123*(9), 7644–7660.

Collinson, A., and J. Neuberg (2012), Gas storage, transport and pressure changes in an evolving permeable volcanic edifice, *Journal of Volcanology and Geothermal Research*, *243*, 1–13.

Contreras-Arratia, R., and J. W. Neuberg (2019), Complex seismic sources in volcanic environments: Radiation modelling and moment tensor inversions, *Journal of Volcanology and Geothermal Research*.

Costa, A., O. Melnik, R. Sparks, and B. Voight (2007), Control of magma flow in dykes on cyclic lava dome extrusion, *Geophysical Research Letters*, *34*(2).

Del Negro, C., G. Currenti, and D. Scandura (2009), Temperature-dependent viscoelastic modeling of ground deformation: application to etna volcano during the 1993–1997 inflation period, *Physics of the Earth and Planetary Interiors*, *172*(3-4), 299–309.

Edmonds, M., C. Oppenheimer, D. M. Pyle, R. A. Herd, and G. Thompson (2003), So2 emissions from soufrière hills volcano and their relationship to conduit permeability, hydrothermal interaction and degassing regime, *Journal of Volcanology and Geothermal Research*, *124*(1-2), 23–43.

Edmonds, M., A. Aiuppa, M. Humphreys, R. Moretti, G. Giudice, R. Martin, R. Herd, and T. Christopher (2010), Excess volatiles supplied by mingling of mafic magma at an andesite arc volcano, *Geochemistry, Geophysics, Geosystems*, *11*(4).

Eichelberger, J., C. Carrigan, H. Westrich, and R. Price (1986), Non-explosive silicic volcanism, *Nature*, *323*(6089), 598–602.

Galetto, F., M. Bagnardi, V. Acocella, and A. Hooper (2018), Noneruptive unrest at the caldera of alcedo volcano (galápagos islands) revealed by insar data and geodetic modeling, *Journal of Geophysical Research: Solid Earth*.

Giordano, D., J. K. Russell, and D. B. Dingwell (2008), Viscosity of magmatic liquids: a model, *Earth and Planetary Science Letters*, *271*(1), 123–134.

Goto, A. (1999), A new model for volcanic earthquake at Unzen Volcano: Melt rupture model, *Geophysical Research Letters*, *26*(16), 2541–2544.

Green, D., J. Neuberg, and V. Cayol (2006), Shear stress along the conduit wall as a plausible source of tilt at Soufrière Hills volcano, Montserrat, *Geophysical Research Letters*, *33*(10).

Hale, A. J., G. Wadge, and H. B. Mühlhaus (2007), The influence of viscous and latent heating on crystal-rich magma flow in a conduit, *Geophysical Journal International*, *171*(3), 1406–1429.

Hall, M. L., A. L. Steele, B. Bernard, P. A. Mothes, S. X. Vallejo, G. A. Douillet, P. A. Ramón, S. X. Aguaiza, and M. C. Ruiz (2015), Sequential plug formation, disintegration by Vulcanian explosions, and the generation of granular Pyroclastic Density Currents at Tungurahua volcano (2013–2014), Ecuador, *Journal of Volcanology and Geothermal Research*, *306*, 90–103.

Heap, M., Y. Lavallée, L. Petrakova, P. Baud, T. Reuschle, N. Varley, and D. B. Dingwell (2014), Microstructural controls on the physical and mechanical properties of edifice-forming andesites at Volcán de Colima, Mexico, *Journal of Geophysical Research: Solid Earth*, *119*(4), 2925–2963.

Heap, M. J., J. I. Farquharson, A. R. Kushnir, Y. Lavallée, P. Baud, H. A. Gilg, and T. Reuschlé (2018), The influence of water on the strength of neapolitan yellow tuff, the most widely used building stone in naples (italy), *Bulletin of Volcanology*, *80*(6), 51.

Heap, M. J., M. Villeneuve, F. Albino, J. I. Farquharson, E. Brothelande, F. Amelung, J.-L. Got, and P. Baud (2019), Towards more realistic values of elastic moduli for volcano modelling, *Journal of Volcanology and Geothermal Research*, p. 106684.

Hickey, J., J. Gottsmann, and R. del Potro (2013), The large-scale surface uplift in the altiplano-puna region of bolivia: A parametric study of source characteristics and crustal rheology using finite element analysis, *Geochemistry, Geophysics, Geosystems*, *14*(3), 540–555.

Iverson, R. M., D. Dzurisin, C. A. Gardner, T. M. Gerlach, R. G. LaHusen, M. Lisowski, J. J. Major, S. D. Malone, J. A. Messerich, S. C. Moran, et al. (2006), Dynamics of seismogenic volcanic extrusion at Mount St Helens in 2004–05, *Nature*, *444*(7118), 439–443.

Johnson, J., M. Ruiz, H. Ortiz, L. Watson, G. Viracucha, P. Ramon, and M. Almeida (2018), Infrasound tornillos produced by Volcán Cotopaxi's deep crater, *Geophysical Research Letters*, *45*(11), 5436–5444.

Johnson, J. H., M. P. Poland, K. R. Anderson, and J. Biggs (2019), A cautionary tale of topography and tilt from Kīlauea Caldera, *Geophysical Research Letters*, *46*(8), 4221–4229.

Kazahaya, K., H. Shinohara, and G. Saito (1994), Excessive degassing of Izu-Oshima volcano: magma convection in a conduit, *Bulletin of Volcanology*, *56*(3), 207–216.

Kazahaya, K., H. Shinohara, and G. Saito (2002), Degassing process of satsuma-iwojima volcano, japan: Supply of volatile components from a deep magma chamber, *Earth, planets and space*, *54*(3), 327–335.

Kendrick, J., Y. Lavallée, T. Hirose, G. Di Toro, A. Hornby, S. De Angelis, and D. Dingwell (2014), Volcanic drumbeat seismicity caused by stick-slip motion and magmatic frictional melting, *Nature Geoscience*, *7*(6), 438.

Maron, S. H., and P. E. Pierce (1956), Application of Ree-Eyring generalized flow theory to suspensions of spherical particles, *Journal of colloid science*, *11*(1), 80–95.

Mastin, L. G. (2005), The controlling effect of viscous dissipation on magma flow in silicic conduits, *Journal of Volcanology and Geothermal Research*, *143*(1), 17–28.

Medina, L. N., D. F. Arcos, and M. Battaglia (2017), Twenty years (1990–2010) of geodetic monitoring of Galeras volcano (Colombia) from continuous tilt measurements, *Journal of Volcanology and Geothermal Research*.

Melnik, O., and R. Sparks (1999), Nonlinear dynamics of lava dome extrusion, *Nature*, *402*(6757), 37.

Mogi, K. (1958), Relations between the eruptions of various volcanoes and the deformations of the ground surfaces around them, *Bulletin of the Earthquake Research Institute, University of Tokyo*, *36*, 99–134.

Mothes, P. A., H. A. Yepes, M. L. Hall, P. A. Ramón, A. L. Steele, and M. C. Ruiz (2015), The scientific–community interface over the fifteen-year eruptive episode of Tungurahua Volcano, Ecuador, *Journal of Applied Volcanology*, *4*(1), 9.

Muller, C., J. Biggs, S. K. Ebmeier, P. Mothes, P. B. Palacios, P. Jarrín, M. Edmonds, and M. Ruiz (2018), Temporal evolution of the magmatic system at tungurahua volcano, ecuador, detected by geodetic observations, *Journal of Volcanology and Geothermal Research*, *368*, 63–72.

Neuberg, J., H. Tuffen, L. Collier, D. Green, T. Powell, and D. Dingwell (2006), The trigger mechanism of low-frequency earthquakes on Montserrat, *Journal of Volcanology and Geothermal Research*, *153*(1), 37–50.

Neuberg, J. W., A. S. Collinson, P. A. Mothes, M. C. Ruiz, and S. Aguaiza (2018), Understanding cyclic seismicity and ground deformation patterns at volcanoes: Intriguing lessons from Tungurahua volcano, Ecuador, *Earth and Planetary Science Letters*, *482*, 193–200.

Odbert, H., B. Taisne, and J. Gottsmann (2015), Deposit loading and its effect on co-eruptive volcano deformation, *Earth and Planetary Science Letters*, *413*, 186–196.

Pola, A., G. B. Crosta, N. Fusi, and R. Castellanza (2014), General characterization of the mechanical behaviour of different volcanic rocks with respect to alteration, *Engineering Geology*, *169*, 1–13.

Sparks, R. S. J. (1997), Causes and consequences of pressurisation in lava dome eruptions, *Earth and Planetary Science Letters*, *150*(3-4), 177–189.

Thomas, M. E., and J. Neuberg (2012), What makes a volcano tick-A first explanation of deep multiple seismic sources in ascending magma, *Geology*, *40*(4), 351–354.

Thomas, M. E., and J. W. Neuberg (2014), Understanding which parameters control shallow ascent of silicic effusive magma, *Geochemistry, Geophysics, Geosystems*, *15*(11), 4481–4506.

Tuffen, H., D. B. Dingwell, and H. Pinkerton (2003), Repeated fracture and healing of silicic magma generate flow banding and earthquakes?, *Geology*, *31*(12), 1089–1092.

Voight, B. (1988), A method for prediction of volcanic eruptions, *Nature*, *332*(6160), 125–130.

Voight, B., R. Hoblitt, A. Clarke, A. Lockhart, A. Miller, L. Lynch, and J. McMahon (1998), Remarkable cyclic ground deformation monitored in real-time on Montserrat, and its use in eruption forecasting, *Geophysical Research Letters*, *25*(18), 3405–3408.

Voight, B., R. Sparks, A. Miller, R. Stewart, R. Hoblitt, A. Clarke, J. Ewart, W. Aspinall, B. Baptie, E. Calder, et al. (1999), Magma flow instability and cyclic activity at Soufrière Hills Volcano, Montserrat, British West Indies, *Science*, *283*(5405), 1138–1142.

Wadge, G., R. Herd, G. Ryan, E. Calder, and J.-C. Komorowski (2010), Lava production at soufrière hills volcano, montserrat: 1995–2009, *Geophysical Research Letters*, *37*(19).

Widiwijayanti, C., A. Clarke, D. Elsworth, and B. Voight (2005), Geodetic constraints on the shallow magma system at Soufrière Hills Volcano, Montserrat, *Geophysical Research Letters*, *32*(11).

Wright, H. M., and R. F. Weinberg (2009), Strain localization in vesicular magma: Implications for rheology and fragmentation, *Geology*, *37*(11), 1023–1026.

Zobin, V. M., H. Santiago-Jiménez, J. J. Ramírez-Ruiz, G. A. Reyes-Dávila, M. Bretón-González, and C. Navarro-Ochoa (2007), Quantification of volcanic explosions from tilt records: Volcán de Colima, México, *Journal of Volcanology and Geothermal Research*, *166*(2), 117–124.

Appendix A

Supplementary material for Chapter 2

The materials presented in Appendix A were included as online Supplementary Material in the following publication:

Citation: **Marsden, L. H.**, Neuberg, J., Thomas, M., Mothes, P., and Ruiz, M. (2019). *Combining magma flow and deformation modelling to explain observed changes in tilt.* Frontiers in Earth Science 7, 219

A.1 Computation of the bubble radius

In order to compute the capillary number at any point within the conduit (Eq. 2.11), the bubble radius, R_b, must first be computed. This section shows the steps required to do this.

The bubble number density, n_b, quantifies of the number of bubbles per metre cubed of melt, each with a melt shell volume of ${S_0}^3$ (*Hurwitz and Navon*, 1994). Here, we assume that bubbles nucleate homogeneously in a single event.

$$ {S_0}^3 = \frac{3}{4\pi n_b} \tag{A.1} $$

As magma ascends and the bubble radius R_b increases, the proportion of melt, ϕ_m, in the shell of volume ${S_0}^3$ decreases. As n_b remains constant with respect to the volume of melt, n_b also decreases as the bubbles expand. The bubble number density, n_b, can be derived as a function of ϕ_m and the gas volume fraction, ϕ_g, where b_{ni} is the bubble number density immediately after nucleation.

$$ n_b = \frac{b_{ni}}{\phi_m} \left[\phi_m - (1 - \phi_g)\right] \tag{A.2} $$

Under the same assumption of homogeneous nucleation and expansion of bubbles,

the bubble radius, R_b, can be calculated through

$$R_b = \left[\frac{{S_0}^3 \rho_m (C_0 - C_m)}{\rho_g} \right]^{1/3} \tag{A.3}$$

where ρ_m and ρ_g are the densities of the melt and gas in the bubbles, respectively, and C_0 and C_m are the initial and remaining amount of dissolved water in the melt, respectively (*Lensky et al.*, 2002).

A.2 Relationship between viscosity and shear stress for a Newtonian fluid

From the Hagen-Poisuille equations for the flow of a Newtonian fluid through a cylindrical conduit, the strain rate can be given as

$$\frac{dv_z}{dr} = \frac{-2P'r}{4\eta} \tag{A.4}$$

where r is the horizontal coordinate and P' is the vertical pressure gradient. At the conduit wall, $r = R_c$. Combining Eqs. 2.1 and A.4 provides the shear stress at the conduit wall.

$$\sigma_s = \frac{\eta dv_z}{dr} = \frac{-P'R_c}{2} \tag{A.5}$$

Eq. A.4 shows that the strain rate is inversely proportional to the viscosity. However, as the shear stress is directly proportional to the viscosity and the strain rate, the viscosity term in Eq. A.5 cancels (Eq. 2.1). A higher viscosity magma ascends with a proportionally lower ascent velocity.

A.3 Gradual exsolution

To achieve a gradual onset to exsolution as shown in Figure A.1, Eq. 2.7 is modified using the following cosine taper.

$$C_{wx} = C_w + \left[\frac{1 + \cos\left(\pi \frac{C_{wi} - C_w}{C_{wi}} \right)}{2} \right]^6 \tag{A.6}$$

Essentially, the theoretical dissolved water content C_w has been subtracted from initial dissolved water content C_{wi}, to give the concentration of H_2O that has been exsolved. This difference has been multiplied by a normalised cosine taper, that ranges from 0 where $C_w = 0$ and 1 at the nucleation depth, where $C_w = C_{wi}$. This cosine

taper has then been raised to the power of 6 to achieve a desired trend, and added to the theoretical dissolved water content C_w.

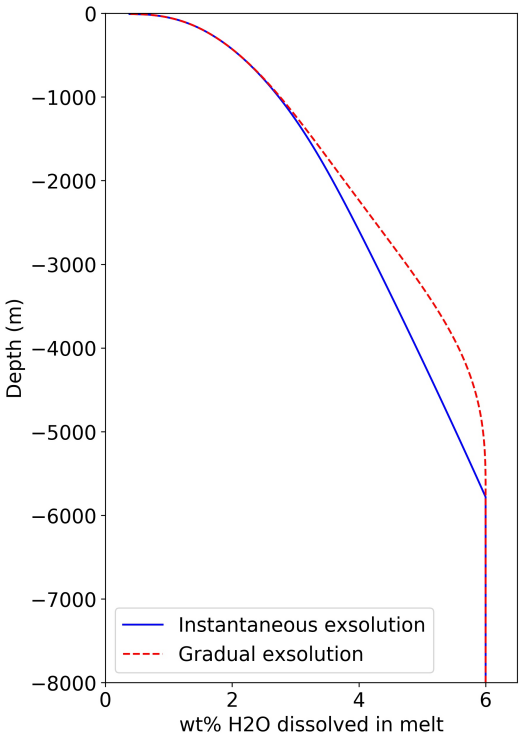

Figure A.1: Content of dissolved water in the melt, obtained from the reference model, either using the solubility law of *Zhang et al.* (2007) (solid) assuming instantaneous exsolution, or modified using Eq. A.6 to simulate a more gradual exsolution (dashed). Note a smoother onset to exsolution is obtained using Eq. A.6, whilst the trend is similar towards the surface.

A.4 Above what depth does exsolved gas escape from the conduit?

Experiments by *Okumura et al.* (2008) on bubble-bearing rhyolitic magma showed that permeability may develop at moderate bubble contents ($\phi_g > 0.20$) due to shear-induced coalescence. Gas loss may be facilitated by fractures in the magma towards the conduit-edifice boundary (*Gonnermann and Manga*, 2003, *Gaunt et al.*, 2014), created from brittle failure of magma at a critical shear stress (*Neuberg et al.*, 2006). The lifespan of such fractures may be short, and so repeated fracturing may be necessary to maintain high permeability (*Cordonnier et al.*, 2012, *Castro et al.*, 2012). However, fractured magma is replaced by fresh underlying magma as it ascends, which will fracture at the same depth if the ascent velocity, viscosity, a conduit geometry remain constant (*Thomas and Neuberg*, 2012). Fractures continue to form as long as magma ascends faster than a critical threshold.

The above methods are effective at outgassing from the conduit boundary where

strain rate is higher. However, a mechanism is required to transport volatiles from the centre of the conduit to the wall. At low bubble contents ($\phi_g = 0.11$), strain-localisation in crystal-rich ($\phi_c = 0.52$) magma has been experimentally shown to induce Riedel shear geometries (*Laumonier et al.*, 2011). Additionally, *Kushnir et al.* (2017) performed experiments on bubble-bearing magma ($\phi_g < 0.20$) to assess the influence of shear-induced fractures on permeability. They found that extensional Mode 1 fractures formed with tip orientations of around 45° with respect to the direction of shear (the direction of least compressive stress, σ_3) and observed an in situ increase in permeability. Both Mode 1 extensional and Riedel shear geometry fractures may provide pathways for outgassing from the centre of the conduit.

The minimum porosity required for degassing is unclear and varies with crystal volume fraction (*Laumonier et al.*, 2011) and strain rate (*Okumura et al.*, 2008, *Caricchi et al.*, 2011). Also, it is unclear how magma permeability and degassing vary with depth. Therefore, in this study, a simplified forced degassing approach is adopted, where an empirical permeability depth profile is provided. We assume that no permeable degassing pathways exist where $\phi_g < 0.2$, a reasonable compromise based on the values referenced. This corresponds to a depth of 1600 m in the reference model.

References

Caricchi, L., A. Pommier, M. Pistone, J. Castro, A. Burgisser, and D. Perugini (2011), Strain-induced magma degassing: insights from simple-shear experiments on bubble bearing melts, *Bulletin of volcanology*, *73*(9), 1245–1257.

Castro, J. M., B. Cordonnier, H. Tuffen, M. J. Tobin, L. Puskar, M. C. Martin, and H. A. Bechtel (2012), The role of melt-fracture degassing in defusing explosive rhyolite eruptions at volcán Chaitén, *Earth and Planetary Science Letters*, *333*, 63–69.

Cordonnier, B., L. Caricchi, M. Pistone, J. Castro, K.-U. Hess, S. Gottschaller, M. Manga, D. Dingwell, and L. Burlini (2012), The viscous-brittle transition of crystal-bearing silicic melt: Direct observation of magma rupture and healing, *Geology*, *40*(7), 611–614.

Gaunt, H. E., P. R. Sammonds, P. G. Meredith, R. Smith, and J. S. Pallister (2014), Pathways for degassing during the lava dome eruption of Mount St. Helens 2004–2008, *Geology*, *42*(11), 947–950.

Gonnermann, H. M., and M. Manga (2003), Explosive volcanism may not be an inevitable consequence of magma fragmentation, *Nature*, *426*(6965), 432–435.

Hurwitz, S., and O. Navon (1994), Bubble nucleation in rhyolitic melts: Experiments at high pressure, temperature, and water content, *Earth and Planetary Science Letters*, *122*(3-4), 267–280.

Kushnir, A. R., C. Martel, R. Champallier, and L. Arbaret (2017), In situ confirmation of permeability development in shearing bubble-bearing melts and implications for volcanic outgassing, *Earth and Planetary Science Letters*, *458*, 315–326.

Laumonier, M., L. Arbaret, A. Burgisser, and R. Champallier (2011), Porosity redistribution enhanced by strain localization in crystal-rich magmas, *Geology*, *39*(8), 715–718.

Lensky, N., V. Lyakhovsky, and O. Navon (2002), Expansion dynamics of volatile-supersaturated liquids and bulk viscosity of bubbly magmas, *Journal of fluid mechanics*, *460*, 39–56.

Neuberg, J., H. Tuffen, L. Collier, D. Green, T. Powell, and D. Dingwell (2006), The trigger mechanism of low-frequency earthquakes on Montserrat, *Journal of Volcanology and Geothermal Research*, *153*(1), 37–50.

Okumura, S., M. Nakamura, A. Tsuchiyama, T. Nakano, and K. Uesugi (2008), Evolution of bubble microstructure in sheared rhyolite: Formation of a channel-like bubble network, *Journal of Geophysical Research: Solid Earth*, *113*(B7).

Thomas, M. E., and J. Neuberg (2012), What makes a volcano tickA first explanation of deep multiple seismic sources in ascending magma, *Geology*, *40*(4), 351–354.

Zhang, Y., Z. Xu, M. Zhu, and H. Wang (2007), Silicate melt properties and volcanic eruptions, *Reviews of Geophysics*, *45*(4).

Appendix B

Supplementary material for Chapter 3

The materials presented in Appendix B were included as online Supplementary Material in the following publication:
Citation: **Marsden, L. H.**, Neuberg, J., Thomas, M. (2019). *Topography and tilt at volcanoes.* Frontiers in Earth Science 7, 317

B.1 2D axisymmetric models with a constant slope angle

The constant slope angles used for the 2D axisymmetric models in Section 3.5 were calculated by calculating the mean slope angle from the summit to the base of the edifice for each DEM. To calculate this, 360 points at 1° intervals where taken at a fixed distance of 6 km from the conduit for Tungurahua volcano and 4 km for SHV. The difference in both elevation and horizontal distance between each point and the summit was used to calculate an average slope angle for all 360 points. The slope angle of the reference model is the mean of the 360 values computed. This equated to an angle of 18° for Tungurahua and 12° for SHV. The elevation of the surface of each reference model is plotted in Figure B.1, alongside profiles for the elevation versus distance from the conduit at 1° intervals in the DEM.

The model boundaries are set in the same way as the models in Section 3.3, and the model is similarly extended to a radius of 40 km and a depth of 50 km. A spatially-variant triangular is divided such that the upper 10 km below the surface to a distance of 10 km can be meshed more finely (Figure B.2). An element size of around 100 m is used within this region, decreasing to as small as 2 m close to the base of the conduit.

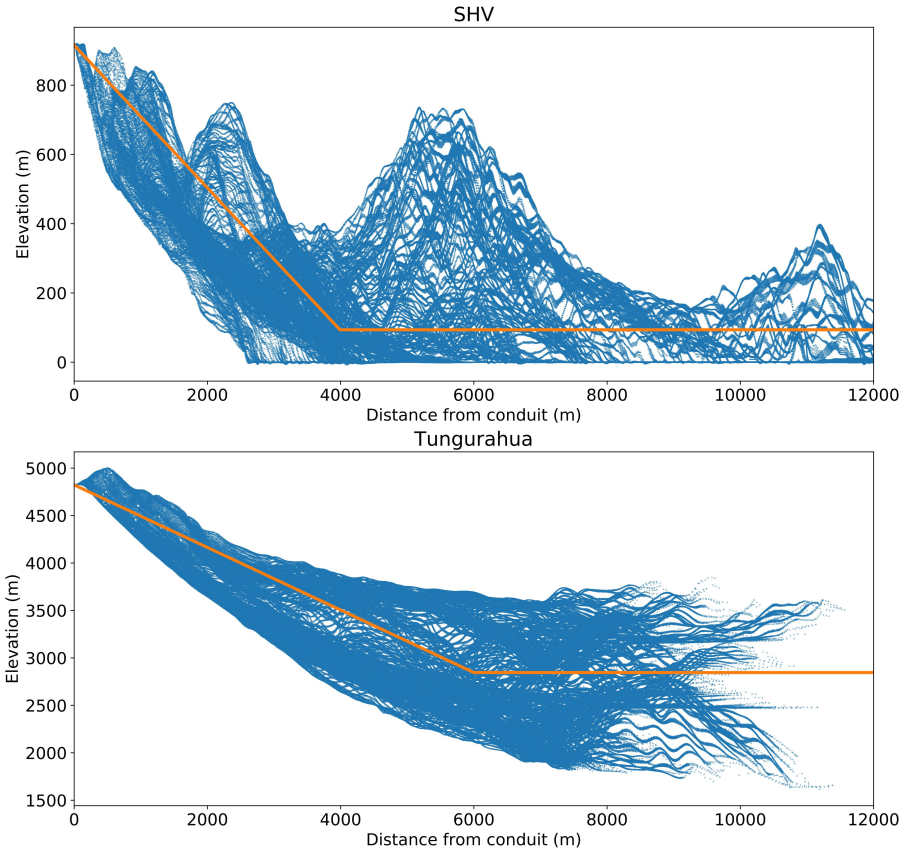

Figure B.1: Surface elevation for the 2D axisymmetric models with a constant slope, as used to obtain $\Delta\theta_r$ in Section 5 (orange line). The elevation and distance from the conduit for mesh points across each DEM are also plotted at 1° intervals (blue dots).

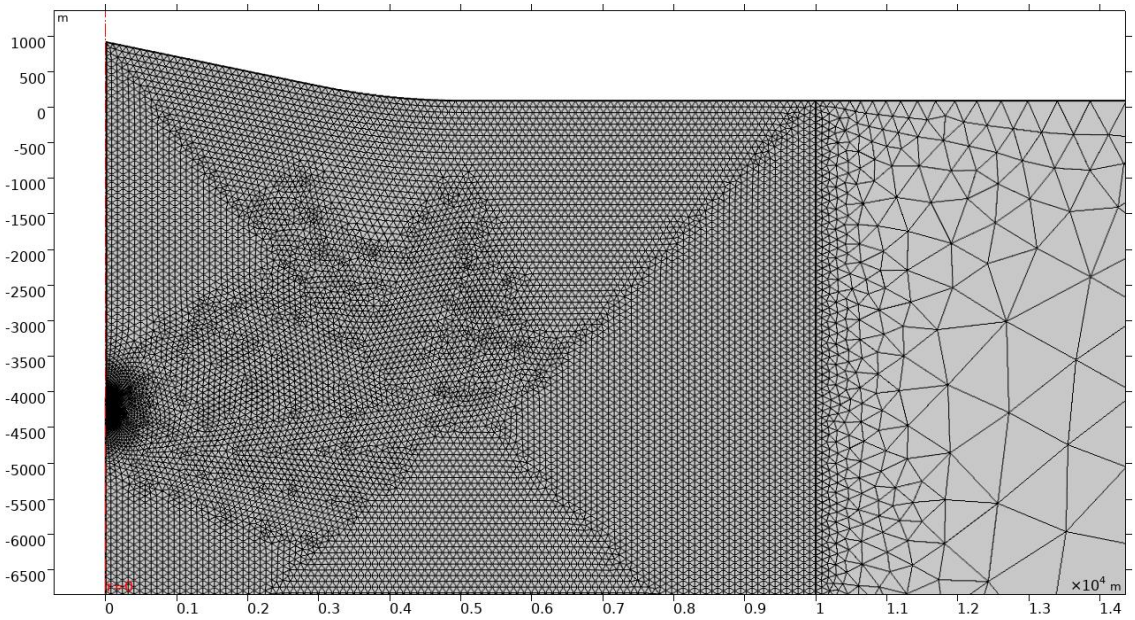

Figure B.2: Example of a mesh used for the 2D axisymmetric models with a constant slope. A high resolution mesh is used to a depth of 10 km below the surface, to a horizontal distance of 10 km, with an element size of around 100 m, that decreases to around 2 m close to the base of the conduit.

Appendix C

Supplementary material for Chapter 4

C.1 Governing equations

Magma ascent is governed by the compressible form of the Navier-Stokes equation

$$\rho\frac{d\mathbf{w}}{dt} + \rho\mathbf{w}\cdot\nabla\mathbf{w} = -\nabla P + \nabla\cdot\left(\eta\left[\nabla\mathbf{w} + (\nabla\mathbf{w})^T\right] - \frac{2}{3}\eta\left[\nabla\cdot\mathbf{w}\right]I\right) + \mathbf{F} \tag{C.1}$$

and the continuity equation

$$\frac{d\rho}{dt} + \nabla\cdot(\rho\mathbf{w}) = 0 \tag{C.2}$$

where ρ is density, $\mathbf{w}$ is the velocity vector, P is pressure, η is the viscosity, $\mathbf{F}$ is a volume force vector, in this case gravity, and I is the identity tensor (*Faber*, 1995).

C.2 Melt composition

Oxide	SiO_2	TiO_2	Al_2O_3	FeO^T	MnO	MgO	CaO	Na_2O	K_2O
wt.%	71.41	0.28	13.58	2.78	0.13	1.64	4.86	3.73	1.60

Table C.1: Composition of melt phase, from rastered electron microprobe analysis of groundmass, SHV (*Barclay et al.*, 1998)

C.3 Gas loss

Exsolved gas can escape from the conduit through pathways of connected bubbles (*Okumura et al.*, 2008) or fractures in the magma (*Gonnermann and Manga*, 2003). However, how much gas is lost from the conduit depends on a number of factors,

including the the gas volume fraction, strain rate (*Okumura et al.*, 2008, *Rust and Cashman*, 2004), the connectivity and orientation of fractures (*Kushnir et al.*, 2017), and the permeability of the wall rocks (*Jaupart and Allègre*, 1991). Whilst a number of authors have shown that ascent dynamics are sensitive to the permeability of the magma or surrounding edifice (*Melnik and Sparks*, 1999, *Diller et al.*, 2006), the proportion of gas that is lost from a conduit is poorly constrained. Therefore, we use a simple cosine taper to quantify the gas loss with depth, as in *Marsden et al.* (2019). The gas loss function is held constant through time in each model. This is an oversimplification, as *Melnik and Sparks* (1999) showed that as the ascent velocity decreases, more gas is able to escape from the conduit. This leads to a reduction in the buoyancy of the magma column, which consequently reduces the ascent velocity further. However, there are also large uncertainties in both the permeability of the magma column and edifice and the rate of crystallisation, which each exert a similar non-linear control on the ascent velocity (*Melnik and Sparks*, 1999). As the ascent velocity decreases, crystals have longer to grow, which causes the viscosity to increase and ascent velocity to decrease. Thus, the would-be effect of changing the gas loss function through time is encompassed by the uncertainty in the rate of crystallisation. The parameterisation for our reference model is tuned to achieve a critical dome height in line with that observed at SHV.

C.4 Magma density

The bulk density of three phase magma, ρ_b, is a function of the relative proportion and density of each phase

$$\rho_\mathrm{b} = \rho_\mathrm{m}(1-\phi_\mathrm{c})(1-\phi_\mathrm{g}) + \rho_\mathrm{g}\phi_\mathrm{g} + \phi_\mathrm{c}\rho_\mathrm{c}(1-\phi_\mathrm{g}) \tag{C.3}$$

where ϕ_c is the crystal content, ϕ_g is the gas volume fraction, and ρ_m, ρ_c and ρ_g are the density of the melt, crystal and gas phases respectively. The density of the melt phase is a function of composition (Table C.1), pressure and temperature, as in *Spera* (2000), hence both the bulk and melt density varies spatially within the conduit.

C.5 Model setup

The conduit is represented in 2D axisymmetric space as a cylinder. A mesh refinement study was performed to ensure that the mesh resolution was sufficient so that the solution would be consistent if refined further. The extrusion rate and dome height are the key parameters of interest in this study, and so spatial variations in other parameters within the conduit do not need to be mapped at a high resolution. Hence, a relatively coarse rectangular mesh with a horizontal distance of 5 m and vertical distance of 20 m between nodes is sufficient in most models. A no slip boundary condition is applied

at the conduit walls, hence $v_z = 0\,\mathrm{m/s}$ here. The pressure at the top and base of the conduit, P_{top} and P_{base} respectively, are set as

$$P_{top} = P_a + P_L \tag{C.4}$$

$$P_{base} = P_a + \rho_e g z_c + P_e, \tag{C.5}$$

where ρ_e is the density of the edifice surrounding the conduit, g is acceleration due to gravity, z_c is the depth in the conduit, P_a is atmospheric pressure, P_L is confining pressure due to the weight of the dome, and P_e is excess pressure at the base of the conduit.

A time-dependent solver outputs a solution for each variable at discrete intervals in time. The time interval is determined using a backward differentiation formula that is inbuilt into COMSOL. The time interval between successive solutions is shorter where the solution changes more dramatically.

References

Barclay, J., M. J. Rutherford, M. Carroll, M. Murphy, J. Devine, J. Gardner, and R. Sparks (1998), Experimental phase equilibria constraints on pre-eruptive storage conditions of the soufrière hills magma, *Geophysical Research Letters*, *25*(18), 3437–3440.

Diller, K., A. Clarke, B. Voight, and A. Neri (2006), Mechanisms of conduit plug formation: Implications for vulcanian explosions, *Geophysical Research Letters*, *33*(20).

Faber, T. E. (1995), *Fluid dynamics for physicists*, Cambridge university press.

Gonnermann, H. M., and M. Manga (2003), Explosive volcanism may not be an inevitable consequence of magma fragmentation, *Nature*, *426*(6965), 432–435.

Jaupart, C., and C. J. Allègre (1991), Gas content, eruption rate and instabilities of eruption regime in silicic volcanoes, *Earth and Planetary Science Letters*, *102*(3-4), 413–429.

Kushnir, A. R., C. Martel, R. Champallier, and L. Arbaret (2017), In situ confirmation of permeability development in shearing bubble-bearing melts and implications for volcanic outgassing, *Earth and Planetary Science Letters*, *458*, 315–326.

Marsden, L. H., J. Neuberg, M. Thomas, P. Mothes, and M. Ruiz (2019), Combining magma flow and deformation modelling to explain observed changes in tilt, *Frontiers in Earth Science*, *7*, 219.

Melnik, O., and R. Sparks (1999), Nonlinear dynamics of lava dome extrusion, *Nature*, *402*(6757), 37.

Okumura, S., M. Nakamura, A. Tsuchiyama, T. Nakano, and K. Uesugi (2008), Evolution of bubble microstructure in sheared rhyolite: Formation of a channel-like bubble network, *Journal of Geophysical Research: Solid Earth*, *113*(B7).

Rust, A., and K. V. Cashman (2004), Permeability of vesicular silicic magma: inertial and hysteresis effects, *Earth and Planetary Science Letters*, *228*(1-2), 93–107.

Spera, F. J. (2000), Physical properties of magma, *Encyclopedia of volcanoes*, *176*.